

CRANFIELD UNIVERSITY

HONGQUAN LIU

PLY CLUSTERING EFFECT ON COMPOSITE LAMINATES  
UNDER LOW-VELOCITY IMPACT USING FEA

SCHOOL OF ENGINEERING  
MSc AIRCRFT DESIGN PROGRAMME

MSc by Research  
Academic Year: 2011 – 2012

Supervisor: Dr. Xiang Zhang  
January 2012



CRANFIELD UNIVERSITY

SCHOOL OF ENGINEERING  
MSc AIRCRAFT DESIGN PROGRAMME

MSc by Research

Academic Year 2011 - 2012

HONGQUAN LIU

PLY CLUSTERING EFFECT ON COMPOSITE LAMINATES  
UNDER LOW-VELOCITY IMPACT USING FEA

Supervisor: Dr. Xiang Zhang  
January 2012

© Cranfield University 2011. All rights reserved. No part of this publication may be reproduced without the written permission of the copyright owner.



## **ABSTRACT**

With the development of the design and manufacture technology, composite materials are widely used in the aeronautical industry. But, one of the main concerns which affects the application of composites is foreign object impact. The damages induced by the Low Velocity Impact (LVI), which can significantly reduce the strength of the structures, can't be easily inspected routinely. The so-called Barely Visible Impact Damages (BVID) due to LVI typically includes interlaminar delamination, matrix cracks and fibre fracture at the back face.

Previous researches have shown that the results of LVI test are similar to that of the Quasi-Static Load (QSL) test. The initiation and propagation of delamination can be detected more easily in the QSL test and the displacement and reaction force of the impactor can be controlled and measured much more accurately. Moreover, it is easier to model QSL tests than dynamic impacts.

To investigate the impact damage induced by LVI, a Finite Element (FE) model employing cohesive elements was used. At the same time, the ply clustering effect, when several plies of the same orientation were stack together, was modelled in the FE model in terms of damage resistance and damage size. A bilinear traction-separation law was introduced in the cohesive elements employed to simulate the initiation and propagation of the impact damage and delamination.

Firstly, a 2D FE model of the Double Cantilever Beam (DCB) and End Notched Flexure (ENF) specimens were built using the commercial FEM software ABAQUS. The results have shown that the cohesive elements can be used to simulate mode I and mode II delamination sufficiently and correctly.

Secondly, an FE model of a composite plate under QSL but without simulating damage was built using the continuum shell elements. Agreement between the FEA results with published test results is good enough to validate the capability of continuum shell elements and cohesive elements in modelling the composite laminate under the transverse load condition (QSL).

Thirdly, an FE model containing discrete interface delamination and matrix cracks at the back face of the composite plate was built by pre-setting the cohesive failure elements at potential damage locations according to the experimental observation. A cross-ply laminate was modelled first where fewer interfaces could be delaminated. Good agreement was found in terms of the delamination area and impactor's displacement-force curve.

Finally, the effect of ply clustering on impact damage resistance was studied using Quasi-Isotropic (QI) layup laminates.

Because of the limited time available for calculation, the simulation was only partly completed for the quasi-isotropic laminates (L2 configuration) which have more delaminated interfaces. The results showed that cohesive elements obeying the bilinear traction-separation law were capable of predicting the reaction force in quasi-isotropic laminates. However, discrepancies with the test results in terms of delamination area were observed for quasi-isotropic laminates. These discrepancies are mainly attributed to the simplification of matrix cracks simulation and compressive load at the interface in the thickness direction which is not taken into account.

Keywords:

Composite Laminates, Low-Velocity Impact, Quasi-Static Load, Delamination, Matrix Crack, Finite Element Method (FEM), Cohesive Elements

## **ACKNOWLEDGEMENTS**

I would like to thank the Aviation Industry Corporation of China (AVIC), the China Scholarship Council and the First Aircraft Institute (FAI) of AVIC for providing me with the opportunity to undertake the master's course in aircraft design at Cranfield University.

I would like to express my appreciation to my supervisor Dr. Xiang Zhang and her PHD student Francesco whose technical guidance and support helped me finish this thesis.

I would like to say my thanks to my family members and friends for their understanding and encouragement. I also want to thank my landlady Liz Anderson for correcting my English mistakes. And last, I would like to give special thanks to my wife Wenting Cheng who looked after our very young daughter during my stay in Cranfield, her encouragement and support has helped me concentrate on my research work.





# TABLE OF CONTENTS

ABSTRACT .....	i
ACKNOWLEDGEMENTS.....	iii
LIST OF FIGURES.....	vii
LIST OF TABLES .....	xi
NOMENCLATURE .....	xiii
1 INTRODUCTION.....	1
1.1 Background.....	1
1.2 Project Aim and Objectives.....	5
2 LITERATURE REVIEW .....	6
2.1 Introduction .....	6
2.2 Low Velocity Impact.....	7
2.3 Impact Damage Types.....	9
2.4 Parameters in Impact.....	13
2.5 Critical Force and Critical Energy.....	14
2.6 Finite Element Method.....	16
2.7 Clustering Effect .....	18
3 METHODOLOGY .....	19
3.1 Introduction .....	19
3.2 Cohesive Element.....	20
3.3 Continuum Shell Element .....	21
3.4 Stress Study of Clustering Laminate.....	22
3.4.1 Transverse Shear Stress Distribution.....	22
3.4.2 Cure Induced Residual Stress.....	26
3.4.3 Fibre Bridging Effect.....	31
3.5 Damage Initiation.....	33
3.5.1 Stress Distribution Study .....	33
3.5.2 Friction Considerations in the Upper Half.....	37
3.5.3 Interaction Between Matrix Crack and Delamination.....	39
3.6 Damage Propagation .....	40
4 MODEL DCB USING COHESIVE ELEMENTS .....	41
4.1 Introduction .....	41
4.2 Geometry Model Description .....	41
4.3 FE Model Description.....	42
4.4 FE Results and Validation.....	43
4.5 Sensitivity of Cohesive Element Parameters .....	46
5 MODEL ENF USING COHESIVE ELEMENTS .....	49
5.1 Introduction .....	49
5.2 Geometry Model Description .....	49
5.3 FE Model Description.....	50
5.4 FE Results and Validation.....	51

5.5 Sensitivity of Cohesive Element Parameters .....	54
6 IMPACT LOAD SIMULATION OF LOW-VELOCITY IMPACT .....	57
6.1 Introduction .....	57
6.2 Material Properties.....	58
6.3 FE Model Description.....	58
6.4 Boundary Condition .....	60
6.5 Mesh Sensitive Analysis .....	60
6.6 Results and Discussion.....	61
7 DAMAGE SIMULATION OF CROSS-PLY LAMINATE .....	63
7.1 Specimen Description .....	63
7.2 FE Model Description.....	63
7.3 Simulation Results .....	64
8 DAMAGE SIMULATION OF CLUSTERED LAMINATE .....	73
8.1 Specimen Description .....	73
8.2 FE Model Description.....	73
8.3 Simulation Results .....	76
9 CONCLUSION .....	81
REFERENCES.....	83
APPENDICES .....	91

## LIST OF FIGURES

Figure 1-1 Design load versus damage severity in composite structures [4].....	2
Figure 1-2 Comparison between clustering and non-clustering layup .....	2
Figure 1-3 Comparison of reaction load versus displacement [14].....	4
Figure 2-1 Response types during impact on plate [20] .....	8
Figure 2-2 Nature of LVI damage in composite plates [24] .....	10
Figure 2-3 Micrographs of the cross-section in different energy level [25] .....	10
Figure 2-4 Damage patterns of stiff and flexible plates [28] .....	11
Figure 2-5 Mode I, II and III crack deformation [40].....	12
Figure 2-6 Hemispherical, ogival and conical Impact Tups [43] .....	14
Figure 2-7 Impact force versus damage area for different plate size [18].....	15
Figure 3-1 Cohesive elements placement illustration .....	19
Figure 3-2 Traction-separation law for mode I and mode II/III fracture [62].....	20
Figure 3-3 Conventional shell element versus continuum shell element [72]...	21
Figure 3-4 Model for transverse shear stress distribution study .....	22
Figure 3-5 FE model using conventional shell elements .....	23
Figure 3-6 FE model using plane strain elements .....	23
Figure 3-7 Transverse shear stress distribution for isotropic material .....	24
Figure 3-8 Axial strain distribution of L1, L2, L3 .....	24
Figure 3-9 Axial stress distribution of L1, L2, L3.....	25
Figure 3-10 Shear stress distribution of L1, L2, L3 and isotropic material.....	25
Figure 3-11 Shear stress distribution of L1, L2, L3 and isotropic material.....	26
Figure 3-12 Model for thermal expansion study .....	27
Figure 3-13 Shear stress distribution along the interface in the x-z direction ...	28
Figure 3-14 Shear stress distribution along the interface in the y-z direction ...	28
Figure 3-15 Residual in-plane stress for layer oriented at 90° .....	30
Figure 3-16 Residual in-plane stress for layer oriented at 0° .....	30
Figure 3-17 Fibre bridging model after curing.....	31
Figure 3-18 Mode I fracture toughness against crack length [3].....	32

Figure 3-19 FE model stress distribution study .....	34
Figure 3-20 Contours plot of peel stress along plate span .....	34
Figure 3-21 Peel stress distribution along plate span.....	35
Figure 3-22 Contours plot of transverse shear stress along plate span .....	35
Figure 3-23 Transverse shear stress distribution along plate span .....	36
Figure 3-24 In-plane strain distribution along span.....	36
Figure 3-25 The relation between cohesive elements and contact pair.....	38
Figure 4-1 DCB specimen geometry (unit: mm) .....	41
Figure 4-2 The half finite element model of DCB.....	43
Figure 4-3 Shear stress distributions along the interface .....	44
Figure 4-4 The whole finite element model of DCB .....	44
Figure 4-5 Relations between reaction force and displacement.....	44
Figure 4-6 X-direction normal stress distributions (unit: MPa) .....	45
Figure 4-7 Y-direction peel stress distributions (unit: MPa) .....	45
Figure 4-8 Transverse shear stress distributions (unit: MPa) .....	45
Figure 4-9 Shear stress distributions along the interface .....	46
Figure 4-10 Peel stress distribution along the interface.....	46
Figure 4-11 Reaction load versus displacement with different initial stiffness ..	47
Figure 4-12 Reaction load versus displacement with different interface strength .....	48
Figure 4-13 Reaction load versus displacement with different critical SERR ...	48
Figure 5-1 ENF specimen geometry (unit: mm).....	49
Figure 5-2 Relations between reaction force and displacement.....	52
Figure 5-3 X-direction normal stress distributions (unit: MPa) .....	52
Figure 5-4 Y-direction peel stress distributions (unit: MPa) .....	52
Figure 5-5 Transverse shear stress distributions (unit: MPa) .....	53
Figure 5-6 Shear stress distributions along the interface .....	54
Figure 5-7 Peel stress distribution along the interface.....	54
Figure 5-8 Reaction load versus displacement with different initial stiffness ....	55
Figure 5-9 Reaction load versus displacement with different interface strength	56

Figure 5-10 Reaction load versus displacement with different critical SERR ...	56
Figure 6-1 Comparison of static and impact load versus displacement curves [14].....	57
Figure 6-2 Quasi-static load test set up [14].....	58
Figure 6-3 The FEM model using conventional shell elements of QSL test .....	59
Figure 6-4 The 3D FEM model using continuum shell elements of QSL test ...	59
Figure 6-5 The stacking sequence of the laminate $[-45/0/45/90]_{4s}$ .....	59
Figure 6-6 Boundary conditions of the FE model .....	60
Figure 6-7 Results of mesh sensitive analysis for 2D.....	61
Figure 6-8 Results of mesh sensitive analysis for 3D.....	61
Figure 6-9 Comparison of contact force versus displacement.....	62
Figure 7-1 FE model of cross-ply plate.....	64
Figure 7- 2 Peel stress distribution along the plate span.....	65
Figure 7- 3 Transverse shear stress distribution along the plate span .....	65
Figure 7-4 Comparison between FE models and experiment with friction.....	66
Figure 7-5 Comparison between FE models and experiment without friction...	66
Figure 7-6 Comparison between different CF in terms of delamination areas..	67
Figure 7-7 Applied displacement versus reaction force for cross-ply laminate .	68
Figure 7-8 Peel stress distribution along fibre direction of the lower ply .....	69
Figure 7-9 Transverse shear stress distribution along fibre direction of the lower ply .....	69
Figure 7-10 Peel stress comparison before and after matrix crack damage ....	70
Figure 7-11 Stress distribution for a delamination area away from matrix crack .....	71
Figure 7-12 Comparison of delamination area with and without matrix crack together with the experimental results.....	72
Figure 8-1 C-scan delamination results of L2 and L4 [8] .....	74
Figure 8-2 FE models of Quasi-Isotropic composite plates .....	75
Figure 8-3 Set up of the impact test of clustering laminates [8].....	75
Figure 8-4 Applied displacement versus reaction load comparison for L4 .....	76
Figure 8-5 Delamination area for interface 1, 2 and 3 of L4 .....	77

Figure 8-6 Applied displacement versus reaction load comparison for L2 ..... 78  
Figure 8-7 Delamination area for interface 1, 2 and 3 of L2 ..... 79

## LIST OF TABLES

Table 4-1 Material properties used in FE analysis.....	42
Table 4-2 Element type and size used in FE analysis [80].....	42
Table 4-3 Cohesive element parameters used in sensitive analysis .....	47
Table 5-1 Material mechanical properties used in FE analysis.....	50
Table 5-2 Element type and size used in FE analysis [80].....	51
Table 5-3 Cohesive element parameters used in sensitive analysis .....	55
Table 6-1 The material properties of the laminate .....	58
Table 6-2 Contact force comparison with different element types .....	62
Table 7- 1 Material properties of the laminate plate .....	64
Table 8-1 Material properties of the laminate plate .....	76





## NOMENCLATURE

a	Coefficients of thermal expansion (strain/ $^{\circ}\text{C}$ )
A	Cross section area ( $\text{mm}^2$ )
D	Bending stiffness (MPa)
$D^*$	Effective bending stiffness (MPa)
E	Flexural modulus (MPa)
F	Applied force (N)
G	Shear modulus (MPa)
$G_{IC}$	Mode I critical strain energy release rate ( $\text{J}/\text{mm}^2$ )
$G_{IIC}$	Mode II critical strain energy release rate ( $\text{J}/\text{mm}^2$ )
$G_{IIIC}$	Mode III critical strain energy release rate ( $\text{J}/\text{mm}^2$ )
$h_p$	Clustering thickness (mm)
k	Contact stiffness
K	Stiffness of cohesive element (MPa)
N	Peel strength of cohesive element (MPa)
$n_d$	Number of delamination interfaces
$n_d^*$	Number of delamination interfaces start from the back face
P	Contact force (N)
$P_C$	Critical contact force (N)
S	Transverse shear strength of cohesive element (MPa) in mode II
T	Transverse shear strength of cohesive element (MPa) in mode III
t	Thickness(mm)
$t_n$	Peel stress of cohesive element (MPa)
$t_s$	Transverse shear stress of cohesive element (MPa) in mode II
$t_t$	Transverse shear stress of cohesive element (MPa) in mode III
$\Delta T$	Temperature difference ( $^{\circ}\text{C}$ )
U	Translation degree of freedom
UR	Rotation degree of freedom
v	Poisson's ratio
W	Width of plate (mm)
$W_{cr}$	Critical impact energy
$\delta$	Displacement (mm)
$\delta(P_C)$	Displacement at critical contact force (mm)

$\mu$	Coefficient of friction
2D	2 Dimension
3D	3 Dimension
AVIC	Aviation Industry Corporation of China
BVID	Barely Visible Impact Damages
BWB	Blending Wing Body
CF	Coefficient of Friction
DCB	Double Cantilever Beam
ENF	End Notched Flexure
FAI	First Aircraft Institute
FE	Finite Element
FEA	Finite Element Analysis
FEM	Finite Element Method
FRP	Fibre Reinforced Plastic
GDP	Group Design Project
ILSS	Interlaminar Shear Strength
JSF	Joint Strike Fighter
LVI	Low Velocity Impact
QI	Quasi-Isotropic
QSL	Quasi-Static Load
SERR	Strain Energy Release Rate
VCCT	Virtual Crack Closure Technique

# 1 INTRODUCTION

## 1.1 Background

The application of composites in the aerospace industry has been developed very quickly in the past few decades. Composite structures are widely used in the primary structures of aircraft and account for an increasing proportion of the total structural weight. Composite materials used in the Joint Strike Fighter (JSF) and Euro fighter are about 40% of their structural mass. Furthermore, more than 50% of the aircraft skins are covered with composite material [1]. The application of composites in the Boeing 787 accounts for about 50% of its whole structural weight [2].

A continuing concern in composite structures evaluation is interlaminar delamination. Composite delamination is a potential failure mode which could happen at ply drop-offs, edges, holes and in the area of impact damage [3]. Delaminations which come from impact damage are very dangerous because they cannot be detected by routine visual inspection but the reduction of strength of the damaged structure in compression is significant. Interface delamination caused by low-velocity foreign object impacts will be studied in detail in this research.

Different categories of damage will occur in composite structures during the service life. The damage severity against design loads requirements according to airworthiness regulations is shown in figure 1-1 [4].

Among the above damage categories as can be seen in figure1-1, the Barely Visible Impact Damage (BVID) at the upper right is one of the most dangerous types of damage which is usually caused by Low Velocity Impact (LVI). BVID usually includes interlaminar delamination, matrix cracks at the back surface and interface debondings between fibre and matrix. Though the existence of matrix crack does not affect the stiffness of the structures dramatically [5], the existences of matrix crack tip will cause the initiation of delamination because of the higher stress level around it. So this study mainly focuses on shear stress

induced interface delamination and matrix crack induced interlaminar delamination.

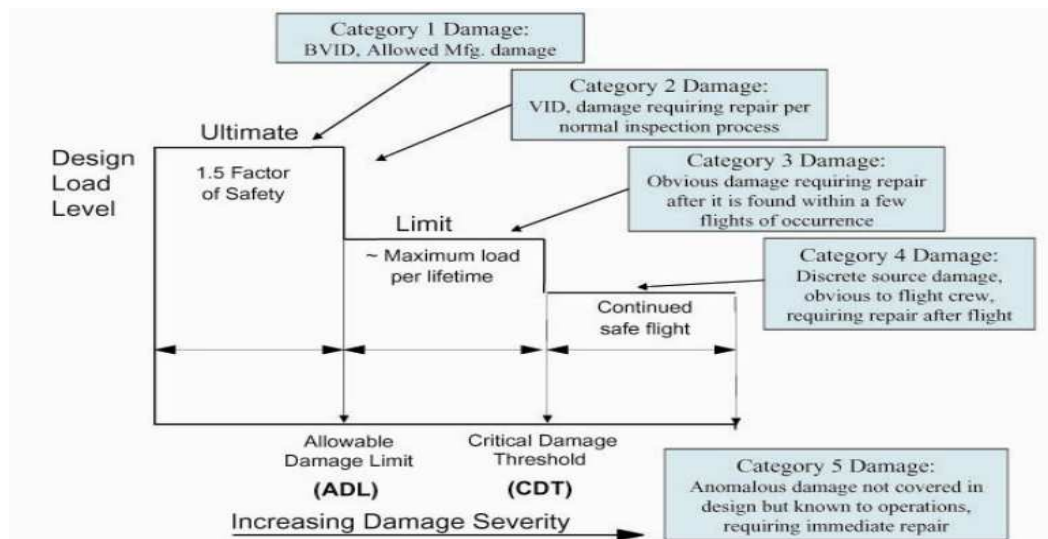


**Figure 1-1 Design load versus damage severity in composite structures [4]**

The first reason why BVID is one of the most dangerous types of damage is that structures with BVID have to carry ultimate design load. The second reason is that BVID is very difficult to detect in regular inspections, where the strength of structures has weakened significantly in compression. The compressive strength may decrease 50% when the structure is subjected to a 10J energy impact which induces a BVID [6]. In this case, it is necessary and important to study and simulate the interlaminar delamination caused by LVI using FE methods.

In order to satisfy the stiffness requirement in a certain direction, the clustering of plies is introduced in a composite laminate. This practice also has some advantages in terms of manufacturing simplicity and readiness [7]. Figure 1-2 illustrates the use of clustering in composite laminates.

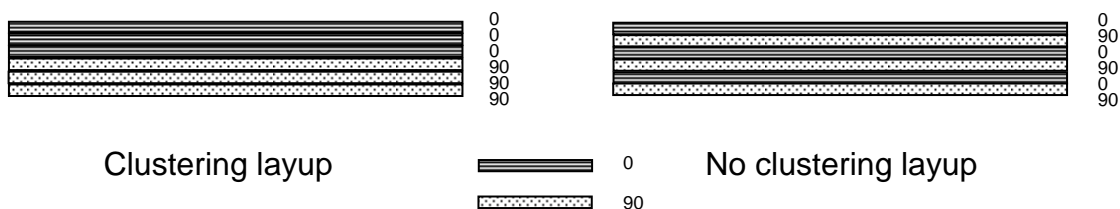


**Figure 1-2 Comparison between clustering and non-clustering layout**

In spite of the advantage of simplicity and readiness with the introduction of clustering layup, the clustering composite laminate is not very efficient in terms of structural behaviours such as damage resistance and damage tolerance. González [8] studied the ply clustering effects on laminated composite plates subjected to low-velocity impact loading. The conclusion that ply clustering reduces the structures capability in terms of the damage resistance was obtained. However, no FE simulation is reported in his research work and FE simulation is needed to achieve certain results which cannot be seen in the test, for example, whether the critical load point means the beginning of a single layer of delamination or several delaminations. Because of this, there is an urgent requirement to use the FE approach to study the interface delamination of composite plates under LVI with consideration of cluster effects.

The mechanics of delamination has been investigated intensively by using fracture mechanics parameters and tools [9]. The Virtual Crack Closure Technique (VCCT) assuming a pre-existing crack in the laminate is the one of the most popular tool to simulate the growth of the delamination [10]. With the emergence of cohesive elements, these elements have attracted more interest in simulating the interface delamination of composite laminates [11-13]. In this research, cohesive elements adopting a bilinear traction separation law were used to simulate delamination using ABAQUS.

BVID is usually caused by LVI. Instead of using dynamic load to simulate LVI, the Quasi-Static Load (QSL) method was used in this study, this is easy to apply and the results are more stable. The main reason is that Brindle [14] carried out both the QSL test and dynamic load test in his research work and came to the conclusion that QSL can be used to simulate the LVI load. The comparison of contact force versus displacement in QSL test and LVI load test is illustrated in Figure 1-3. At the same time, Lee and Soutis [15] obtained the same results that the loading paths of the dynamic load follow the static curve from their experimental research very well.

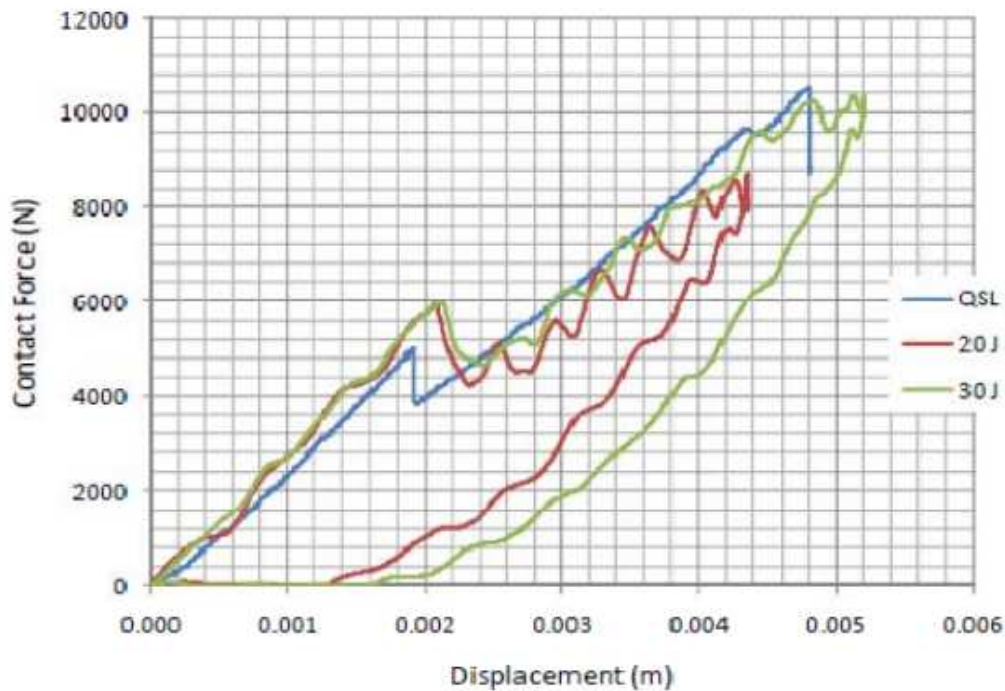


**Figure 1-3 Comparison of reaction load versus displacement [14]**

Accordingly, the contents of this research work are organized as follows:

Firstly, a 2D Finite Element (FE) specimen model of a Double Cantilever Beam (DCB) and an End Notched Flexure (ENF) using commercial FEM software ABAQUS was built.

Secondly, the FE model of a composite plate under QSL but without considering damage was built using continuum shell elements. The agreement of test results with the FEA results validates the capability of continuum shell elements in modelling the composite laminate under transverse load (QSL) conditions.

Thirdly, an FE model which considered interface delamination and matrix crack at the back face of the composite plate was built using cohesive elements to simulate impact responses during impact. Cross-ply laminate was first employed where fewer interfaces could be delaminated.

Finally, the validated method was used to simulate delamination area in quasi-isotropic laminates where more interfaces are available for delamination.

From March 2011 to August 2011, the author joined the Group Design Project (GDP) with the aim of designing a flying-wing commercial aircraft. The aircraft can carry 200 passengers with a range of 7000 miles. The concept design phase was conducted during this period of time. The author's work done in GDP is attached as an appendix at the back of this thesis.

## **1.2 Project Aim and Objectives**

The aim of this research project is to study the clustering effects on laminated composite plates in terms of damage resistance under low-velocity impact loading using the FE method. The FE results will be compared with test results obtained by González [8]. Cohesive elements using the bilinear traction-separation law were applied in this research to simulate interface delamination.

The objectives of this research project are as follows:

1. Build DCB and ENF specimen FE models to analyse mode I and mode II delamination mechanics using cohesive elements.
2. Conduct parameter sensitivity analysis of cohesive elements using DCB and ENF models.
3. Set up a delamination-free FE model to simulate the contact force versus displacement of the impactor.
4. Build a delamination model to predict impact force and delamination area in cross-ply composite laminates subjected to LVI using the QSL approach.
5. Perform simulating of the clustering effects of composite laminates in terms of damage resistance using quasi-isotropic laminates.

## **2 LITERATURE REVIEW**

### **2.1 Introduction**

With the development of composite technology, more and more composite materials are being used in aerospace structures, even in some primary structures such as fuselage, wing structures and tail. However, one of the most dangerous types of damage to composite structures is BVID which is usually caused by LVI. Different impact events will cause different impact damage. Quite a lot of research has been done to classify the impact events and investigate the parameters affecting the definition of the impact events and the damage induced by different impact events.

A review of the literature has shown that lots of research has been done to study the damage induced by LVI and the reduction of stiffness and strength of the damaged structures using test methods. LVI usually induces matrix cracking, fibre and matrix debonding and interface delamination. The factor that influences the safety of the structure the most is interface delamination.

There are many parameters which affect the impact response of composite laminates, such as structure parameters, impactor parameters and environmental conditions. Most of the studies focus on the structural parameters, like stacking sequence, thickness and size, which will affect the damage resistance and damage tolerance of the structures during tests. Some parameters were also used in published papers to describe the impact events, like critical force, peak force and critical energy. Critical force described the sudden reduction of stiffness of the impacted structure.

The major contribution of BVID is delamination which affects the safety of the structure while being difficult to detect. FE methods to predict delamination under LVI also have been conducted comprehensively. These methods include the stress-based failure method, the Virtual Crack Closure Technique (VCCT) based on fracture mechanics and the newly developed cohesive elements method.



Ply clustering is necessary when the enhancement of stiffness in certain directions is necessary. The clustering effects of the laminate plates subject to LVI in terms of damage resistance and damage tolerance have been studied extensively in recent years. The clustering of plies, though with the advantage of simplicity of manufacturing, not only reduces the damage resistance but also the damage tolerance of a plate. But only a few studies have been conducted using FE methods to study the clustering effect of composite plates under LVI. At the same time, the reason why there is no delamination between layers with the same ply angle was not presented very clearly.

## **2.2 Low Velocity Impact**

Sources such as birds, debris, hail and dropped tools can cause impact damage to composite structures during service life [16]. Most of the impact energy is absorbed by elastic deformation and damage mechanisms, rather than plastic deformation because of the brittle property of the composite material [17]. This brittle property makes composite structure vulnerable to impact.

Studies commonly define types of impact as high-velocity and low-velocity. But no consensus has been achieved for these two definitions. It has been suggested that low velocity be defined as less than  $20\text{ms}^{-1}$  [18]. However, Schoeppner [19] considered the upper limit of low-velocity should be  $40\text{ms}^{-1}$ . Olsson [20] suggested that high-velocity impact be defined as ballistic impact which induces penetration of the laminates and low-velocity impact as that producing no penetration from impact.

The impact duration significantly affects the impact behaviour of laminates and provides another way to define the impact event. In the research results of Olsson [20], impact events were divided into three different categories, dilatational waves, flexural waves and Quasi-Static, as shown in figure 2-1.

The impact event illustrated in figure 2-1-a is usually called ballistic impact with through-the-thickness response. The impact time is very short and in most cases will induce damage which is easily detectable. The impact event in figure

2-1-b is typically caused by hail and runway debris which are lighter but have relatively high speed. The impact time is longer than ballistic impact with the impact response dominated by flexural waves and shear waves. The impact event shown in figure 2-1-c is usually induced by dropping of heavy tools which are heavier but with low velocity. The impact time is much longer than the times required by the waves to reach the boundary of the plates, so the impact response will be affected by boundary conditions and plate size. This impact is also called quasi-static impact because the reaction load and impactor displacement have the same relation as in a static load condition. The latter two impact events usually cause BVID which is very critical in composite structures design.

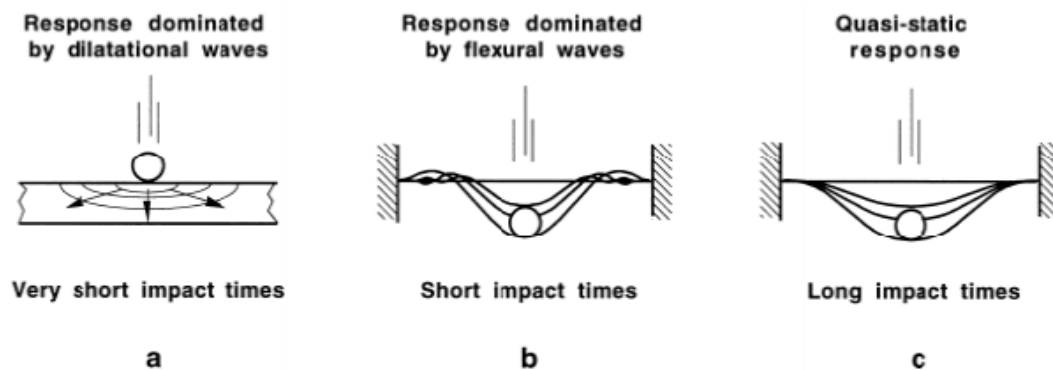


**Figure 2-1 Response types during impact on plate [20]**

Because of the difficulty of using impact duration to classify the impact events, impactor-laminate mass ratio was also introduced in Olsson's [20] paper to help define the impact events. An impactor-laminate mass ratio less than 0.23 will result in a flexural wave response, while a mass ratio more than 2.0 will have a quasi-static response. The conclusion that small-mass impactors cause much larger delamination areas than the large-mass impactors with the same kinetic energy was also found in the research results of [21, 22, 23].

In this research, intensive study focuses on low-velocity impact event as shown in figure 2-1-c. Brindle [14]'s test data were first used to validate the FE simulation of reaction force versus displacement of the impactor. In Brindle's tests, the velocities of impact are from 1.21 m/s to 2.97 m/s and the impactor-

laminate mass ratio is about 69 which satisfies the requirements of low-velocity impact. Furthermore, QSL test data show very good agreement with the LVI experimental data [3]. At the same time, Lee and Soutis [15] observed the same phenomenon where the loading paths of the dynamic load follow the static curve very well through their experimental research. This explains why an FE model employing QSL load can be used in this research to investigate the LVI test.

### **2.3 Impact Damage Types**

As can be seen in Figure 2-2, the primary damage resulting from low-velocity impact can be categorized into five different types [24].

1. Contact damage which is always localized damage and the severity of this damage mainly depends on the impact load. The signs of contact damage are matrix and fibre crushing within the limit of the thickness. Usually this localized crushing damage is not considered in FE simulations because the damage is small and limited.
2. Transverse shear stress induced delamination happens in the middle of the plate where the maximum shear stress exists.
3. Failure of the impact faces due to the compressive strains which include matrix and fibre failure.
4. Matrix fracture or crack induced by tensile strains on the back face of the plate. The existence of the matrix crack does not affect the stiffness of the plate significantly. But delamination starts at the crack tip at interfaces between plies with different ply angles [18].
5. Delamination due to back face matrix cracking [24]. The delamination in the middle plane is mainly caused by transverse shear stress. But delamination near the back face is mostly induced by peel stress in the interfaces between plies with different ply orientations.

In the research work [25], impact damage events were defined in three stages as illustrated in figure 2-3. At the first stage as can be seen in figure 2-3-a, only a single bending matrix crack and shear matrix cracks were observed in the bottom layer and second bottom layer respectively. A small delamination was

detected in the lowest interface along the bending crack. The same crack and delamination pattern was also reported in [26]. After that, more shear matrix cracks were detected in the middle layers with inclined angle of about 45°. Delamination initiated from the crack tip propagated unstably which caused a sudden load drop of the impactor. Finally, more matrix cracks and delamination developed with the increase of impact load.

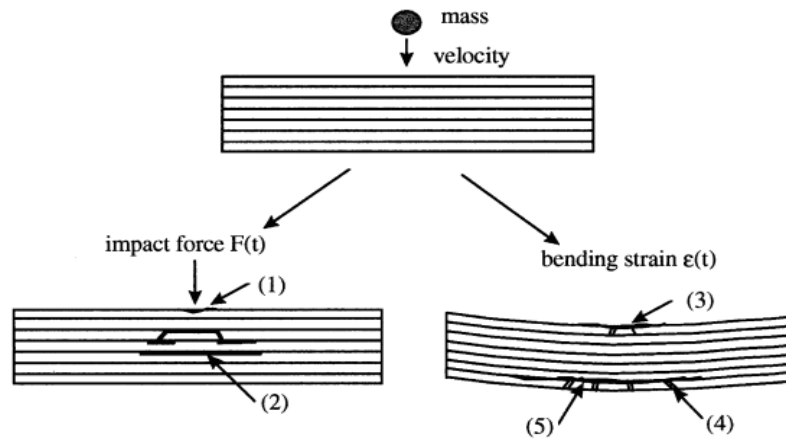


Figure 2-2 Nature of LVI damage in composite plates [24]

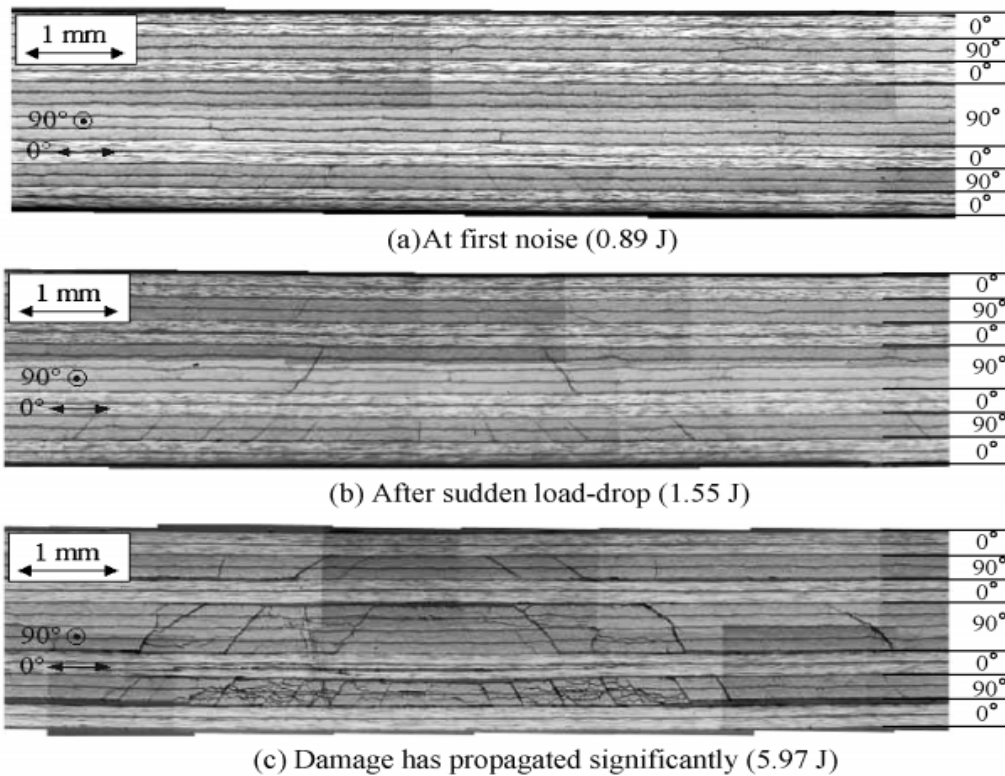
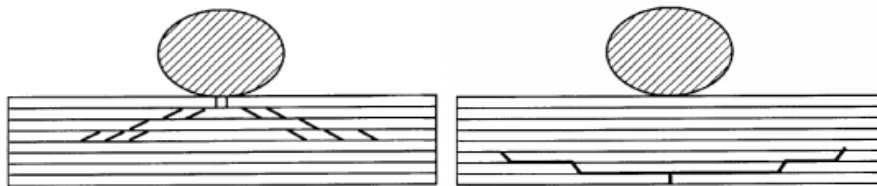


Figure 2-3 Micrographs of the cross-section at different energy levels [25]

Delaminations in the two lowest interfaces were larger than others and more shear matrix cracks were found in the back side layers.

Composite plate and stiffened panel impact tests done in [18, 27] also show that the damage types of structures with different configuration are different under the same impact energy. As illustrated in figure 2-4 [28], under LVI, a stiff structure as shown on the left will result in more middle plane matrix cracks and delamination which is attributed to the higher impact force. At the same time, a flexible structure as shown on the right will develop more surface damage, like the matrix crack at the back face, which is mainly caused by the larger bending strain and higher residual tension stress.



**Figure 2-4 Damage patterns of stiff and flexible plates [28]**

It is well known that delamination initiation and growth are affected by the existence of matrix cracks [18, 28] and the interaction between delamination and matrix cracks has been studied [29, 30]. The conclusion was that delamination started due to the high tension stress at the interfaces because of the existence of matrix cracks. The interaction between matrix cracks and delamination also explained the peanut shape of the delamination. However, recent FE simulation studies [25, 31, 32, 62] found that the delamination prediction in clustered laminates agreed well with the experimental data without considering the shear matrix cracks. These research results show that the relation between shear matrix cracks and delamination is not very clear for cross-ply composite laminates.

The experimental evidence that no bending matrix cracks were clearly identified at the back surface of a non-clustering composite plate shows that bending matrix simulation is not necessary for non-clustering plates [62]. Furthermore, the experimental results of González [11] found no clear peanut shape of

delamination with its main axis along the fibre direction in the lower ply of non-clustering plates. However, for clustering plates, both FE simulation and experimental results presented peanut shape delamination with its main axis along the fibre orientation at the lower layer. The peanut delamination is mainly attributed to the observed bending matrix cracking at the back face along the fibre direction.

Intensive studies by [33, 34, 35, 36, 37] have been conducted to predict the damage types due to LVI. They concluded that matrix cracking and interface delaminations are the main damage forms in composite laminates subjected to LVI. At the same time, matrix crack tips were seen as a delamination initiation point at interface between plies with different layup angles [18, 35, 38, 39]. Accordingly, bending matrix cracking at the back face, shear matrix cracking at inner layers and interlaminar delamination were all considered in composite laminate due to LVI in this paper.

Delamination is basically caused by three loading modes, as shown at figure 2-5 [40]. Mode I deformation is driven by peel stress while modes II and III deformation are driven by interlaminar transverse shear stress. Davies [41] assumed that delamination propagation in a simply supported circular laminate plate was dominated by mode II fracture. Irving [42] considered that the impact damage is a function of  $G_{IIC}$  (Mode II) properties. The fracture toughness of mode I and mode II was experimentally determined using the Double Cantilever Beam test and the End Notched Flexure test respectively.

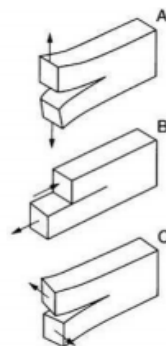


**Figure 2-5 Mode I, II and III crack deformation [40]**

## 2.4 Parameters in Impact

The parameters which will affect the impact response can be classified into three different groups: structural parameters, impactor parameters and environmental conditions. Parameters like shape, thickness, size, material properties, ply stacking sequence, and boundary conditions are categorized as structural parameters. Impactor parameters comprise shape, diameter, material properties, weight, angle of incidence and impact velocity [8].

A number of experimental tests were conducted to study these parameters in impact events. Davies [18] found that the more popular plots showing damage area versus impact energy were very chaotic. Under the same impact energy, the structural parameters, like shape, size and boundary conditions will affect the impact response significantly. For example, a small plate is stiffer than a large plate which will result in a larger impact force on the small plate. So, the relationship between impact force and damage area as shown in figure 2-7, was used instead of that between impact energy and damage area as this means there is no need to consider plate size and other effects. However ply stacking sequence was not considered in this research work. From the research results a small piece of test specimen can be used to simulate impact damage in a large in-service structure when the same impact force was employed.

At the same time impactor geometry can dramatically affect the impact damage of a plate [14]. The impactor shapes shown in figure 2-6 created different type of damage in terms of fibre breakage, matrix crack and delamination [43, 44].

Research results indicate that a hemispherical tup has the highest peak load but the shortest contact time. Conical tups usually generate lowest peak load but longest contact duration [43]. Penetration damage always comes with the conical tup impact which will cause fibre breakage. Greatest impact damage is introduced by hemispherical tup under the same impact energy [44].



**Figure 2-6 Hemispherical, ogival and conical Impact Tups [43]**

As mentioned in chapter 2.2, under the same impact energy, different masses of the impactor will not induce identical results. A higher velocity is dominated by flexural wave and usually cause localized damage. A larger mass impactor always results in quasi-static impact response which causes interface delamination. Feraboli [45] found that the impact damage is almost the same with impactor mass in the range of 1 to 20 kg.

## **2.5 Critical Force and Critical Energy**

The impact event can be described as follows:

1. impact energy – kinetic energy of the impactor;
2. peak force – maximum force recorded during the impact event;
3. critical force – threshold force for onset of delamination [37];
4. critical energy – impact energy analogous to critical force;
5. dissipated energy – energy absorbed in damage initiation and propagation [46].

As mentioned in the previous chapter, impact force against damage area plots, as shown in figure 2-7 [18], can be employed to describe the impact event without external effects like size, shape and boundary condition of the laminate plate. As can be seen in the figure 2-7, there is an obvious threshold force below which no delamination happens. This force is called the critical force.



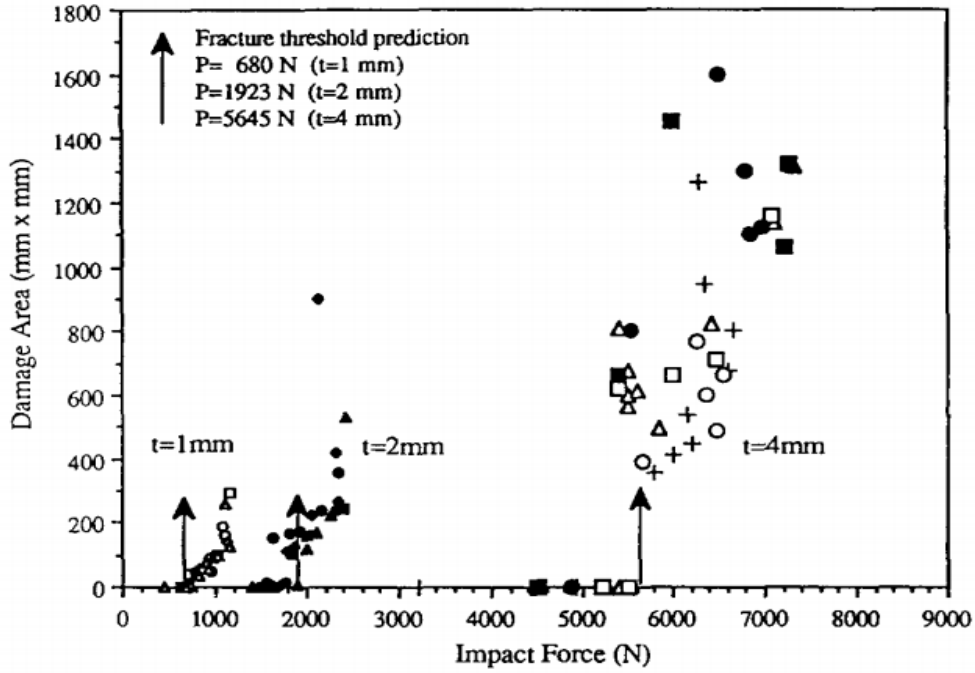


Figure 2-7 Impact force versus damage area for different plate size [18]

The critical force for a Quasi-Isotropic (QI) laminate is calculated using the following equation:

$$P_c^2 = \frac{8\pi^2 E t^3}{9(1-\nu^2)} G_{IIC}$$

Where E is the effective flexural modulus; t is the thickness of the laminate;  $G_{IIC}$  is the mode II critical strain energy release rate;  $\nu$  is Poisson's ratio [41].

In an impact event, when the critical force reaches a threshold value, there is instantaneous large delamination caused by unstable crack propagation which often leads to sudden drop of impact force. The critical force does not mean the beginning of damage, because small matrix cracks and sub-critical delamination may happen at lower contact force [8, 37].

This criterion was further developed by [47, 48] with the consideration of multi-delamination through the thickness which is defined as:

$$F_{dn_d}^{stat} = \pi \sqrt{\frac{32DG_{IIC}}{n_d + 2}}$$

Where  $D$  means the bending stiffness of the composite plates,  $n_d$  is the number of delamination interfaces. When  $n_d$  equal 1, the above criterion becomes that which is given by Davies [41]. At the same time, the critical load is independent of the size and boundary conditions of the plate [47, 49, 50].

After studying the clustering effect on the critical load using three plates with different stacking sequence, a new criterion was developed taking into consideration the clustering effect [8]. The critical load is calculated as:

$$F_{dn_d}^{stat} = 4\pi\sqrt{2D^*G_{IIc}} \left( -1 + \frac{t^3}{(t - n_d^*h_p)^3 + n_d^*h_p^3} \right)$$

Where  $D^*$  is the effective stiffness of orthotropic plates;  $n_d^*$  is the interface numbers starting from the back face of the plates. Fewer interfaces are considered by assuming no delamination interface between plies with the same fibre orientation.  $h_p$  is the clustering thickness which includes the thickness of plies with the same fibre orientation together;  $t$  is the total thickness of the plates. The equation above was found to be capable of calculating the critical force of composite plates taking into consideration the clustering effect.

## 2.6 Finite Element Modelling of Impact of Composites

In the last few decades, lots of FE simulations have been conducted to predict the damage initiation and propagation in composite laminates under low-velocity impact.

The stress-based failure model was proposed for predicting interlaminar delamination subjected to LVI assuming the explosive nature of damage which was undergone in all the impact tests on composite laminate [24]. Delamination starts when the Interlaminar Shear Strength (ILSS) or the through-thickness tensile strength was exceeded. In this research, both indentation and in-plane fibre and matrix failure were considered by employing an empirical contact law and the Chang and Chang criterion separately. The conclusion was that the flexural stiffness of the plates is unaffected by internal delamination unless the delamination reaches a free edge where there is no slide constraint of the

adjacent plies. However in-plane fibre or matrix degradation will reduce the plate's flexural stiffness when the plates have large deformation.

Subsequently, the Virtual Crack Closure Technique (VCCT) which adopted linear elastic fracture mechanics, had been used extensively [51]. However, this method is very sensitive to the configuration of the mesh and the size of elements and an initial crack in the FE model is required to carry on the simulation. Apart from that, the VCCT method also requires an adaptive mesh approach in certain circumstances to track the varying shape of the crack tip [52, 53]; this is not yet available in any of the major analysis codes. Because of these drawbacks to the VCCT method, the fact that the cohesive elements model deals with the limitations of the VCCT method aroused some interest in the field of predicting composite impact damage [25, 31, 54, 55, 56, 57, 58, 59, 60 and 61].

The bilinear traction separation law was adopted in the cohesive element to simulate the damage initiation and propagation. Stress-based criteria were employed to simulate the delamination initiation while fracture mechanics energy criteria were used to predict damage evolution [61]. The validation of cohesive elements was performed using a simple model like Double Cantilever Beam (DCB) and End Notched Flexure (ENF) [55, 56, 57, 58]. Only a few projects studied the impact damage of composite laminate using 3D FE models to simulate different delamination sizes and shape at different interfaces through the thickness [25, 31, 61, and 62].

Aymerich et al [61] carried out research to predict the delamination damage in laminates under low-velocity impact using cohesive interface elements. FE models using cohesive elements with a bilinear traction-separation law were first validated using the standard mode I and mode II fracture toughness tests, like DCB and ENF. The same methodology used in the previous FE model was applied to conduct the impact simulation of cross-ply composite laminates. The FEA results and experimental observations showed good agreement in terms of orientation, shapes and size of delaminations.

After that, Aymerich [62] studied the impact reaction and the damage process of cross-ply laminated plates with clustered and interspersed ply stacking using a FE model. For grouped laminates, the FEA prediction shows good agreement with the experimental data. However, in interspersed laminates, the model was validated to simulate the shape of the damage area but the delamination sizes between interfaces are not accurately predicted because of the complicated damage processes.

In this paper, the cohesive element method was adopted to simulate the impact damage of composite laminates taking into account the ply clustering effect.

## **2.7 Clustering Effect**

The ply clustering effect of composite laminates under low-velocity impact was widely studied [65, 66, and 67] in terms of damage resistance and damage tolerance. Damage resistance is different from damage tolerance. Damage resistance is the structure's ability to resist the damage initiation while damage tolerance is the residual strength after the damage. In this research only damage resistance is considered.

Ply clustering decreases the damage resistance of a plate subjected to low-velocity impact [8]. There are two main reasons which contribute to this phenomenon. The first is that the interface shear stresses are increased between different ply groups due to the difference in increased bending stiffness. This larger shear stress will also lead to more delamination [68, 69]. Secondly, because more or larger delamination usually happens at interface with different ply orientation [8], ply clustering also reduces the number of interfaces where delamination is expected to occur, which in turn, leads to larger delamination areas when same amount of energy is absorbed. However, the reason why there is no delamination at the interface with the same fibre orientation is not very clear. Three factors, transverse shear stress distribution due to impact load, residual stress arising from the curing process and fibre bridging effect are studied with the aim of clarifying this question in chapter 3.4.

### 3 METHODOLOGY

#### 3.1 Introduction

As discussed above, interface delamination and matrix crack were considered in the numerical simulation. Cohesive elements employing the bilinear traction separation law were used to simulate delamination and matrix crack. Cohesive elements were inserted between plies with different layup orientations to simulate interface delamination. To simulate matrix cracking, which usually develops in the lower grouped layers along the fibre direction, vertical cohesive elements were modelled on the plane parallel to the fibre direction as illustrated in figure 3-1.

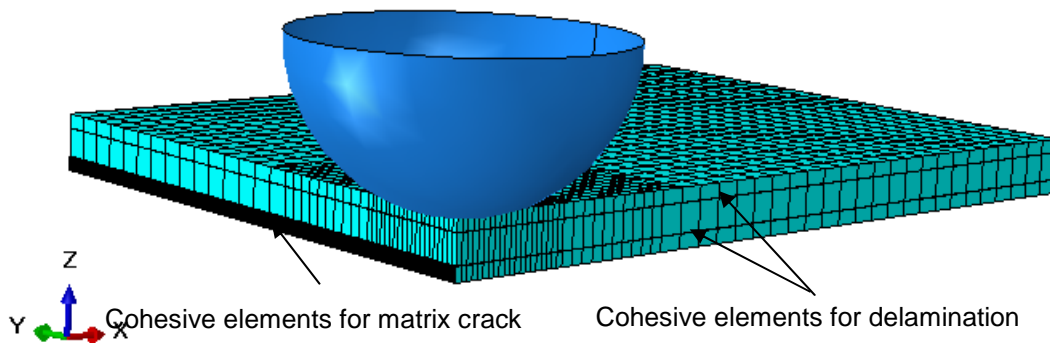


**Figure 3-1 Cohesive elements placement illustration**

Composite laminates were modelled using continuum shell elements. Continuum shell elements look like solid elements while their kinematic and constitutive behaviour is similar to shell elements [72].

The commercial software package ABAQUS 6.10 was used to carry out the finite element analysis. The nonlinear solver in ABAQUS Standard was employed to simulate the damage process given the fact that static load was used in the model.

### 3.2 Cohesive Element

Several traction-separation laws are available in published papers to represent the loading response of the interface between plies [73]. However, many studies found that simulation results were not sensitive to the cohesive law [73, 74]. In this research, cohesive elements adopting the most popular bilinear traction separation law were applied to simulate interface delamination and matrix crack at the back face in the fibre direction. The bilinear cohesive element behaviour adopted under mode I and mode II/III are shown in figure 3-2. The horizontal axis shows the relative displacement between the upper and low interface surfaces while the longitudinal axis shows the normal (mode I) and tangential (mode II/III) traction. The area under the traction-separation curve is equal to the energy required to delaminate the interface.

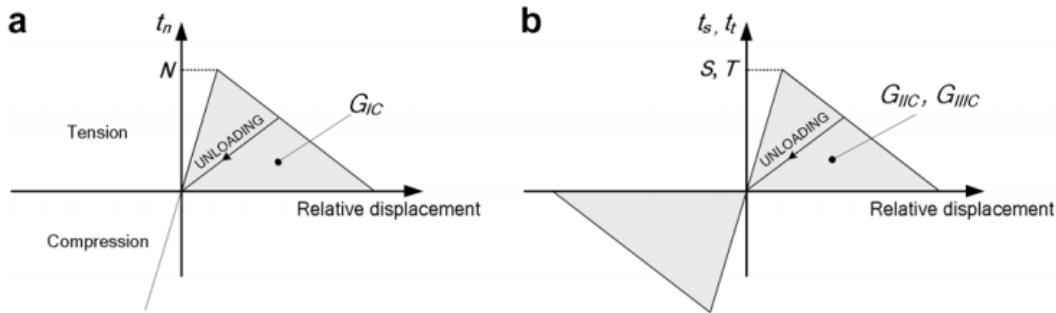


**Figure 3-2 Traction-separation law for mode I and mode II/III fracture [62]**

As illustrated in figure 3-2, an initial linear stage is observed until the traction reaches its maximum. After the traction reaches its peak, a linear softening stage is also seen, which shows that decohesion of the interface is already taking place in this phase. At the end of the softening stage, the traction reaches zero, which implies the complete delamination of the interfaces. The unloading process follows a linear path which goes directly through the origin as the stiffness reduces. In the lower left of figure 3-2-a, the cohesive interface will retain its original stiffness when the compression load exists at the interface, which in turn ensures that interpenetration is avoided at a delaminated interface.

### 3.3 Continuum Shell Element

Unlike a conventional shell element which defines the geometry at a reference surface, the continuum shell element discretizes an entire three-dimensional part. Continuum shell elements allow for thickness change in two sides and thus are suitable for contact simulation [72].

Though continuum shell elements look like 3D solid elements from a modelling point of view, their kinematic and constitutive behaviour is similar to conventional shell elements. Conventional shell elements have both displacement and rotational degrees of freedom whilst continuum shell elements only have three displacement degrees of freedom. Also the section property is used to define the thickness of conventional shell elements whereas continuum shell elements use element nodal geometry. The differences between these two shell elements are illustrated in figure 3-3.

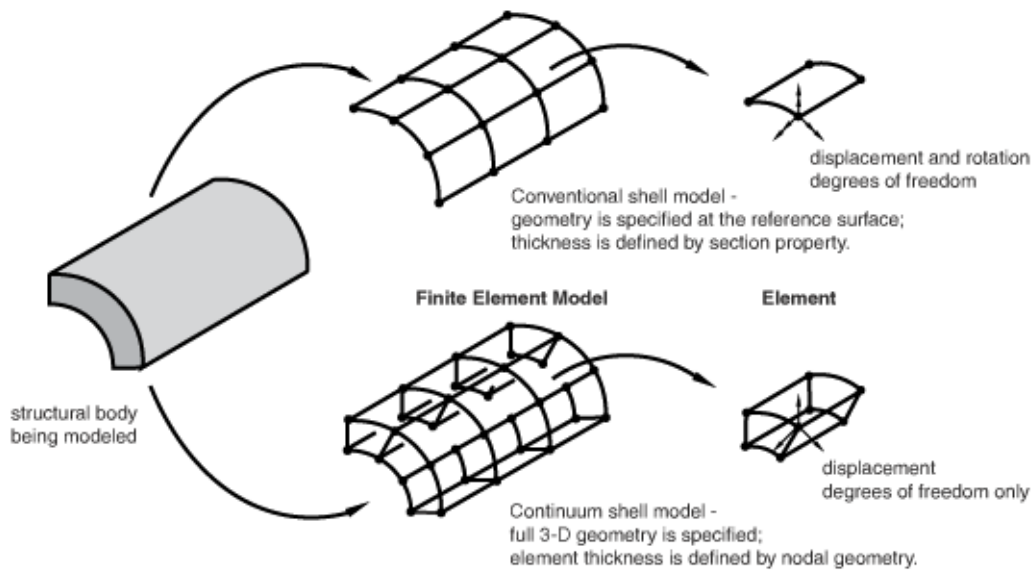
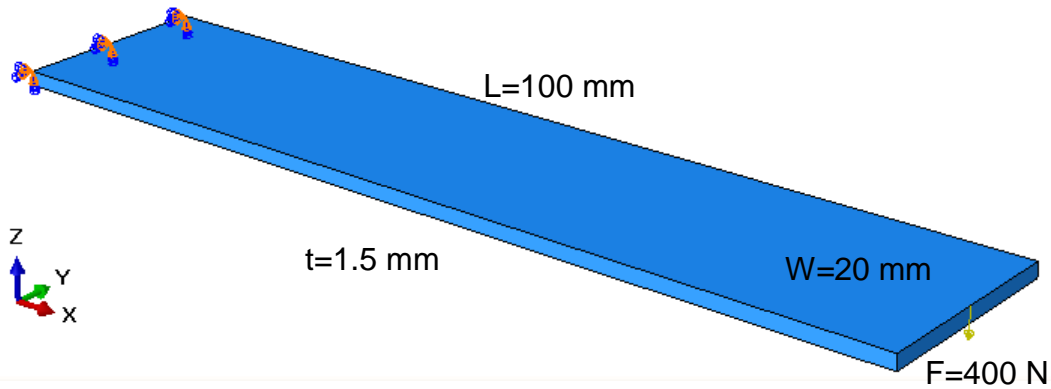


Figure 3-3 Conventional shell element versus continuum shell element [72]

### 3.4 Stress Study of Clustering Laminate

#### 3.4.1 Transverse Shear Stress Distribution

At first, a simple FE model was built to study the transverse shear stress distribution through thickness of the plate. The stacking sequences proposed are  $[0_{12}]$ ,  $[90_3/0_3]_s$  and  $[(90/0)_3]_s$  which are designated as L1, L2, L3 in this thesis. The set up of the model is illustrated in figure 3-4.



**Figure 3-4 Model for transverse shear stress distribution study**

Under the above configuration, the maximum transverse shear stress for an isotropic material can be calculated using classical beam theory as follows:

$$\max \tau_{xz} = 1.5 \frac{F}{A} = 1.5 \frac{F}{Wt} = 1.5 \frac{400}{1.5 \times 20} = 20 \text{MPa}$$

Where F is the applied force, A is the cross sectional area of the plate, W is the width of the plate while t is the thickness.

Two FE models employing conventional shell elements and plane strain elements separately were used to investigate the transverse shear stress distribution along the thickness of the plate. General-purpose conventional shell elements S4R were used which allow transverse shear deformation in one model [72] while two dimensional plane strain elements CPE4 were employed in the other. Figure 3-5 and 3-6 shows the FE models of conventional shell and plane strain elements respectively.



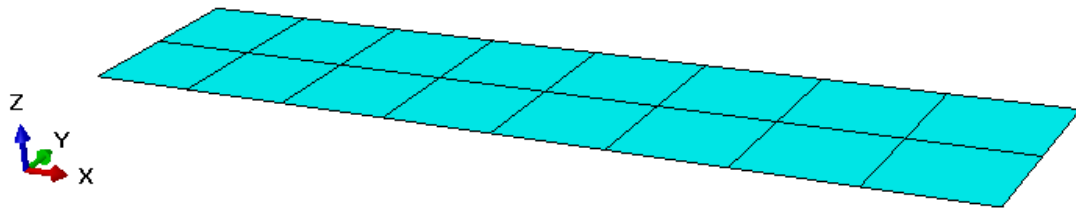


**Figure 3-5 FE model using conventional shell elements**

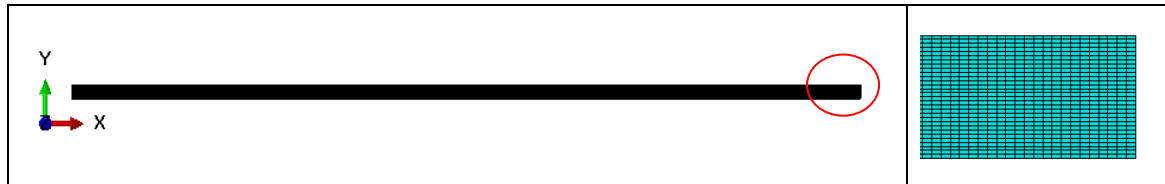


**Figure 3-6 FE model using plane strain elements**

At first, both conventional shell and plane strain elements FE models using isotropic material properties were built to validate the FE model. After that FE models were constructed using orthotropic composite material properties to study the transverse shear stress distribution along thickness direction of the plate. The material properties for isotropic and orthotropic material are listed in table 3-1.

**Table 3-1 Material properties for isotropic and orthotropic materials**

Isotropic material					
E(MPa)			ν		
70000			0.3		
Orthotropic material					
E <sub>1</sub> (MPa)	E <sub>2</sub> (MPa)	ν <sub>12</sub>	G <sub>12</sub> (MPa)	G <sub>13</sub> (MPa)	G <sub>23</sub> (MPa)
142000	8000	0.3	4000	4000	4000

The transverse shear stress distribution along the thickness for an isotropic material plate can be seen in figure 3-7. Both conventional shell and plane strain elements FE models were validated by comparing the maximum transverse shear stress results from the theoretical calculation and the FE results.

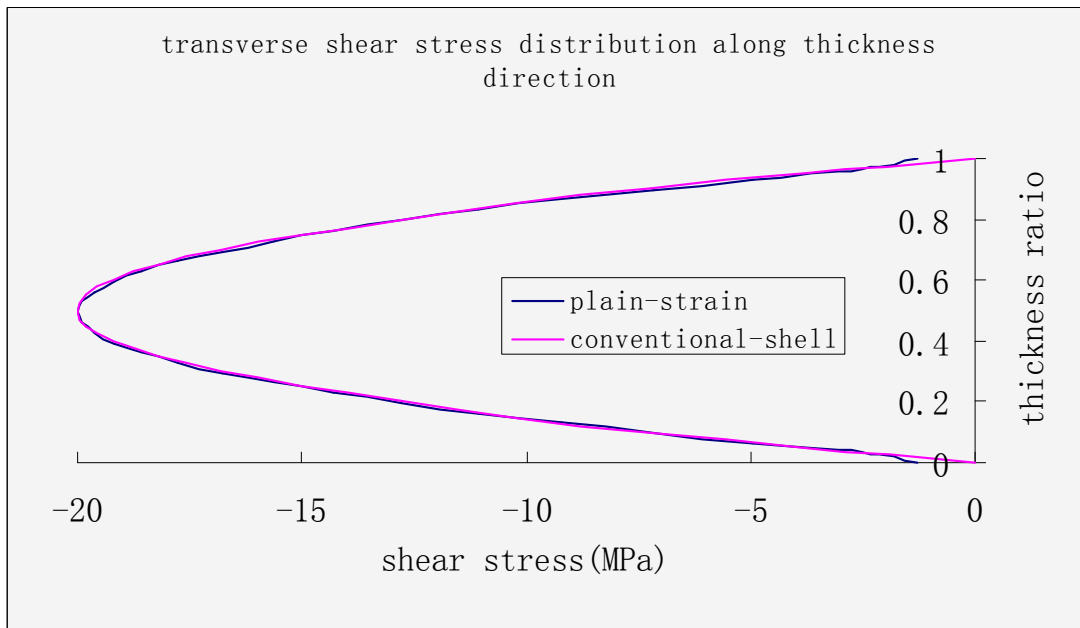


**Figure 3-7 Transverse shear stress distribution for isotropic material**

The axial strains located at the middle of the plate along the thickness for L1, L2 and L3 are illustrated in figure 3-8 using conventional shell elements. The axial stresses along the thickness for L1, L2 and L3 are shown in figure 3-9. The transverse shear stress distribution along the thickness for L1, L2, L3 and isotropic material using conventional shell elements can be seen in figure 3-10.

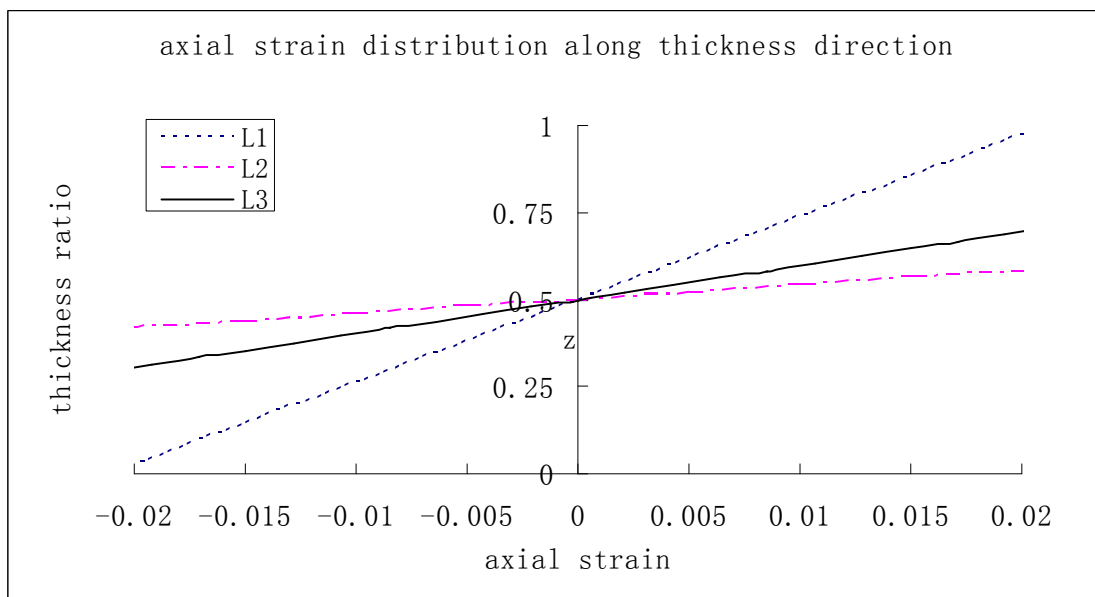


**Figure 3-8 Axial strain distribution of L1, L2, L3**

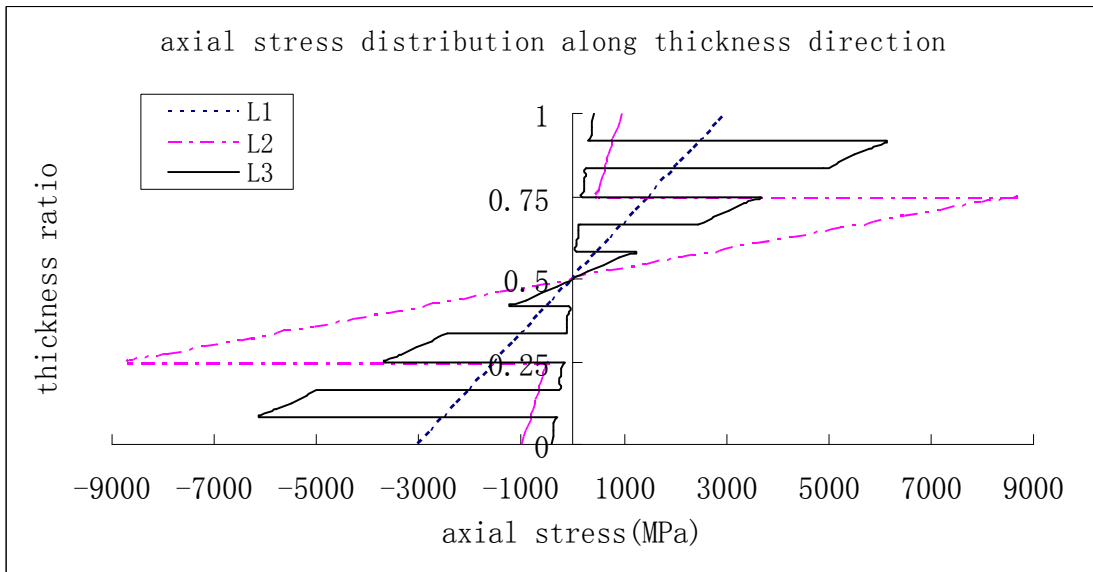


**Figure 3-9 Axial stress distribution of L1, L2, L3**

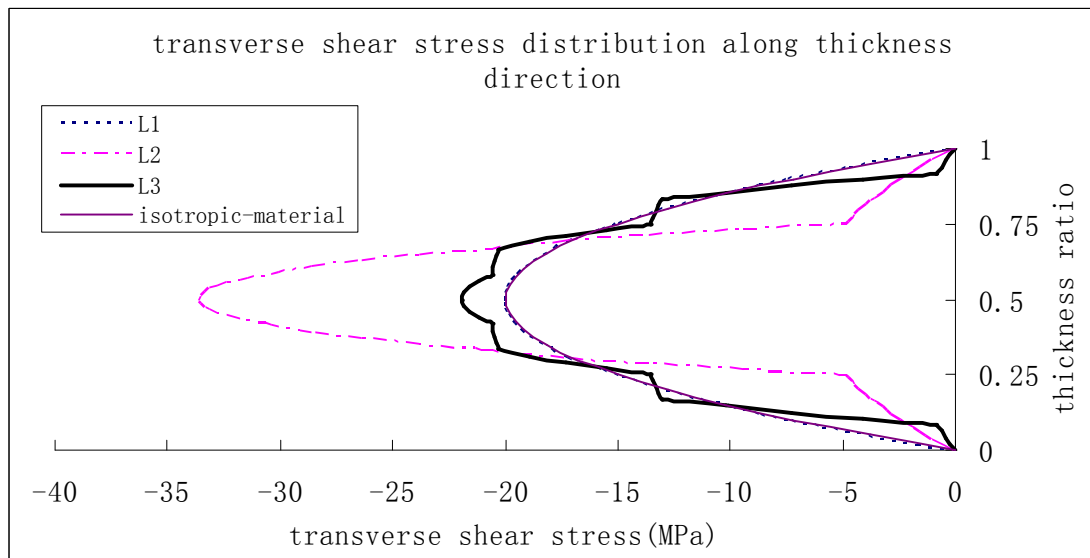


**Figure 3-10 Shear stress distribution of L1, L2, L3 and isotropic material**

The transverse shear stress distribution along the thickness for L1, L2, L3 and isotropic material using plane strain elements can be seen in figure 3-11.

As illustrated in figure 3-10 and 3-11, with the ply clustering, the maximum transverse shear stress is a little bit more than 33 MPa which is higher than the no clustering plate L3. However, the maximum shear stresses happen at the middle plane of the plate where zero normal stress exists. This also means that the maximum shear stress does not exist at the interface with different fibre

orientation where the delamination usually starts. Furthermore the shear stress at interfaces with different fibre orientation, which are located at 25% or 75% of the thickness, for the plate L2 is about 5 MPa which is much less than the stress level of the no clustering interfaces in L3.

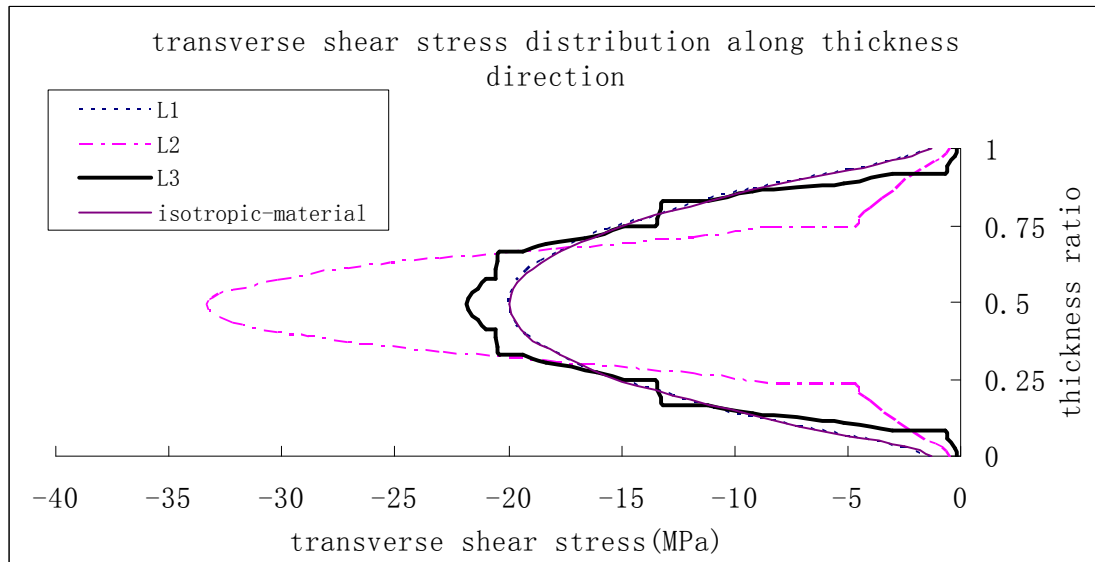


**Figure 3-11 Shear stress distribution of L1, L2, L3 and isotropic material**

In conclusion, ply clustering does not necessarily increase the transverse shear stress at the interface where fibres have different orientation. At the same time, both conventional shell elements and plane strain elements are calibrated using comparison between figure 3-10 and figure 3-11.

### 3.4.2 Cure Induced Residual Stress

Secondly, an FE model employing continuum shell elements to investigate the residual transverse shear stress and in-plane stress was constructed. A scheme of the model is shown in figure 3-12. During the curing process of the composite plate, the temperature will usually reach 180 °C and the structure of the plates is moulded during that time. After curing, the composite structures will be used at room temperature. The temperature difference causes residual transverse shear stress and in-plane stress between adjacent plies with different fibre orientation.

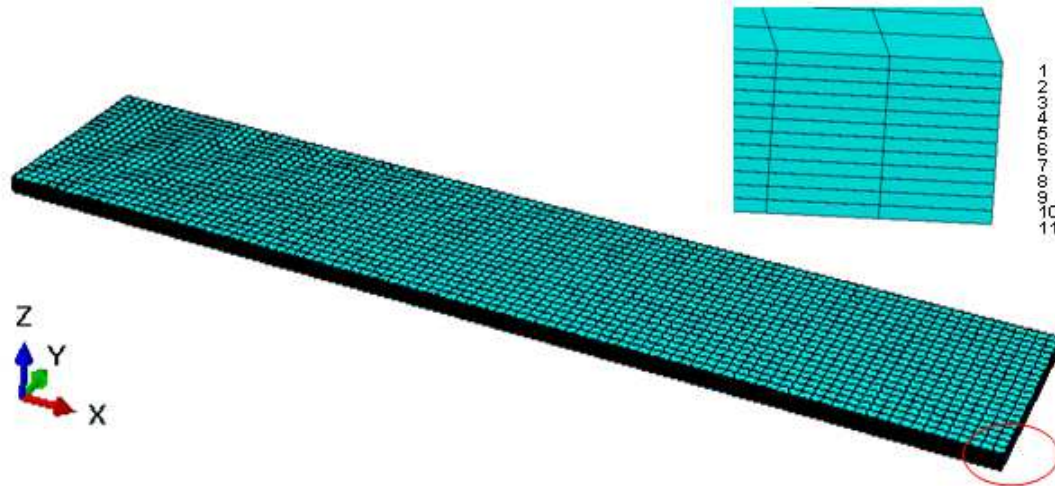


**Figure 3-12 Model for thermal expansion study**

In the above model, 11 layers of cohesive elements were placed at the interfaces to capture the transverse shear stress caused by thermal expansion. Twelve layers of continuum shell elements were built to find the in-plane stress due to thermal expansion.

The stacking sequence of the plate is  $[90_3/0_3]_s$  and the temperature difference is  $160\text{ }^\circ\text{C}$ . Coefficients of thermal expansion were found to increase when the working temperature increased [71]. In this paper, the coefficients of thermal expansion in fibre and fibre transverse direction were  $1.16\text{e}^{-6}/^\circ\text{C}$  and  $28.99\text{e}^{-6}/^\circ\text{C}$  with the temperature at  $30\text{ }^\circ\text{C}$  [71].

The transverse shear stress distribution along the interface in the x-z direction is illustrated in figure 3-13. The transverse shear stress distribution along the interface in the y-z direction is illustrated in figure 3-14.

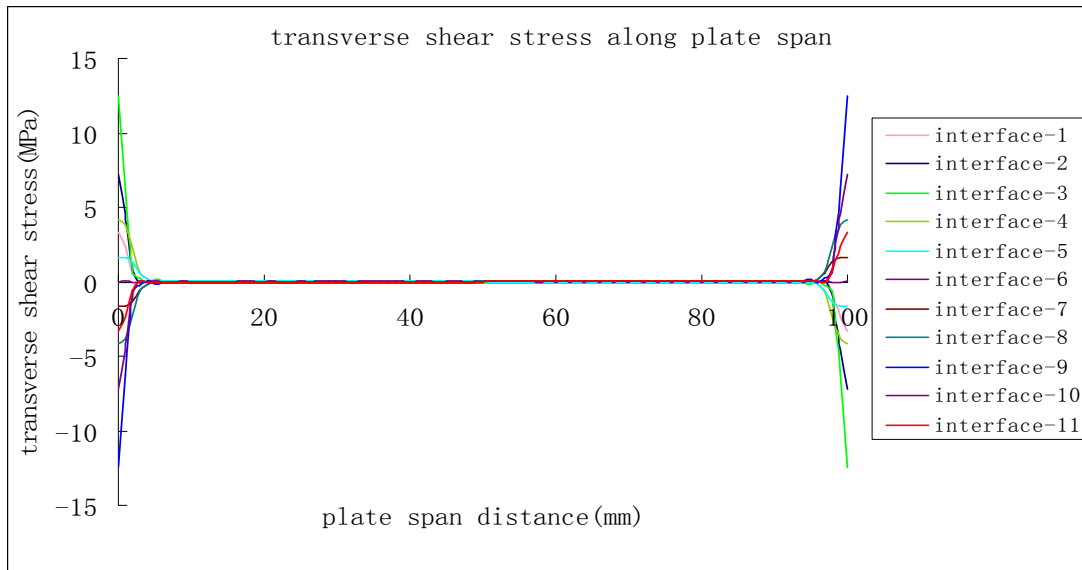


**Figure 3-13 Shear stress distribution along the interface in the x-z direction**

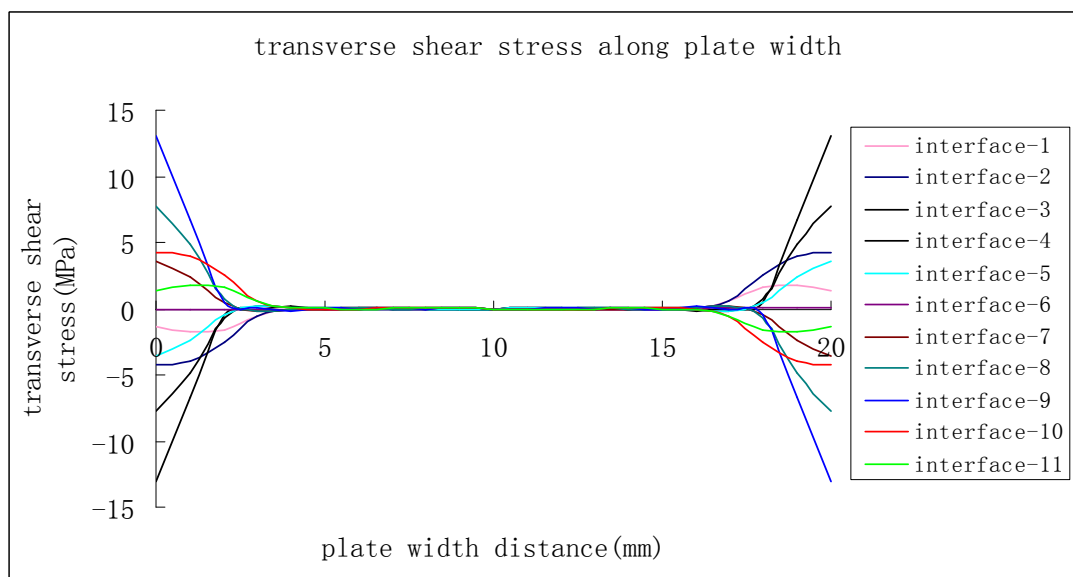


**Figure 3-14 Shear stress distribution along the interface in the y-z direction**

As can be seen in figure 3-13 and figure 3-14, the maximum transverse shear stress happens at the third and eighth interface where layers on both sides have different fibre orientations. At the same time, the maximum value of the transverse shear stress is about 13 MPa in both directions. The transverse shear stress at interfaces with the same fibre orientation is lower than the stress level at interfaces with different fibre orientation. The transverse shear strength

is about 80 MPa which means the residual transverse shear stress does not have a significant effect on the existence of delamination between layers.

Another important feature of the stress distribution is that the transverse shear stress only exists at the four boundaries of the layer. The main reason is that continuous deformation is expected for the composite plate with 6 different layers bonded together. Under the thermal load, the layers with different fibre directions tend to deform separately, but, in fact the deformations are very smooth which is mainly because of the transverse shear stress which arises at the edge. In the area away from the boundary, the displacement of adjacent plies is the same which means there is no transverse shear stress between them.

Using the configuration of plates in this chapter, the residual in-plane stress can be calculated using the equation below [71]:

$$f_A^R = \frac{\Delta T E_1 E_2 A_2 (\alpha_2 - \alpha_1)}{(A_1 E_1 + A_2 E_2)}$$

Where  $\Delta T$  is the temperature difference,  $E_1$  and  $E_2$  are young's modulus in 11 and 22 direction,  $A_1$  and  $A_2$  are the total cross-section area in 11 and 22 direction,  $\alpha_1$  and  $\alpha_2$  are coefficients of thermal expansion in 11 and 22 direction. 11 is in the fibre direction and 22 is the in fibre transverse direction.

$A_1$  equals  $A_2$  because of the balanced symmetric layup of the composite plate which means the numbers of  $0^\circ$  plies and  $90^\circ$  plies are the same, so the residual in-plane stress was calculated as below:

$$\begin{aligned} f_A^R &= \frac{\Delta T E_1 E_2 A_2 (\alpha_2 - \alpha_1)}{(A_1 E_1 + A_2 E_2)} = \frac{\Delta T E_1 E_2 (\alpha_2 - \alpha_1)}{(E_1 + E_2)} \\ &= \frac{160 \times 142000 \times 8000 \times (28.99 - 1.16) \times e^{-6}}{142000 + 8000} \\ &= 33.72 \text{ MPa} \end{aligned}$$

Residual in-plane stress in the fibre transverse direction was also investigated using the FE model mentioned above. As illustrated in figure 3-15 and 3-16, the tension stress in the fibre transverse direction was about 33 MPa which is about

half of the matrix tension strength. Because of that, the residual in-plane stress in fibre transverse direction has a significant influence on the matrix damage. Under the impact load conditions, the matrix crack will first happen because of the high residual stress arising from the curing process then the matrix crack acting as the initial point of delamination will cause more delamination at the interface.

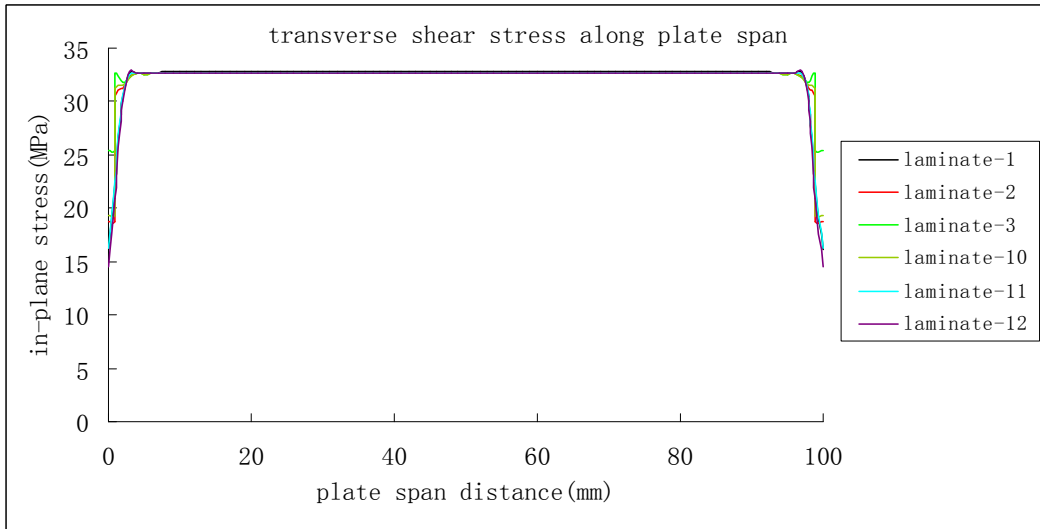


**Figure 3-15 Residual in-plane stress for layer oriented at 90°**

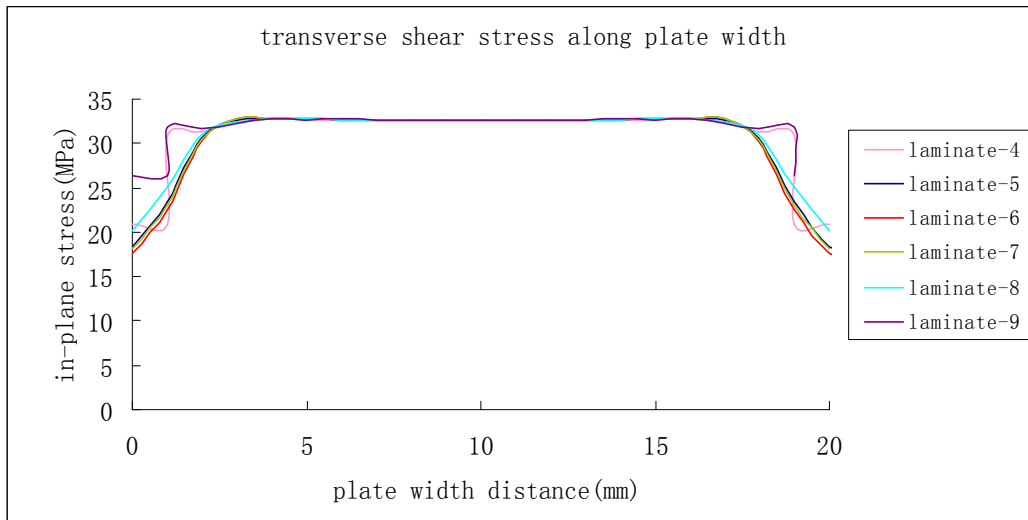


**Figure 3-16 Residual in-plane stress for layer oriented at 0°**

In conclusion, residual transverse shear stress due to thermal expansion only exists at the boundary of the structure and this does not affect the impact



behaviour at the middle of the plate. At the same time, residual in-plane stress in the fibre transverse direction, as can be seen in figure 3-15 and figure 3-16, show no effects from ply clustering. However, the high residual in-plane stress will cause premature matrix crack if the residual stress exceeds the tension strength of the matrix. For composite laminates without premature matrix crack, high residual in-plane stress will cause matrix crack at an early stage of impact which acts as an initiation point for delamination [29].

### 3.4.3 Fibre Bridging Effect

Finally, the effect of fibre bridging on interface delamination was studied. Fibre bridging is defined as the nesting of the fibre, which is observed very often in unidirectional laminates where fibres migrate to each other during the cure time. A diagram of the fibre bridging model is shown in figure 3-17.

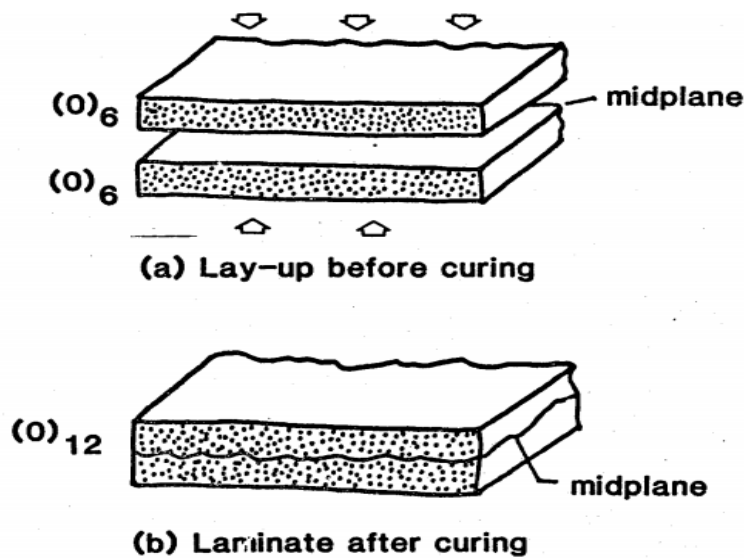


Figure 3-17 Fibre bridging model after curing

At the same time, the bridging of fibres can weaken the interface of fibre and matrix. Fibre bridging happens when fibres are pulled from one side of the delamination plane to the other plane [3].

Figure 3-18 shows Mode I fracture toughness against crack length for four different specimens. The three curves on the top show the DCB model of composite laminate with different angle for the top laminate plate and the

bottom laminate plate. The other curve shows the DCB model with an adhesive bond using the same matrix material as the composite laminate specimens.

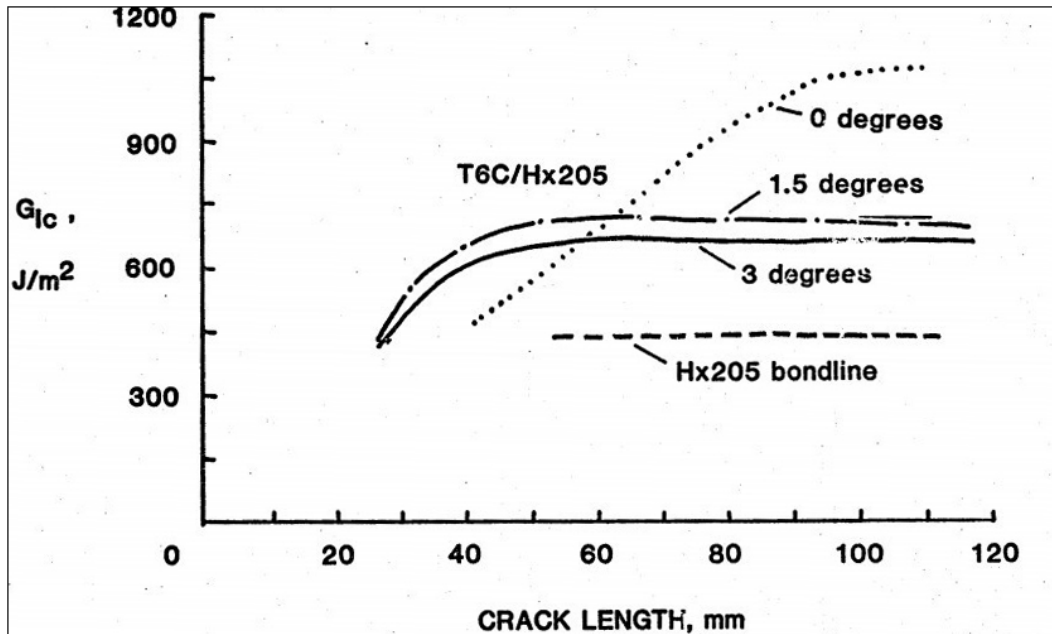


Figure 3-18 Mode I fracture toughness against crack length [3]

The research results shown in figure 3-18 illustrate that the mode I fracture toughness of the matrix material increases rapidly with increasing crack length for both the composite laminate specimens. This is attributed to the fibre bridging effect. For the 0 degree condition, the toughness value may even reach 1000J/m<sup>2</sup> which is almost three times the initial value. In contrast, the fracture toughness of the bond joint specimen showed no sign of increase with increasing crack length. The fracture toughness of the bond joint specimen is almost the same as the initial toughness values of the other three specimens. Based on the discussion above, in situ matrix toughness can be determined either by the toughness value obtained from the bond joint specimen or by the toughness found in the composite specimens before fibre bridging which is widely used in composite structure design.

In conclusion, because of the fibre bridging effect, which is more severe between plies with the same fibre orientation, more fracture energy is required to debond the surface area.

The same phenomenon was observed in the End Notched Flexure test which is used to determine the mode II fracture toughness of the matrix material.

Apart from the three factors discussed above, shear matrix cracks may play a very important role in this phenomenon. Shear matrix cracks only stop at the interface where the adjacent plies have different fibre orientation [70]. Because of this, shear matrix cracks will propagate in the thickness direction for clustering plies. When the shear matrix cracks reach the interface where adjacent plies have different fibre directions, matrix cracks start to propagate in the plane of this interface which acts as an initial point for delamination.

From the investigation of the three factors which affect the interlaminar delamination above, it is clear that the main reason why there is no delamination between plies with the same fibre orientation is the fibre bridging effect and the fact that no matrix crack exists between layers with the same fibre orientation. Bending stiffness mismatch of the ply groups does not necessarily increase the interface shear stress at the adjacent plies. Residual transverse shear stress only happens at the boundary of the composite plate which cannot affect the impact delamination damage in the middle of the plate. Also as there is no fibre in the thickness direction, it cannot cause thermal strain change. At the same time, a clustered layup does not increase the residual in-plane stress if the composite plates have balanced layup. However, relatively high residual in-plane stress causes matrix crack in the early stages of impact which will lead to more delamination.

## **3.5 Damage Initiation**

### **3.5.1 Stress Distribution Study**

Damage initiation refers to the starting of degradation of a material point. Usually when the normal stress and transverse shear stress at the interface satisfy certain damage initiation criteria, the degradation of material begins.

Because of the complexity of stress state in the impact damage process, there is no consensus of opinion about selecting a suitable damage initiation criterion to predict the start of damage [76, 77]. One of the unresolved problems is

clearly that delamination is affected by the compressive peel stress. The research results in [61] found that much less delamination happened at the top interface of the plate where higher compressive peel stress existed.

In order to have a good understanding of the peel stress and transverse shear stress distribution along the plate span, an FE model employing plane strain elements was set up. The composite plate has 12 different layers with the stacking sequence of  $[0_3/90_3]_s$ , the impactor was treated as an analytical rigid body. The size of the model is 67.5 mm×45 mm with thickness of 2.4 mm. The FE model is illustrated in figure 3-19. Reaction load at prescribed displacement 1.88 mm is about 1200 N.

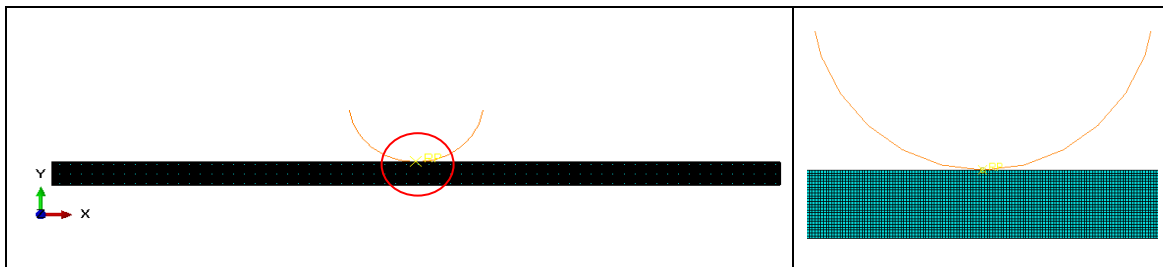


**Figure 3-19 FE model for stress distribution study**

The contour plot and curve plot of peel stress distribution along the plate span are shown in figures 3-20-3-21 respectively.

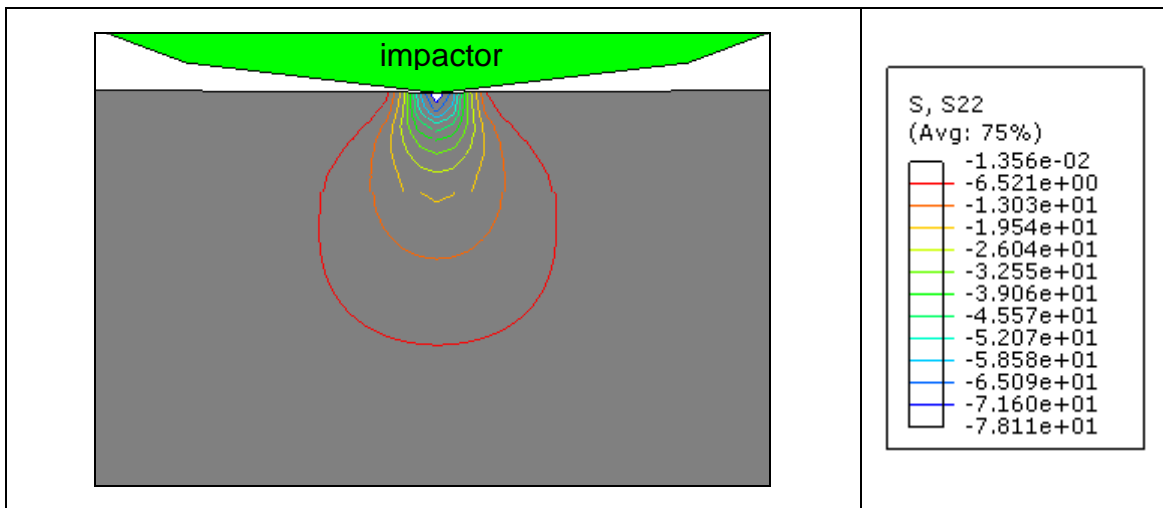


**Figure 3-20 Contours plot of peel stress along the plate span**

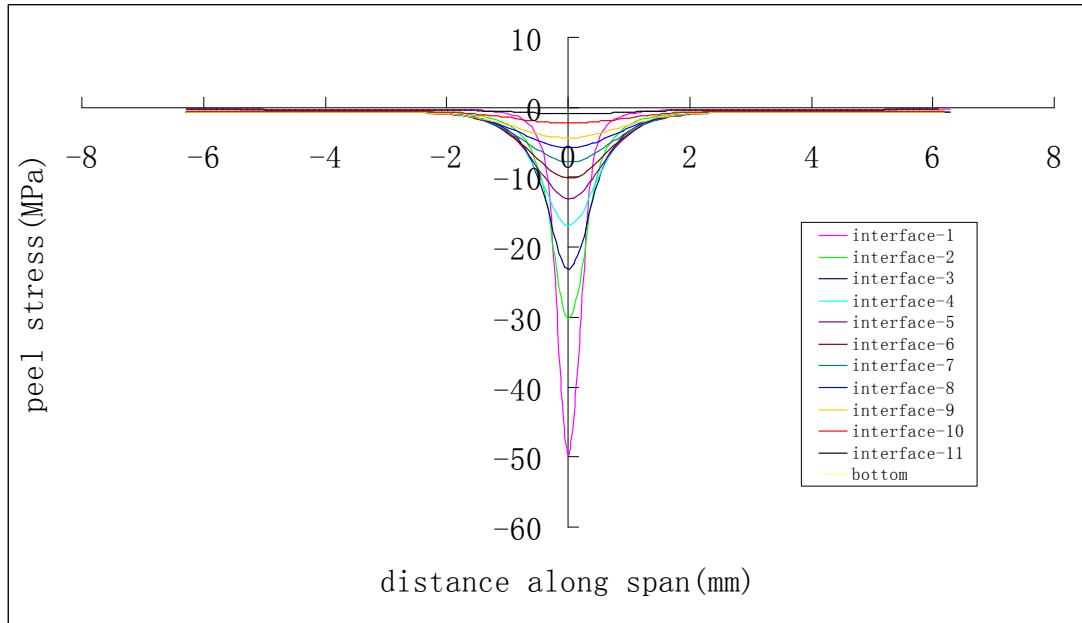


**Figure 3-21 Peel stress distribution along the plate span**

As illustrated in figure 3-20 and figure 3-21, the maximum compressive peel stress happens at the top interface of the plate. The compressive peel stress decreases from the top interface to the bottom interface. The compressive peel stress dominates the area just beneath the impactor which in turn will suppress the delamination.

The contours plot and curve plot of transverse shear stress distribution along the plate span are shown in figure 3-22 and figure 3-23 respectively.

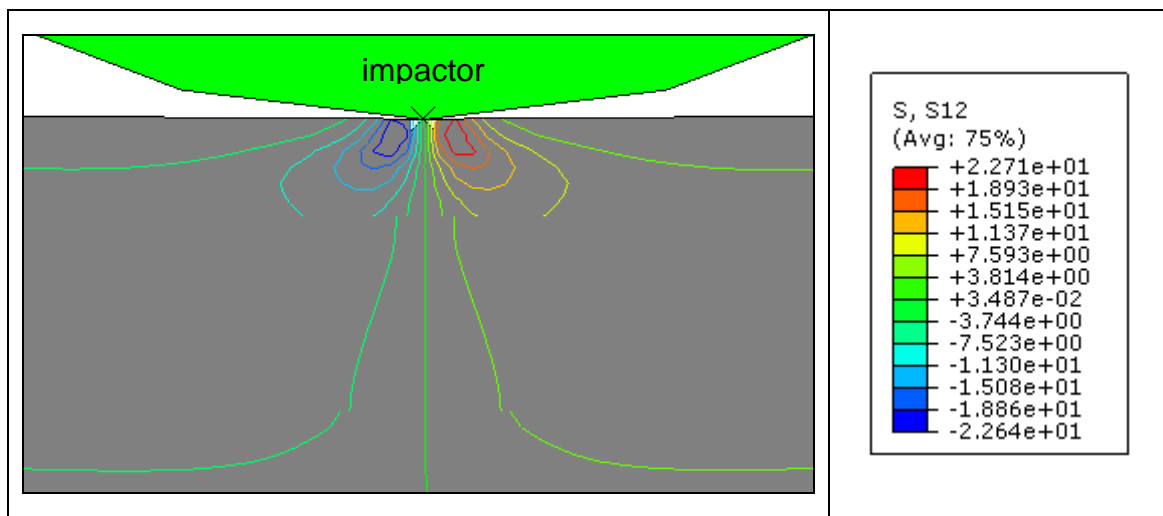


**Figure 3-22 Contours plot of transverse shear stress along the plate span**

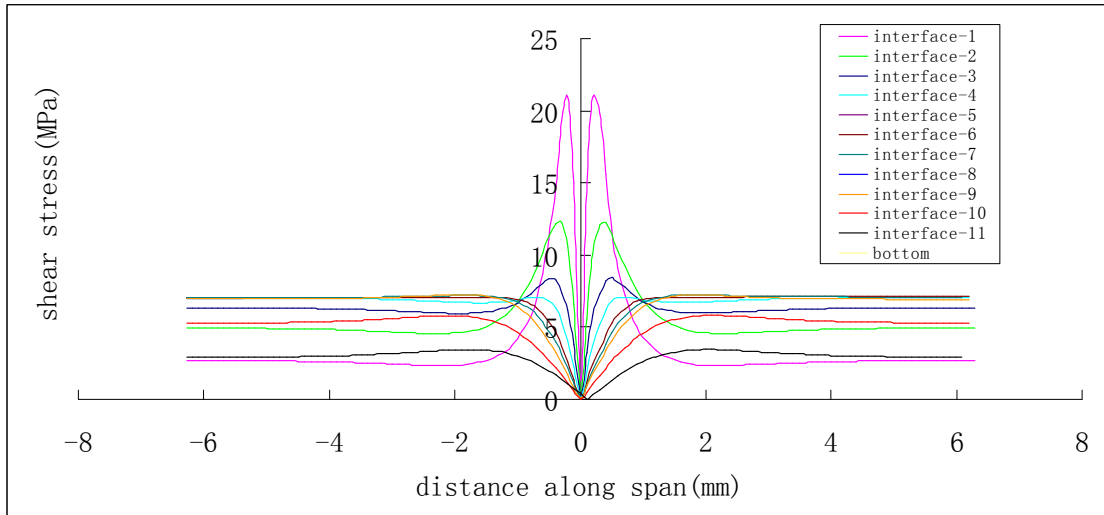


**Figure 3-23 Transverse shear stress distribution along the plate span**

As can be seen in figure 3-22 and figure 3-23, the maximum transverse shear stress also happens at the top interface where larger peel stress exists. This phenomenon was attributed to the change in the larger peel stress at the top interface and only restricted to a small area along plate span. In the area away from the impact the transverse shear stress distribution is according to the classical shear stress distribution where maximum stress happens at the middle plane.

The curve plot of in-plane tension strain distribution in the  $0^\circ$  fibre direction along plate span is shown in figure 3-24.

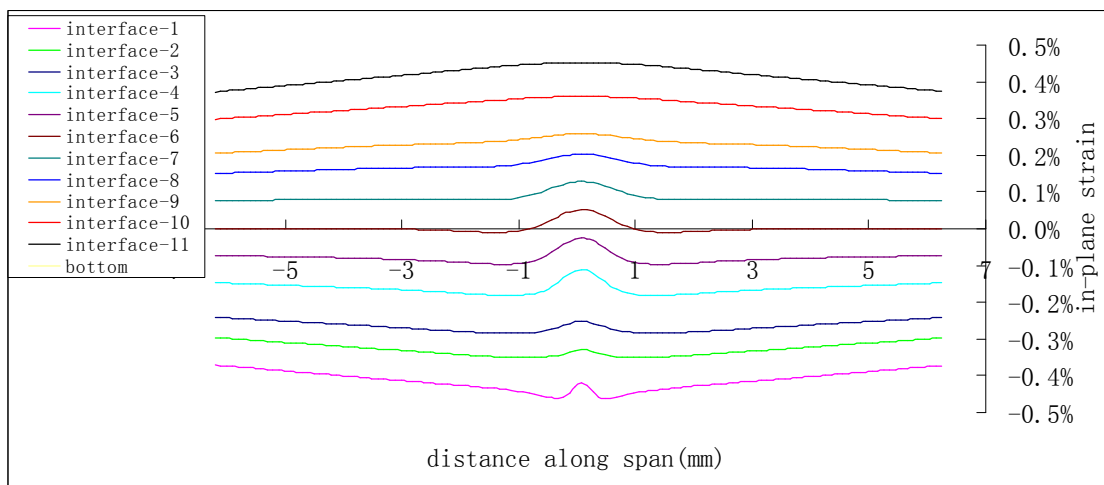


**Figure 3-24 In-plane strain distribution along span**

Because of the discontinuity of in-plane stress, in-plane strain along the  $0^\circ$  fibre direction is shown in figure 3-24. The experimental test observed matrix cracks on the back face which are mainly attributed to the in-plane tension stress and the residual tension stress.

### 3.5.2 Friction Considerations in the Upper Half

Though large compressive peel stress exists at the interfaces, none of the criteria in ABAQUS consider the effect of this compression loading. In order to take account of this effect, in the research work of [61, 62] the new damage initiation criteria based on the work done by [78] was adopted to predict the delamination initiation and good agreement between FE results and experimental data was achieved. The criterion is shown below:

$$\begin{aligned} \left(\frac{t_n}{N}\right)^2 + \left(\frac{t_s}{S}\right)^2 + \left(\frac{t_t}{S}\right)^2 &= 1 \quad \text{for } t_n \geq 0 \\ \left(\frac{t_s}{S}\right)^2 + \left(\frac{t_t}{S}\right)^2 - 8 \cdot \left(\frac{t_n}{N}\right)^2 &= 1 \quad \text{for } -\sqrt{\frac{t_s^2 + t_t^2}{8}} \leq t_n < 0 \\ \text{NO DELAMINATION} &\quad \text{for } t_n < -\sqrt{\frac{t_s^2 + t_t^2}{8}} \end{aligned}$$

Where N and S are the interface strength and  $t_n$ ,  $t_s$ ,  $t_t$  are the interface stress for mode I, II and III respectively.

In this paper, a new method which considers the action of friction at the interface is introduced to resolve the constraining effect of compression through thickness.

The cohesive elements which act as an interface between layers have tension stiffness according to the bilinear traction-separation law. However, under compressive load conditions, the original normal stiffness of the cohesive elements still exists in order to stop penetration between adjacent layers. The normal stiffness is retained even after the total failure of the cohesive elements [61, 62]. In this research, a contact relationship was set up between plies where delamination exists with the aim of including friction between adjacent plies. In these circumstances, there are two spring bodies at the interfaces where

delamination happens, one is cohesive element and the other is a contact pair, under compressive stress loading. The relation between cohesive elements and contact pair is illustrated in figure 3-25.

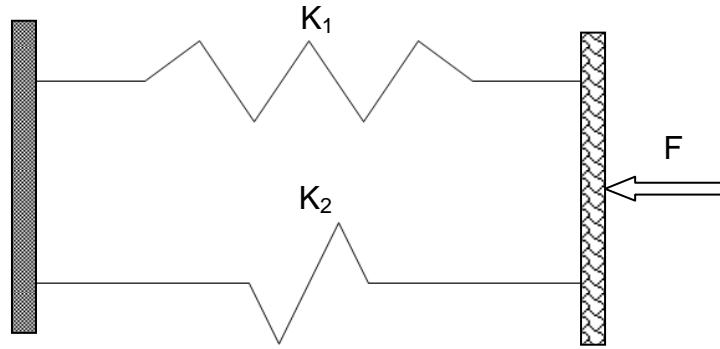


**Figure 3-25 The relation between cohesive elements and contact pair**

Where  $K_1$  and  $K_2$  represent the coefficient of stiffness of cohesive elements and contact pair respectively and  $F$  symbolises compressive load. The displacement of the above condition is calculated below:

$$\delta = \frac{F}{K_1 + K_2}$$

The contact force between the contact pair is calculated as:

$$F_c = \delta \times K_2 = \frac{FK_2}{K_1 + K_2}$$

A typical value of the coefficient of friction 0.9 is used to calculate friction force and a sensitivity analysis of the coefficient of friction is carried out. Friction force is calculated as follows:

$$F_f = \mu \times F_c = \frac{\mu FK_2}{K_1 + K_2}$$

Where  $\mu$  is the coefficient of friction. Considering the friction effect between plies where delamination happens the transverse shear strength for the interface can be calculated as:



$$S_T = S + S_F = S + \frac{\mu FK_2}{A(K_1 + K_2)}$$

Where  $S_T$  is the true shear strength of the interface;  $S_F$  is the friction stress while  $S$  is the cohesive elements transverse shear strength.

The criterion for damage initiation is shown below:

$$\left\{ \frac{\langle t_n \rangle}{N} \right\}^2 + \left\{ \frac{t_s}{S_T} \right\}^2 + \left\{ \frac{t_t}{T_T} \right\}^2 = 1$$

Where  $N$ ,  $S_T$ ,  $T_T=S_T$  are the interface strengths taking friction into account and  $t_n$ ,  $t_s$ ,  $t_t$  are the interface stresses for modes I, II and III respectively. Brackets  $\langle \rangle$  mean that compressive load does not initiate delamination damage.

In order to establish the contact relation between plies where delaminations exist, zero thickness cohesive elements are needed in the FE model.

### 3.5.3 Interaction Between Matrix Crack and Delamination

As can be seen in figure 3-23, the transverse shear stress in the area away from the impactor had a classical parabolic shape distribution which is also illustrated in figure 3-10 and figure 3-11. Another important point is that the shear stress level in these areas away from the impactor is below 10 MPa which cannot be a main factor in the initiation of delamination.

According to the research works [29, 30], the existence of matrix crack affects the initiation of delamination. At the same time Choi [63] clearly stated that delamination only happened with the presence of matrix cracks. When matrix cracks happen, there is high peel stress at the interface along the matrix crack which leads to mode I delamination [29, 30, 64]. The stress distribution in the delaminated interface taking matrix crack into account is studied in chapter 7.

The stress components which induce matrix crack are  $\sigma_{22}$ ,  $\sigma_{13}$  and  $\sigma_{33}$  where 1 is the  $0^\circ$  fibre direction, 2 is the fibre transverse direction and 3 is the thickness direction. However,  $\sigma_{33}$  is relatively small compared with the other two components and it decreases very sharply from the impact point [29].

As shown in figure 2-3, matrix cracks can happen in any position through the thickness of the impacted laminate. However, according to the experimental results of González [8], interface delaminations mainly exist at the lower half of the laminate. Because of this, only matrix cracks at the lower half of the laminate are taken into account in this research. Usually the matrix cracks happen at a certain distance away from the impactor in the fibre transverse direction. But, to simplify the simulation, matrix cracks are only inserted in the symmetry plane under the impact point.

### 3.6 Damage Propagation

The linear interaction criterion which considers the mixed modes of fracture energy is used in this thesis. The criterion is shown below [72] :

$$\left\{ \frac{G_I}{G_{IC}} \right\} + \left\{ \frac{G_{II}}{G_{IIC}} \right\} + \left\{ \frac{G_{III}}{G_{IIIC}} \right\} = 1$$

Where  $G_{IC}$ ,  $G_{IIC}$  and  $G_{IIIC}$  are the critical energy release rates in mode I, II and III respectively.

A damage indicator  $d$  is used to monitor the damage process, the damage indicator ranges in value from 0 to 1. Value 0 means the interface is intact while 1 indicates the total decohesion of the interface.

## 4 DCB MODEL USING COHESIVE ELEMENTS

### 4.1 Introduction

The Double Cantilever Beam (DCB) test is one of the most popular specimen test used to study the mode I fracture toughness of composite laminates [79]. Before using cohesive elements to simulate complicated delamination in a composite laminate, a DCB Finite Element model with cohesive elements located in the middle of the specimen was built first to validate the capability of the cohesive elements to simulate mode I fracture toughness.

### 4.2 Geometry Model Description

The DCB test was set up with specimen geometry and boundary conditions as shown in Figure 4-1.

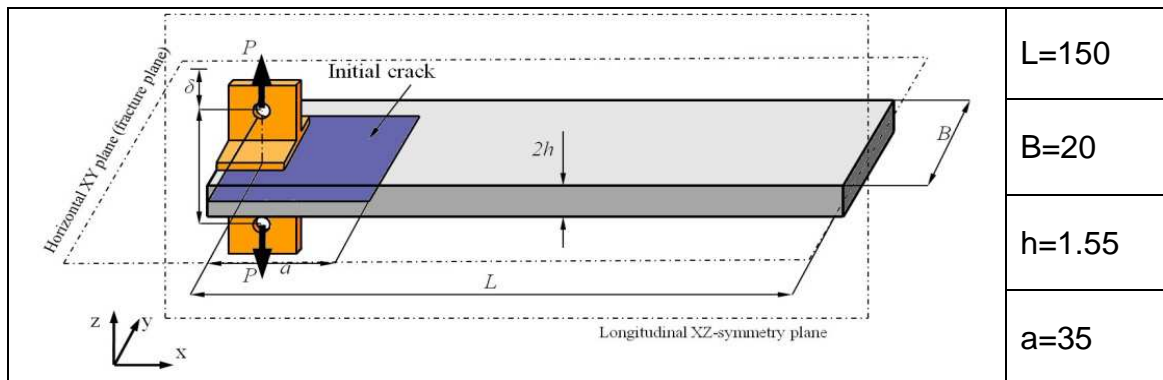


**Figure 4-1 DCB specimen geometry (unit: mm)**

The specimen is manufactured from HTA/6376C carbon/epoxy prepreg which is produced by Ciba Geigy. The ply stacking sequence of the specimen is  $[0^{\circ}_{12} // (\pm 5^{\circ} / 0^{\circ}_4)_s]$  which contains 24 layers of thickness 3.1 mm. The sign “//” means the middle interface plane, i.e. the plane where delamination happens. The ply angle in the bottom half is  $5^{\circ}$  with the aim to avoid fibre bridging effects in the delamination interface [80]. However, the effect on bending stiffness from the non-zero lay-up in the bottom half is small and it is not taken into account in FE analysis. Material properties of lamina and cohesive interface are summarized in Table 4-1.

**Table 4-1 Material properties used in FE analysis [80].**

Lamina								
$E_{11}$ (MPa)	$E_{22}$ (MPa)	$E_{33}$ (MPa)	$\nu_{12}$	$\nu_{23}$	$\nu_{13}$	$G_{12}$ (MPa)	$G_{13}$ (MPa)	$G_{23}$ (MPa)
146000	10500	10500	0.30	0.51	0.30	5250	5250	3480
Interface								
$G_{IC}$ (N/mm)	$k_N$ (N/mm <sup>3</sup> )	$k_S$ (N/mm <sup>3</sup> )	$k_T$ (N/mm <sup>3</sup> )	N (MPa)	S (MPa)	T (MPa)		
0.2386	50000	50000	50000	30	80	80		

In the FE model, Quasi-Static Load (QSI) is used instead of dynamic impact load. The QSI is simulated by using displacement load  $\delta$  which is more stable and easy to inspect [80]. The reaction force  $P$  is also recorded during the analysis.

Experimental data from Asp [81] were used to validate the simulation results.

### 4.3 FE Model Description

Because of symmetry, only one half of the specimen was modelled and studied at first and the cohesive energy used in the analysis is half of the critical SERR. Boundary conditions matching the experimental samples were employed by imposing zero y-direction displacement constraints to the node on the symmetry edge. Element type and size are summarized in Table 4-2 [80].

**Table 4-2 Element type and size used in FE analysis [80]**

Cohesive interface		Lamina			
Element type	Element size	Element type	Free arm	Delamination part	Undamaged part
COH2D4	0.04x0.1mm	CPE4R	0.5x0.1mm	0.2x0.1mm	1x0.2 mm

The finite element model of DCB can be seen in Figure 4-2.

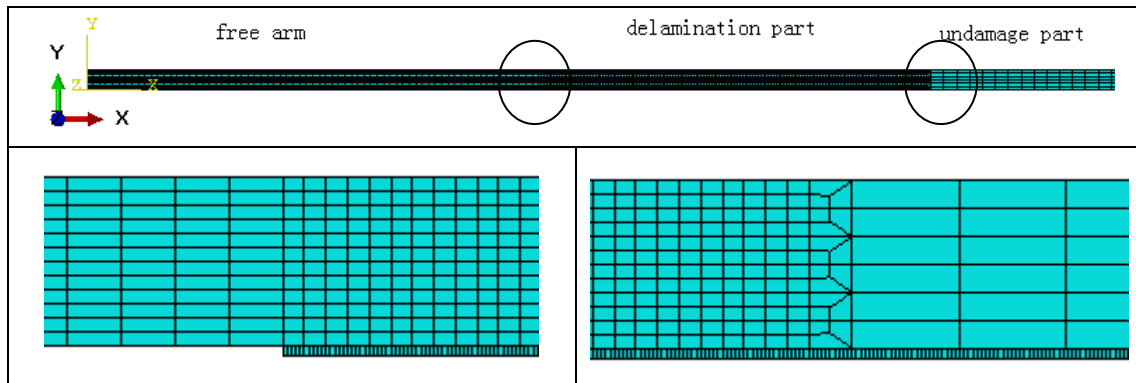


**Figure 4-2 The half finite element model of DCB**

A displacement equation constraint was also used as a constraint to make sure the bottom and top nodes of the cohesive element have the same x-direction displacement.

#### **4.4 FE Results and Validation**

The shear stress along the cohesive interface at the prescribed displacement of 3 mm is illustrated in Figure 4-3. In this research crack is reached when the stiffness of the cohesive elements become zero which means the cohesive elements have been positively damaged.

In the DCB configuration peel stress is the only stress component which leads to delamination. At the same time, the shear stress is theoretically supposed to be zero at the interface. But, as can be seen in Figure 4-3, near the crack tip shear stress is more than 6 MPa which is not negligible. In this half model, the deformation of the cohesive elements in the Y direction is not symmetric which will cause unexpected shear stress. Therefore, the whole DCB FE model was introduced to eliminate this problem. All the results presented later are derived using the whole model. The whole DCB model is shown in Figure 4-4.

A plot of reaction force at the free DCB arm versus the prescribed displacement is shown in Figure 4-5. The reaction force exhibits linear behaviour before the crack begins to open. When the crack happens, the reaction force decreases with displacement. The FE results and the experimental data in Figure 4-5 show good agreement.

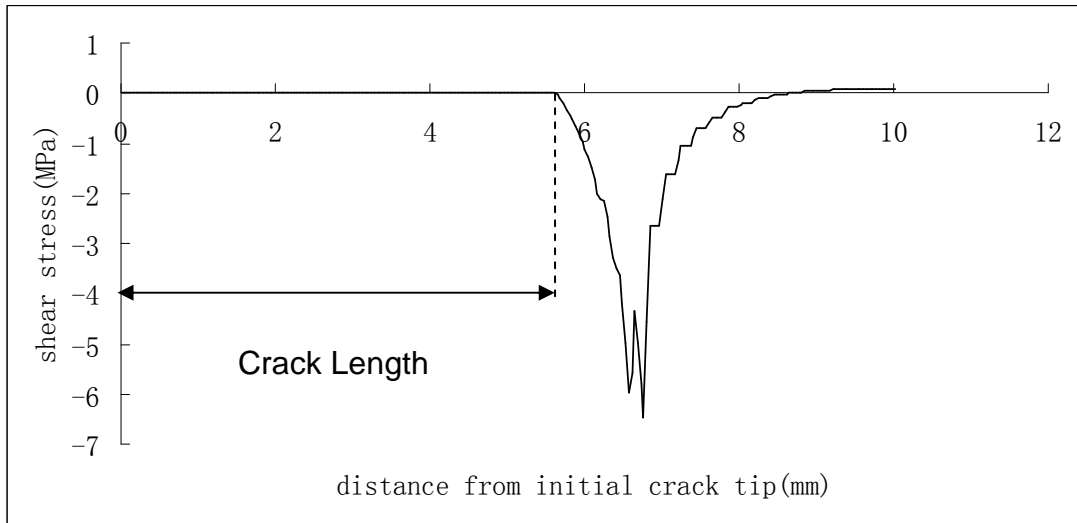


**Figure 4-3 Shear stress distributions along the interface**

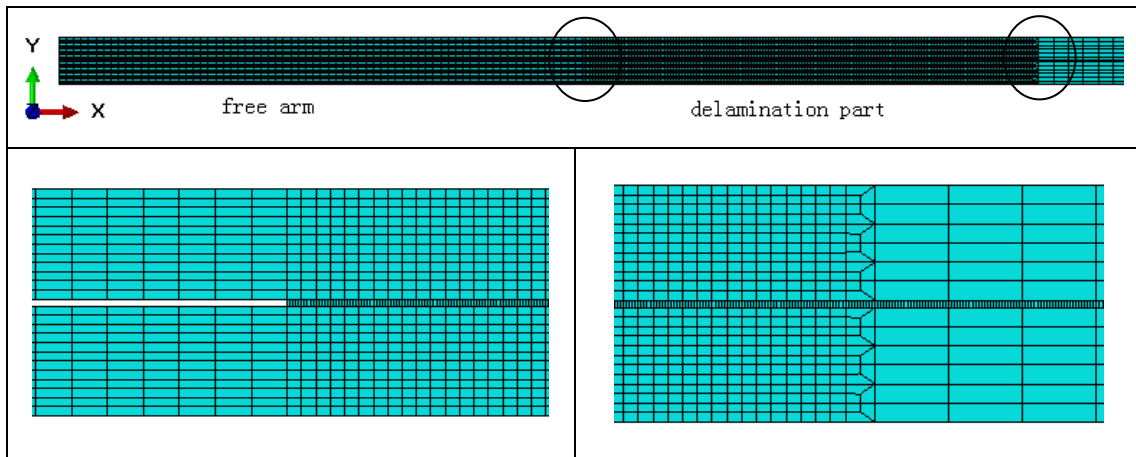


**Figure 4-4 The whole finite element model of DCB**

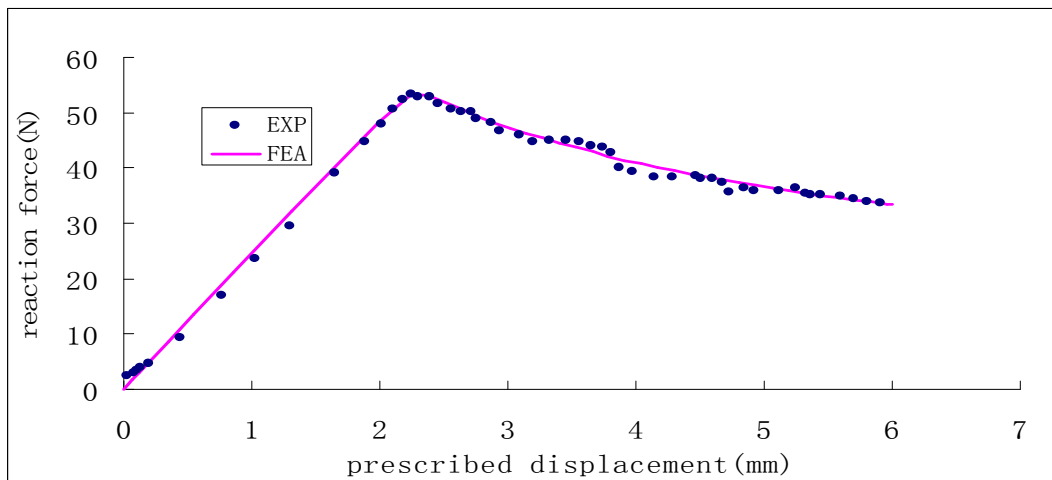


**Figure 4-5 Relations between reaction force and displacement**

Figure 4-6 to 4-8 show contour plots of the three stress components in the cohesive interface and lamina on both sides, near the crack tip at prescribed displacement which is 3 mm.

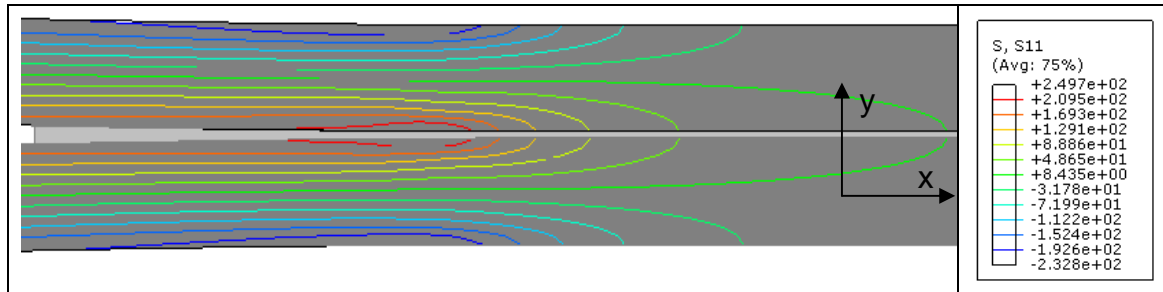


**Figure 4-6 X-direction normal stress distributions (unit: MPa)**

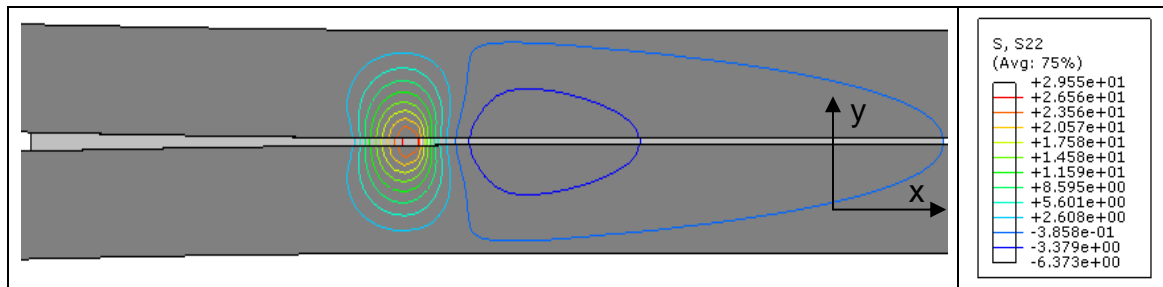


**Figure 4-7 Y-direction peel stress distributions (unit: MPa)**

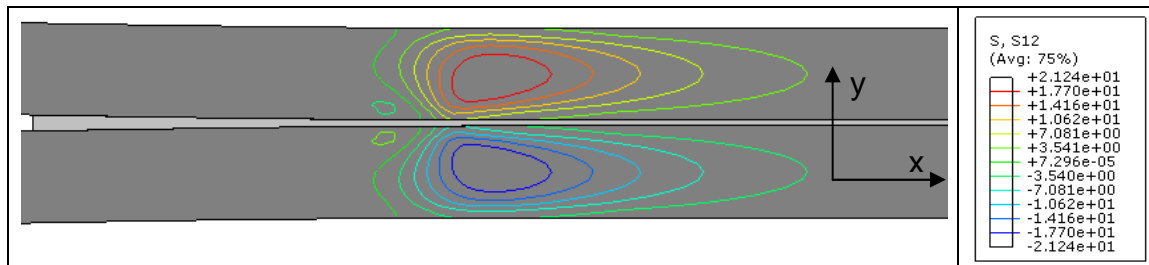
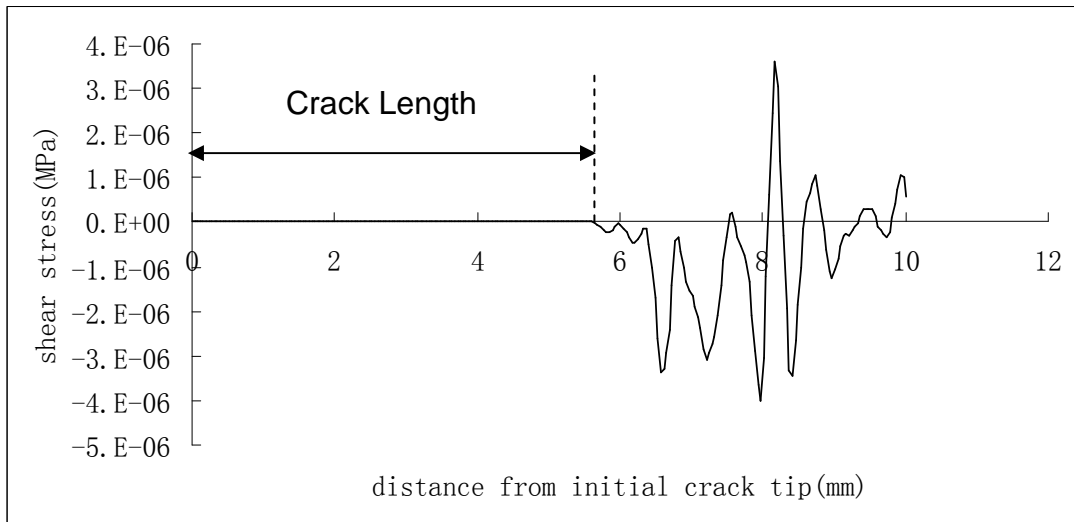


**Figure 4-8 Transverse shear stress distributions (unit: MPa)**

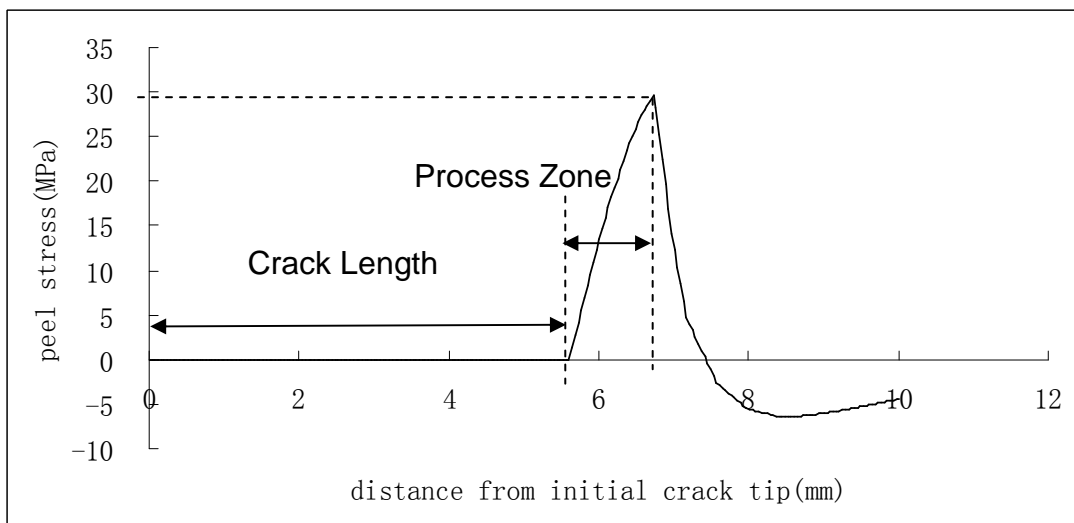
As can be seen in figure 4-7, the normal stress of the cohesive interface in the y direction is about 30 MPa which is the same as the peel strength of the cohesive elements. The transverse shear stress of the cohesive interface is about zero according to the figure 4-8. So it is clear that the interface decohesion in the DCB model is mainly attributable to the peel stress.

Figure 4-9 illustrates the shear stress distribution in the cohesive interface. Figure 4-10 shows the peel stress distribution in the cohesive interface. As can be seen in figure 4-9, the shear stresses along the interface between laminae are very small and can be considered to be zero. Whilst in figure 4-10, the peel

stress increases from zero at the crack tip to almost 30 MPa which is the cohesive peel strength defined in the material property. The area from crack tip (zero stress) to the maximum stress is the process zone where the cohesive elements are in a linear softening stage which means decohesion of these interfaces happens after the onset of the damage.



**Figure 4-9 Shear stress distributions along the interface**



**Figure 4-10 Peel stress distribution along the interface**

#### 4.5 Sensitivity of Cohesive Element Parameters

In order to investigate the impact of the initial stiffness, interface strength and the critical Strain Energy Release Rate (SERR) of the cohesive elements, a

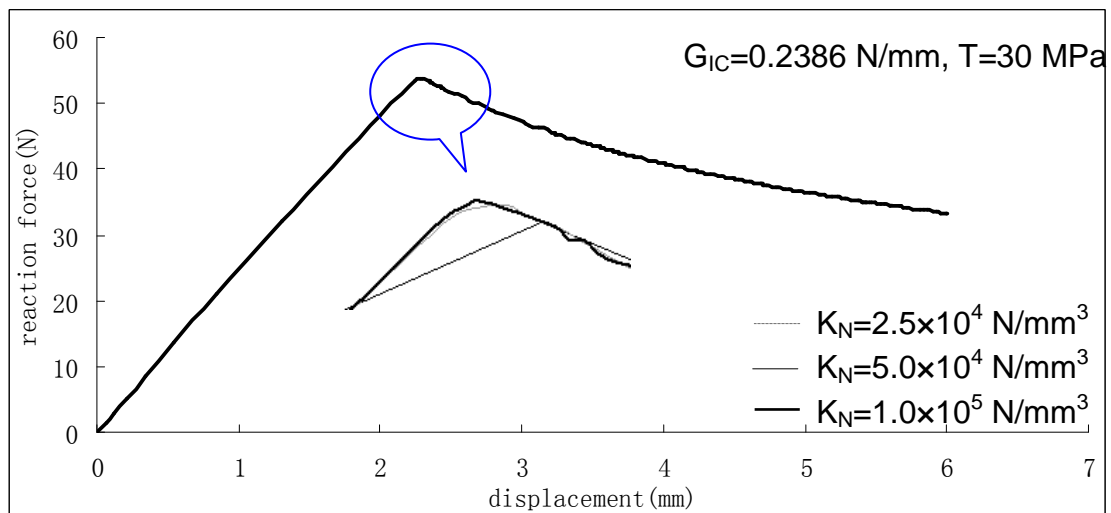


parameter sensitivity study was conducted. Three different values of initial stiffness, cohesive strength and critical SERR, as listed in table 4-3, were used in FE models. In each analysis, only one of the three parameters was changed while the other two parameters were kept constant. Table 4-3 list all the parameters used in the FE analysis.

**Table 4-3 Cohesive element parameters used in sensitive analysis**

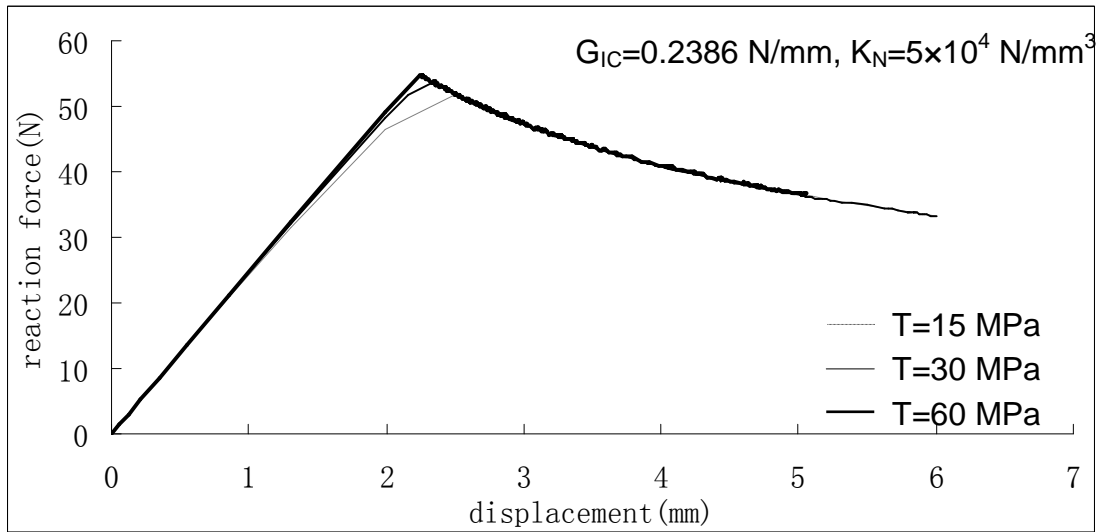
	$K_N$ (N/mm <sup>3</sup> )	T (MPa)	$G_{IC}$ (N/mm)
Lower bound	$2.5 \times 10^4$	15	0.2147
Used in analysis	$5 \times 10^4$	30	0.2386
Upper bound	$10^5$	60	0.2624

Force-displacement curves in Figure 4-11 obtained with different initial stiffness illustrate that the response of the laminate is not sensitive to the value of the stiffness of the cohesive elements. A previous study [80] found the same results.



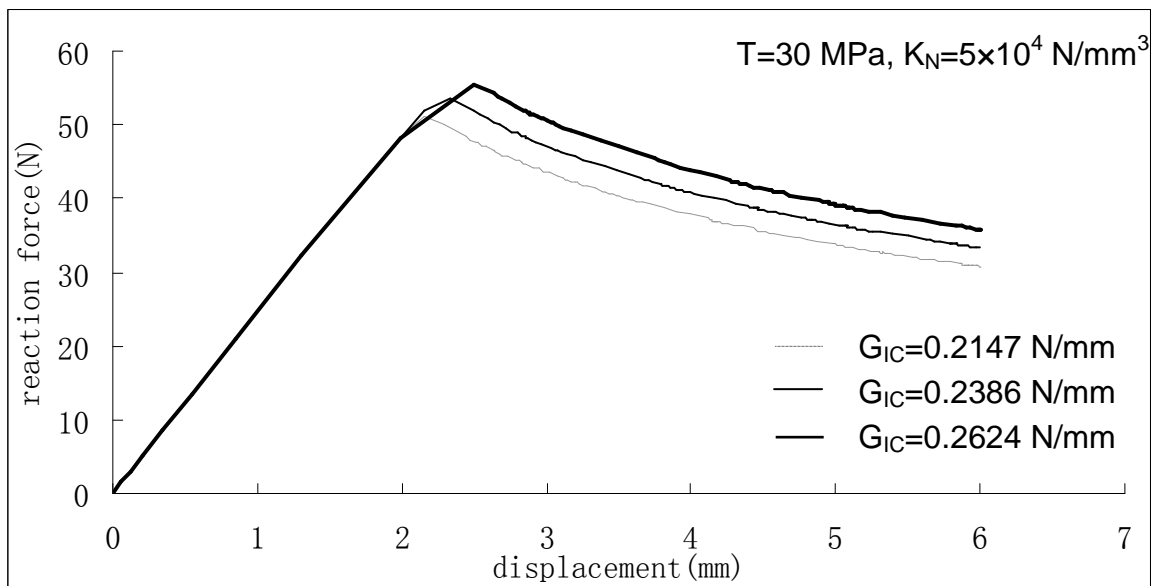
**Figure 4-11 Reaction load versus displacement with different initial stiffness**

Figure 4-12 illustrate the impact of the interface strength on the impact reaction of the composite laminates. As can be seen in figure 4-12, both the peak load and the stiffness of the laminate are very sensitive to the interface strength.



**Figure 4-12 Reaction load versus displacement with different interface strength**

The responses of the laminate with different critical SERR values can be seen in Figure 4-13, which shows that a higher applied force is needed to delaminate the laminate when the critical SERR is higher.



**Figure 4-13 Reaction load versus displacement with different critical SERR**

## 5 ENF MODEL USING COHESIVE ELEMENTS

### 5.1 Introduction

The End Notched Flexure (ENF) test is widely used to study the mode-II delamination fracture of fibre reinforced plastic (FRP) plates [79]. Prior to using cohesive elements to simulate complex delamination in composite laminates, an ENF Finite Element (FE) model with cohesive elements located in the middle of the specimen was built. The aim was to validate the capability of the cohesive elements to simulate mode-II fracture toughness.

Shear load is introduced using the conventional three-point bending configuration. The bending stiffness of each half of the specimen is the same which ensures that only the shear stress loaded on the cohesive elements which are located in the middle of the laminate.

### 5.2 Geometry Model Description

The ENF test was set up with specimen geometry and boundary conditions as shown in Figure 5-1 [80].

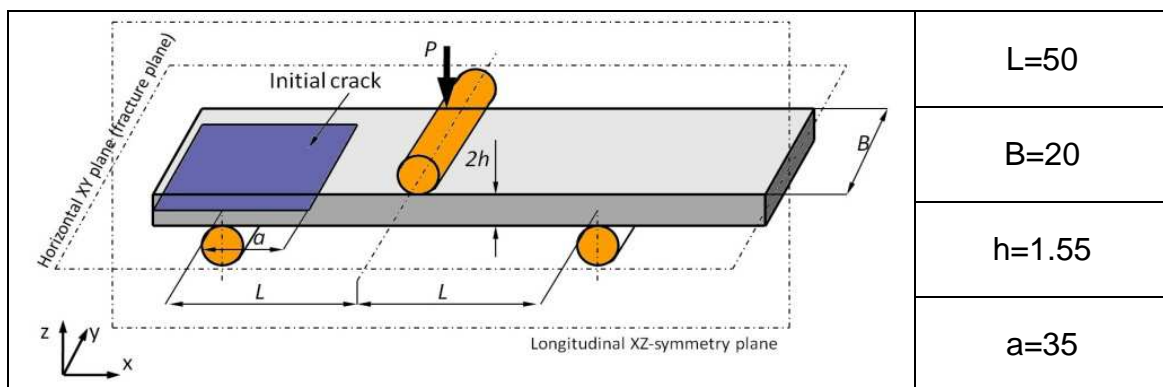


**Figure 5-1 ENF specimen geometry (unit: mm)**

The specimen is manufactured from HTA/6376C carbon/epoxy prepreg which is produced by Ciba Geigy. The stacking sequence of the specimen is  $[0^0_{12} // (\pm 5^0 / 0^0_4) s]$  which includes 24 layers of thickness 3.1 mm, and the sign “//” means the middle interface plane where delamination take place. The ply angle in the bottom half is  $5^0$  with the aim to eliminate fibre bridging effects [80]. However, this change in angle for the bottom half has little effect on the stiffness of the

laminate plate which is not taken into account in FE analysis. Material properties of both lamina and interface are summarized in Table 5-1.

**Table 5-1 Material mechanical properties used in FE analysis [80]**

lamina								
$E_{11}$ (MPa)	$E_{22}$ (MPa)	$E_{33}$ (MPa)	$\nu_{12}$	$\nu_{23}$	$\nu_{13}$	$G_{12}$ (MPa)	$G_{13}$ (MPa)	$G_{23}$ (MPa)
146000	10500	10500	0.30	0.51	0.30	5250	5250	3480
interface								
$G_{IIC}$ (N/mm)	$k_N$ (N/mm <sup>3</sup> )	$k_S$ (N/mm <sup>3</sup> )	$k_T$ (N/mm <sup>3</sup> )	N (MPa)	S (MPa)	T (MPa)		
0.8831	50000	50000	50000	30	90	90		

In the FE model, Quasi-Static Load (QSI) is used instead of dynamic impact load. The QSI is simulated by using displacement load  $\delta$  which is more stable and easy to inspect [80]. The reaction force  $P$  is also recorded during the analysis.

Experimental data from Asp [81] were used to validate the simulation results.

### 5.3 FE Model Description

2D plane strain elements were used to model the ENF specimen. Boundary conditions matching the experimental specimens were applied by imposing zero y-direction translational constraints to nodes at each end and zero x-direction displacement constraints to either end to make sure there is no rigid movement in x direction.

The thickness of the cohesive elements is 0.01 mm which is very small compared with the thickness of the samples. The negligible thickness of the cohesive elements guarantees that the bending stiffness of the FE model matches the experimental samples. Element type and size are summarized in Table 5-2 [80].

**Table 5-2 Element type and size used in FE analysis [80]**

Cohesive interface		Lamina	
Element type	Element size	Element type	Free arm
COH2D4	0.05 mm	CPE8R	0.25x0.1 mm

In order to avoid numerical issues with the using of linear plane strain elements CPE4R [80], quadratic plane strain elements CPE8R were used in this research.

## **5.4 FE Results and Validation**

A plot of reaction force versus prescribed displacement in the delaminated interface is shown in Figure 5-2. The reaction force shows good linear behaviour before the crack begins to open. After the crack happens, the reaction force decreases with displacement.

As illustrated in figure 5-2, the stiffness of the force against displacement curve of FE analysis is a little different from the experimental results at the beginning of the impact event. This phenomenon is mainly due to the existence of a resin rich pocket at the initial crack front. The resin rich pocket is caused by a thick film which is used to produce the 35 mm length artificial crack. Because of the resin rich pocket, the initial artificial crack seems a little bite longer than the given dimension. At the same time, the stiffness of the specimen is very sensitive to the length of the initial crack. In the FE model, the given initial length 35 mm was used without the consideration of the resin rich pocket. Therefore, the initial stiffness and maximum peak load of the FE analysis are slightly different from the experimental results. The same situation was also observed in Bianchi's work [80].

The relationship between reaction force and applied displacement of experimental test, as can shown in figure 5-2, shows that the specimen failed when the prescribed displacement was approximately 3 mm. This is mainly attributed to the high axial stresses coming from bending. However, this specific failure mode is not considered in the FE model and for this reason the FE model illustrates further load capabilities.

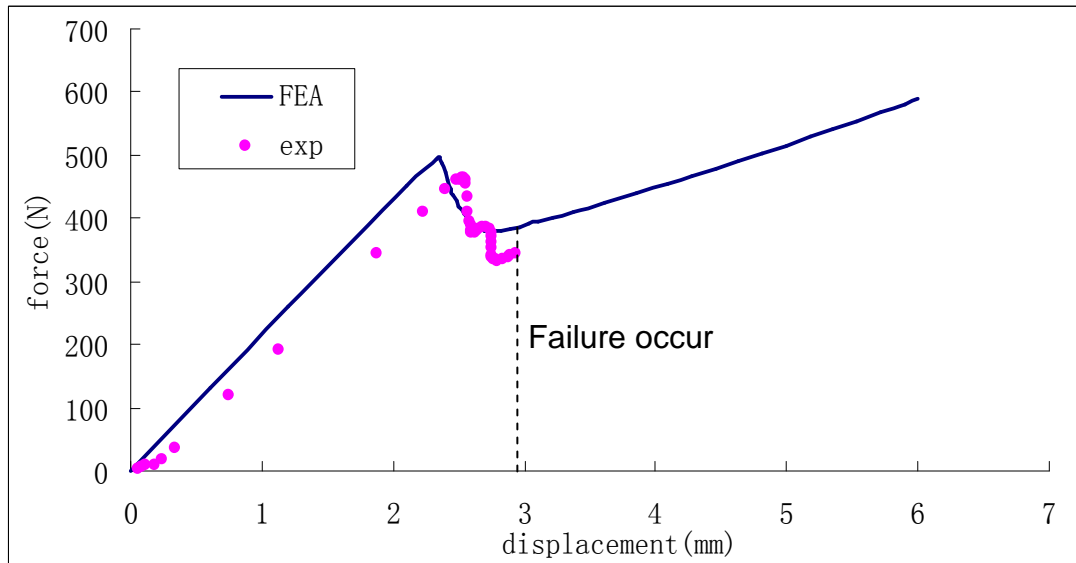


**Figure 5-2 Relations between reaction force and displacement**

Figure 5-3 to 5-5 show contour plots of the three stress components in the cohesive interface and lamina on both sides, near the crack tip at the prescribed displacement which is 2.5 mm.

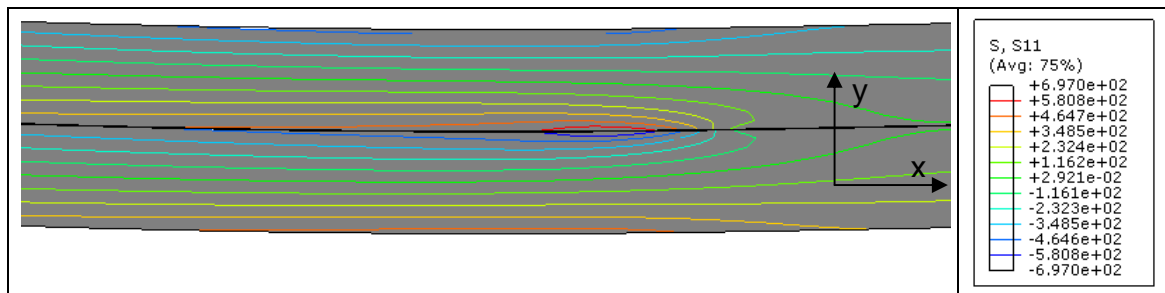


**Figure 5-3 X-direction normal stress distributions (unit: MPa)**

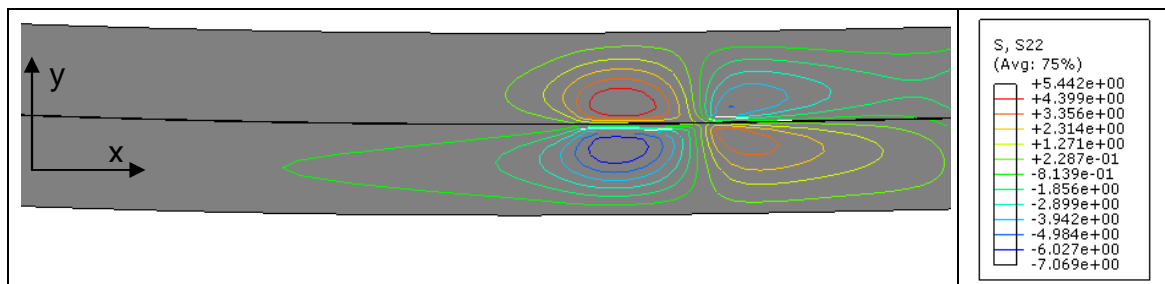


**Figure 5-4 Y-direction peel stress distributions (unit: MPa)**

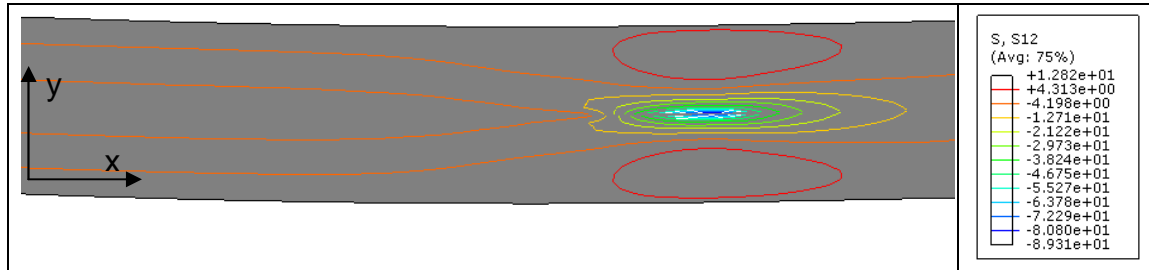


**Figure 5-5 Transverse shear stress distributions (unit: MPa)**

As shown in figure 5-4, the peel stress of the interface is about zero which is reasonable according to the set up of the specimen. Whilst the transverse shear stress of the interface is about 90 MPa which is the same as the cohesive interface shear strength. So it is clear that the interface decohesion of ENF model is mainly attributable to the transverse shear stress.

Figure 5-3 illustrates the normal stress distribution along the interface at a prescribed displacement of 2.5 mm. Figure 5-4 shows the shear stress distribution from the initial crack tip at a prescribed displacement of 2.5 mm. The normal stress after the crack tip which reaches peak stress at 15 mm distance from the initial crack tip mainly comes from the concentrated displacement load acting at the middle of the specimen. Though there is no normal stress at the crack extension area, the original value of the normal stiffness is restored under compressive loads with the aim to prevent material interpenetration at a delaminated interface [61, 62]. The shear stress increases from zero at the crack tip to almost 90 MPa which is the cohesive shear strength defined in the material property. The area from crack tip (zero stress) to the maximum stress is the process zone where the cohesive elements are in a linear softening stage which means that delamination of this interface happens after the initiated damage.

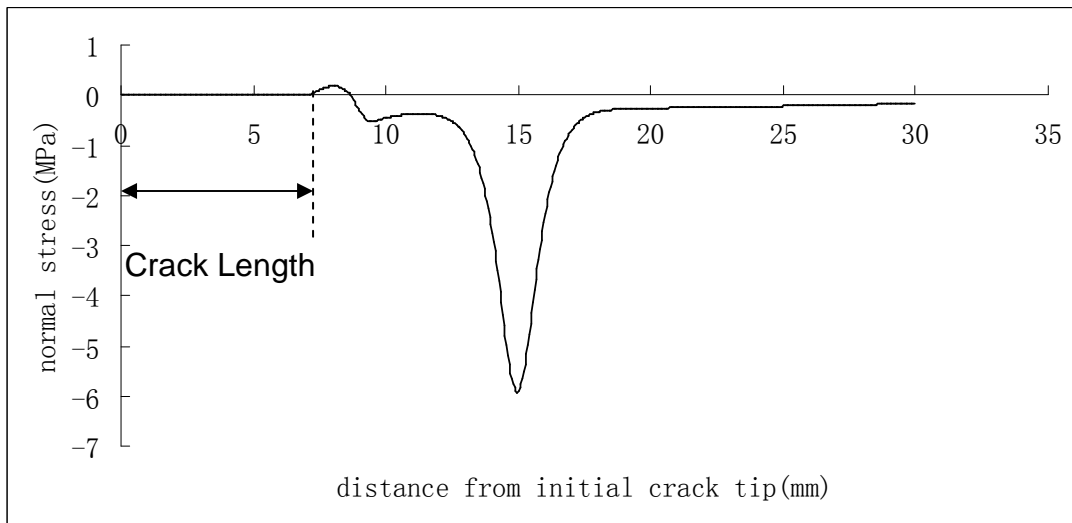


**Figure 5-6 Shear stress distributions along the interface**

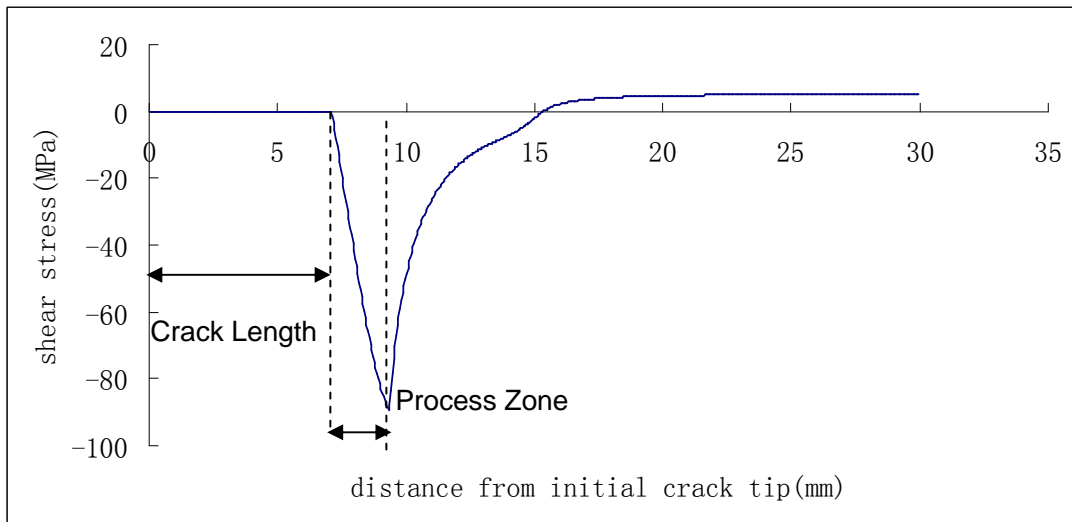


**Figure 5-7 Peel stress distribution along the interface**

### 5.5 Sensitivity of Cohesive Element Parameters

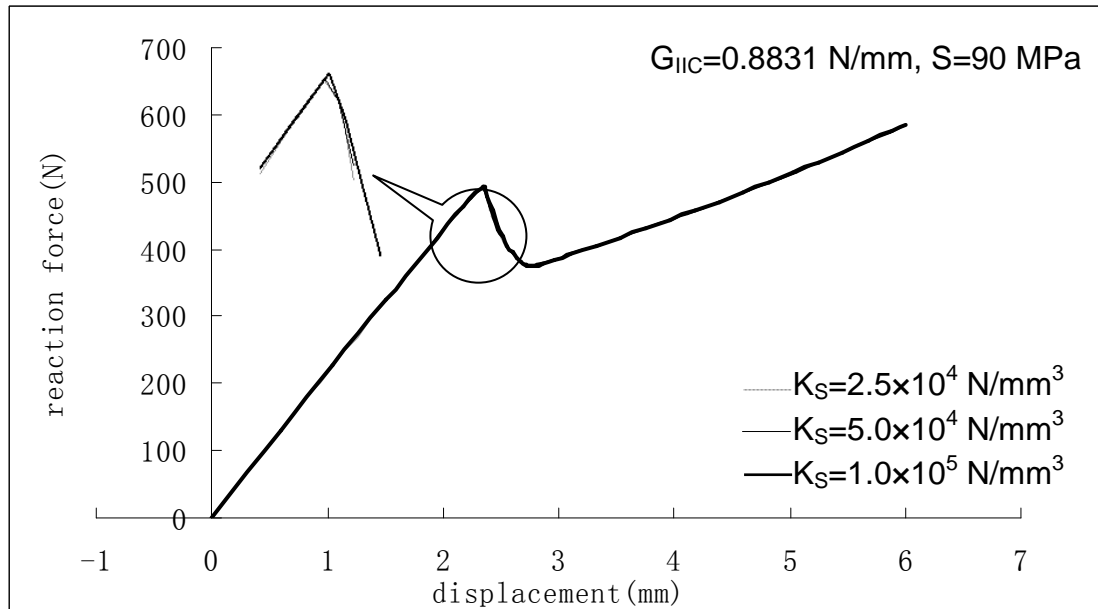
In order to study the effect of the initial stiffness, interface strength and the critical SERR of the cohesive elements, a sensitivity analysis was conducted. Three different values of initial stiffness, cohesive strength and critical SERR, as listed in table 5-3, were used in FE models. In each analysis, only one of the three parameters was changed while the other two parameters were kept constant. Table 5-3 lists all the parameters used in the FE analysis.



**Table 5-3 Cohesive element parameters used in sensitive analysis**

	$K_S$ (N/mm <sup>3</sup> )	S (MPa)	$G_{IIC}$ (N/mm)
Lower value	$2.5 \times 10^4$	45	0.7656
Analysis value	$5 \times 10^4$	90	0.8831
Upper value	$10^5$	130	1.0006

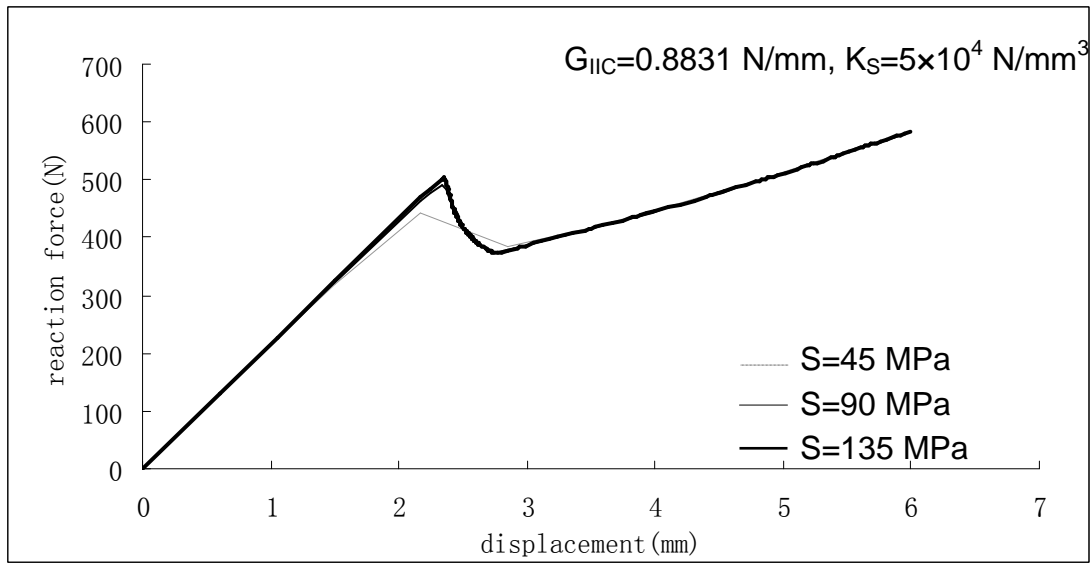
Figure 5-8 shows the force-displacement curves which are obtained using different values of the initial stiffness. As can be seen in figure 5-8, the response of the laminate is not sensitive to the value of the stiffness of the cohesive elements. A previous study [80] had the same outcome.



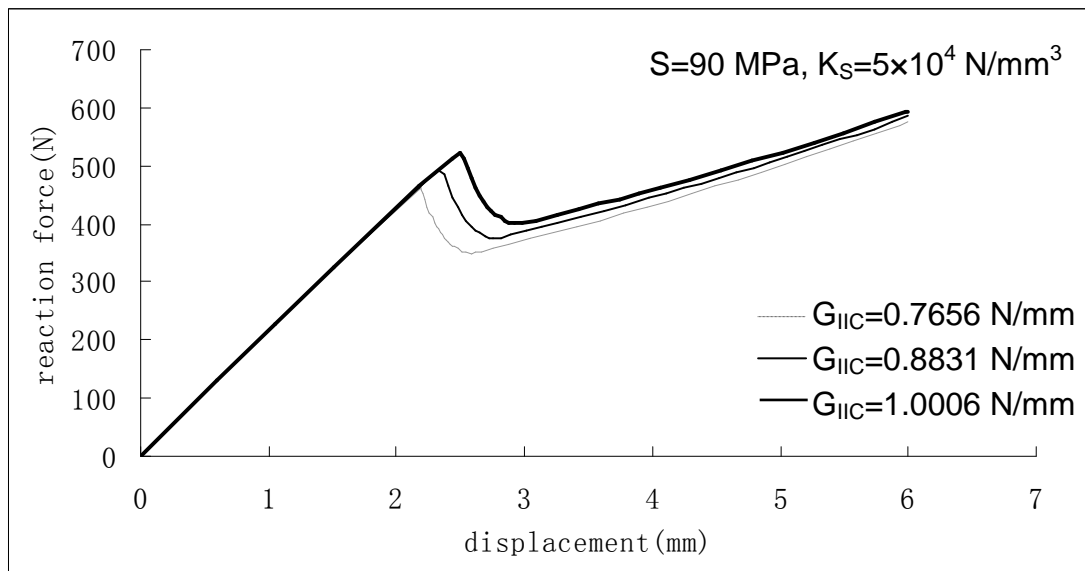
**Figure 5-8 Reaction load versus displacement with different initial stiffness**

Figure 5-9 shows the effect of the interface strength on the response of the laminate. As can be seen in figure 5-9, both the peak load and the stiffness of the laminate are very sensitive to the interface strength.

The response of the laminate with different critical SERR values can be seen in Figure 5-10, which shows that a higher applied force is needed to delaminate the laminate when the critical SERR is higher.



**Figure 5-9 Reaction load versus displacement with different interface strength**



**Figure 5-10 Reaction load versus displacement with different critical SERR**

## 6 IMPACT LOAD SIMULATION OF LOW-VELOCITY IMPACT

### 6.1 Introduction

Both the QSL (Quasi-Static Load) test and dynamic load test were conducted by Brindle [14]. Boeing standard coupons were manufactured using Cytec 977-3/IM7. Figure 6-1 illustrates the comparison of contact force against applied displacement in both dynamic load test and Quasi-Static Load test. In this chapter, an FE model under QSL without considering delamination, fibre and matrix damage was built to simulate the linear contact force before the sharp drop in the QSL test.

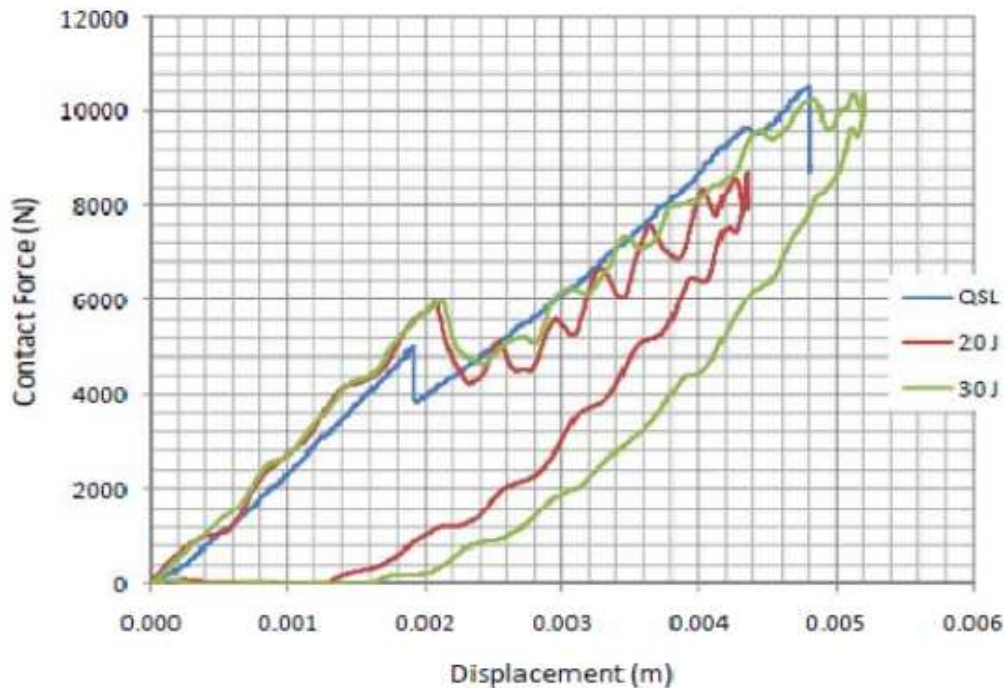


**Figure 6-1 Comparison of static and impact load versus displacement curves [14]**

The set up of the QSL test is shown in Figure 6-2. The impactor was fixed and mounted on to the load machine. A coupon with the size of 100 mm × 150 mm was put on a steel frame and clamped at four points on its surface. The steel frame had a 75 mm × 125 mm rectangular cutout below the coupon. A displacement load which is stable was used in the FE model instead of dynamic load.

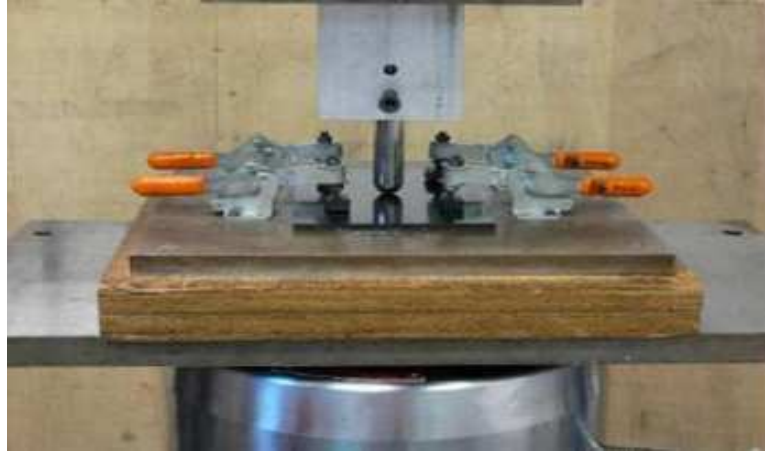


**Figure 6-2 Quasi-static load test set up [14]**

## 6.2 Material Properties

The laminate material is Cytec HYE 977-3/IM7. The stacking sequence of the laminate plate is  $[-45/0/45/90]_{4S}$  which is a quasi isotropic plate. The thickness of the laminate plate is 4 mm which contained 32 plies. The thickness of a single ply is 0.125 mm. table 6-1 lists all the material properties of the laminate plate used in FE analysis.

**Table 6-1 The material properties of the laminate**

Longitudinal Tensile Modulus ( $E_{11}$ ) (GPa)	162
Transverse Tensile Modulus ( $E_{22}$ ) (GPa)	8.34
In-Plane Shear Modulus ( $G_{12}$ ) (GPa)	4.96
Transverse Shear Modulus ( $G_{13}$ ) (GPa)	4.96
Transverse Shear Modulus ( $G_{23}$ ) (GPa)	3.96
Poisson's Ratio ( $\nu_{12}$ )	0.27

## 6.3 FE Model Description

Both conventional shell (2D) and continuum shell (3D) elements were used to model the composite plate without consideration of interface delamination. A 2D FE model using elements of type S4R can be seen in Figure 6-3. A 3D FE model using elements of type SC8R is shown in Figure 6-4. The impactor was modelled using the analytical rigid method.

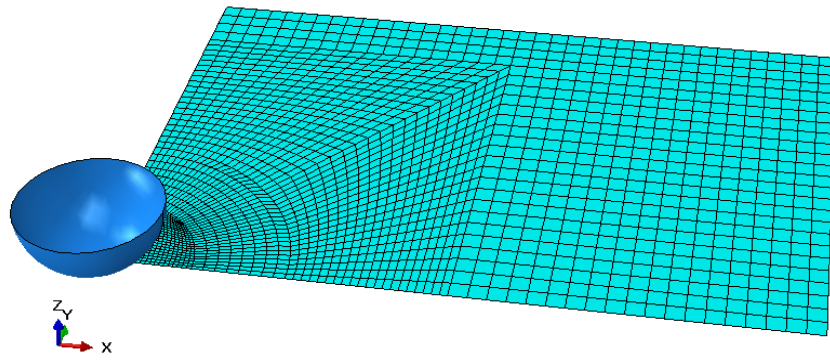


**Figure 6-3 The FEM model using conventional shell elements of QSL test**

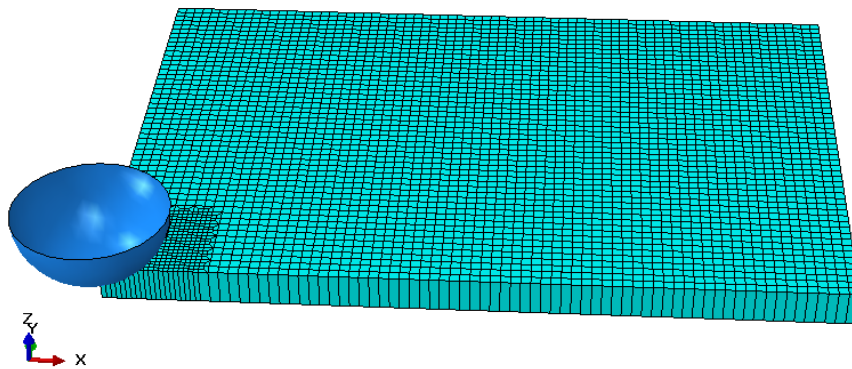


**Figure 6-4 The 3D FEM model using continuum shell elements of QSL test**

To verify the stacking sequence  $[-45/0/45/90]_{4S}$  of the laminate and direction of the single ply, a query function can be selected in ABAQUS and the ply stack plot is illustrated in Figure 6-5.

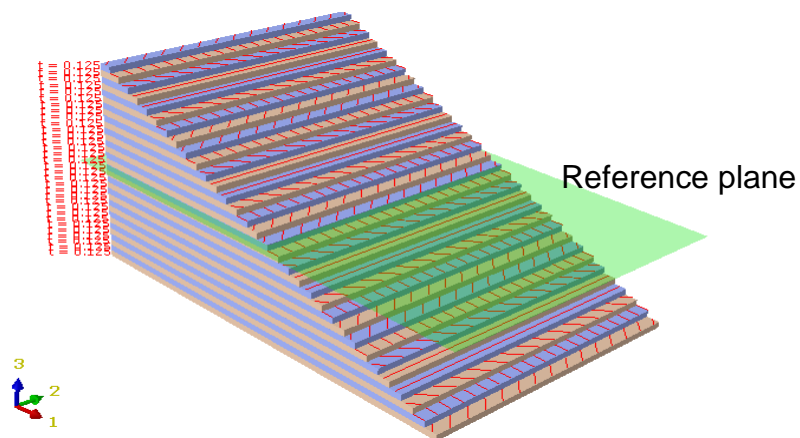


**Figure 6-5 The stacking sequence of the laminate  $[-45/0/45/90]_{4S}$**

## 6.4 Boundary Condition

As can be seen from the configuration of the QSL test in Figure 6-2 and following Ning's research result [81], simply supported boundary conditions for both 2D and 3D models were used in this research. To reduce the computing time only a quarter of the composite plate was modelled because of the symmetry of the test specimen which is shown in Figure 6-6.

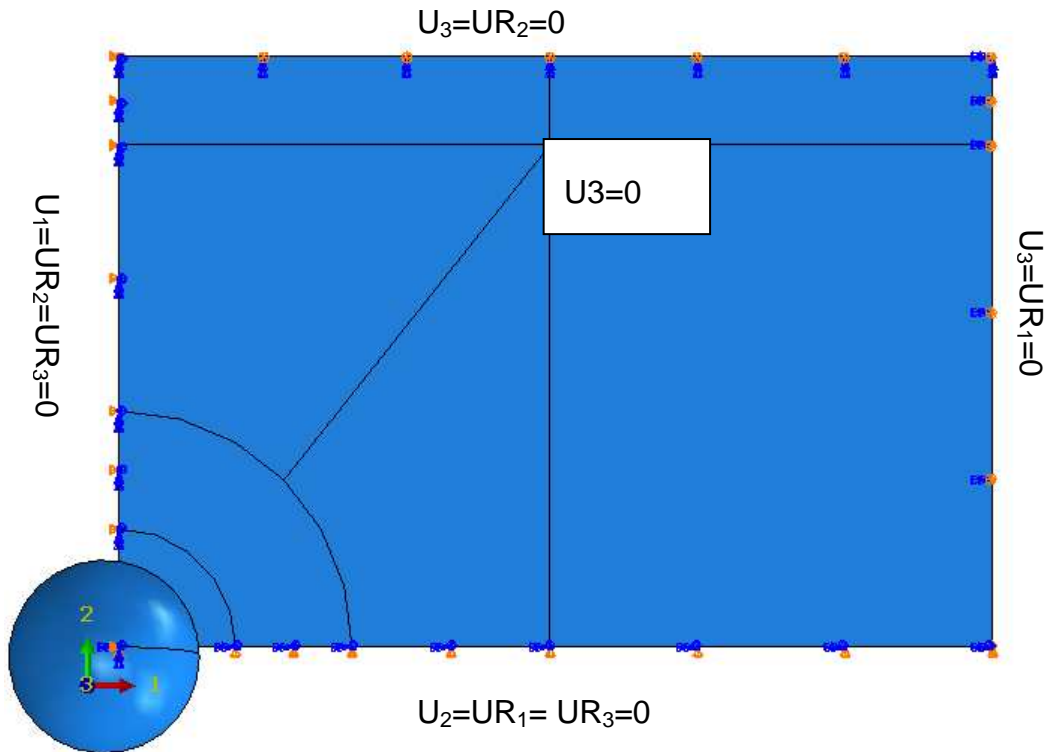
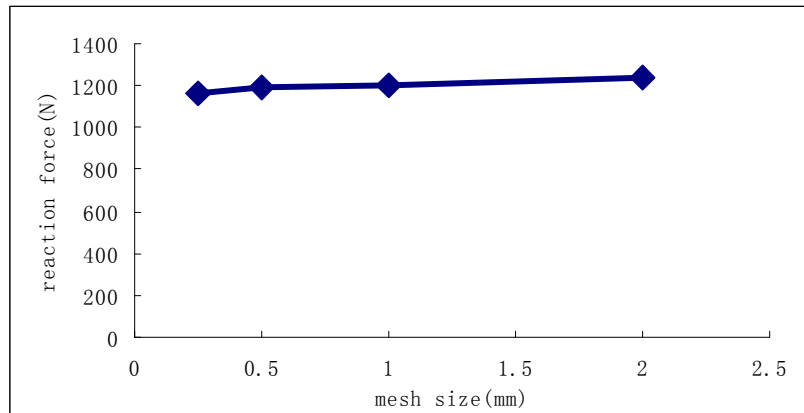


Figure 6-6 Boundary conditions of the FE model

## 6.5 Mesh Sensitive Analysis

To minimize the effect of mesh density on the simulation results, a mesh sensitive analysis was conducted by applying a prescribed displacement load on the load point with different element sizes, then, the reaction forces at the load point were recorded for evaluation. The reaction force at a prescribed displacement of 1.93 mm was used. This is the starting point of the damage according to Brindle [14]. The mesh sensitive analysis for 2D configuration is shown in Figure 6-7. The results for the 3D model are seen in Figure 6-8. In Figure 6-7, the reaction force differences between adjacent element sizes are all less than 5% which is widely acceptable and an element size 0.5 mm was

chosen to calculate the quasi-static contact load. For the continuum shell element the same element size 0.5 mm was used.



**Figure 6-7 Results of mesh sensitive analysis for 2D**

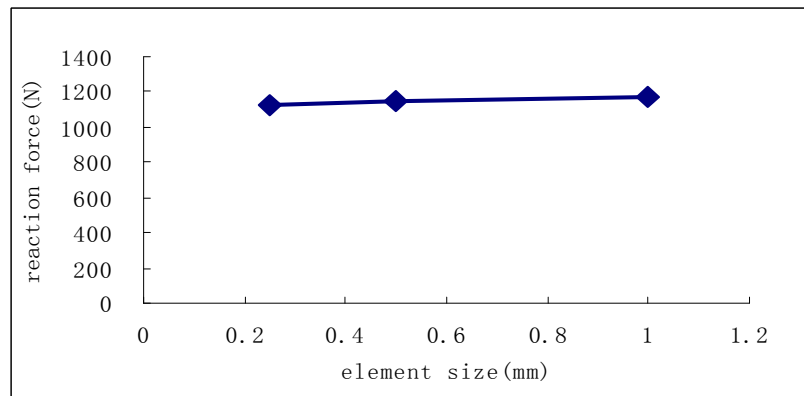


**Figure 6-8 Results of mesh sensitive analysis for 3D**

## 6.6 Results and Discussion

The contact forces of both FE models (2D and 3D) at the prescribed displacement of 1.93 mm when the stiffness of the composite laminate decreases sharply was shown in Table 6-2. In addition, the comparison between FEA results and experimental data are included in the table. The contact force versus displacement curves are shown in Figure 6-9. The contact force is four times that of the FE results because only one quarter of the plate is built in the FE model.

**Table 6-2 Contact force comparison with different element types**

	Contact Force (kN)	Error (%)
QSL Test Result	5.05	-
FEM (Conventional Shell Element)	5.27	4.4
FEM (Continuum Shell Element)	4.80	-5.0

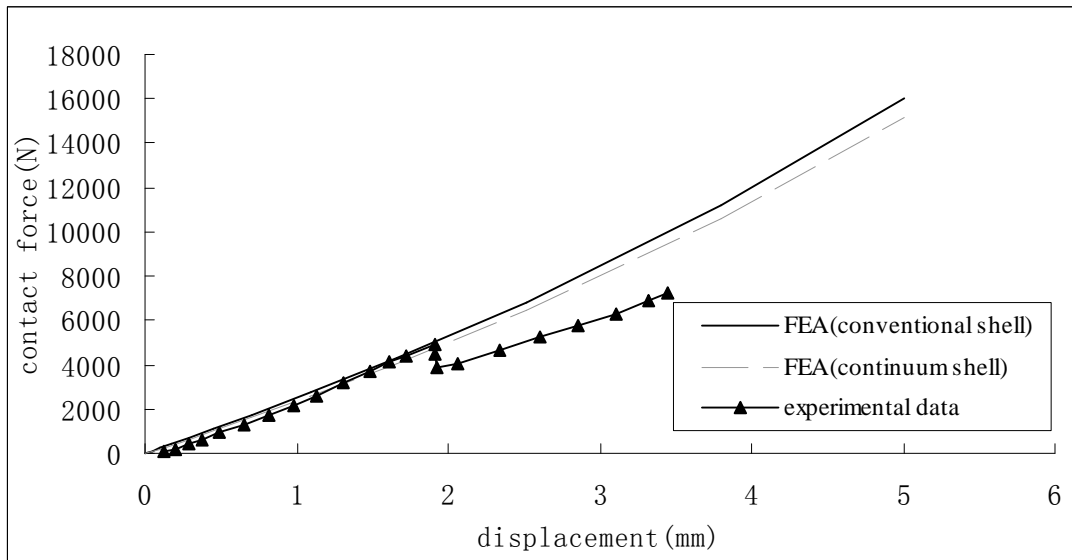


**Figure 6-9 Comparison of contact force versus displacement**

Both conventional shell (2D) and continuum shell (3D) elements were validated for simulating contact force before damage start in the QSL test. However, the conventional shell elements cannot be stacked to simulate the interface between different layers which means cohesive elements must be modelled in continuum shell elements. Because of that, continuum shell elements were used in the following chapters to insert cohesive elements between continuum shell elements. Apart from that, simple fixed boundary conditions and element sizes of 0.5 mm were used in the above verses. This will be used in the next chapter to simulate delamination in the composite laminate.



## **7 DAMAGE SIMULATION OF CROSS-PLY LAMINATE**

### **7.1 Specimen Description**

Experimental results in Aymerich's paper [62] were used to study the damage process of cross-ply laminate under LVI. The stacking sequence of the cross-ply plate is  $[90_3/0_3]_s$  with a thickness of about 2 mm. The composite plates were 65 mm × 87.5 mm in size which were simply supported by a steel plate and there is a 45 mm × 67.5 mm rectangular cutout underneath the plate. The hemisphere impactor weighs 2.3 kg with a diameter of 12.5 mm.

### **7.2 FE Model Description**

Only one quarter of the plate was built in the FE model because of the symmetry of the plate. The layers of the plate were simulated with continuum shell element SC8R while the interfaces between layers with different fibre orientation were modelled with 3D cohesive elements COH3D8. At the bottom layer where most of the matrix crack happened, vertical cohesive elements were set up to simulate the matrix crack. The vertical cohesive elements were placed parallel to the fibre direction on the symmetry plane. Because there is no interface delamination between layers with the same fibre orientation, only two layers of cohesive elements were inserted into the delaminated interface. At the centre of impact, the element size of the laminate is 0.25 mm while the cohesive elements size is 0.05 mm. The impactor was modelled using an analytical rigid body which means there is no deformation of the impactor. This is feasible because of the relatively small deformation of the impactor compared with the laminate. FE model is shown in figure 7-1.

The size of the FE plate model is 45 mm × 67.5 mm which is exactly the same size as the rectangular opening underneath the laminate plate. The simply supported boundary conditions were used in this analysis.

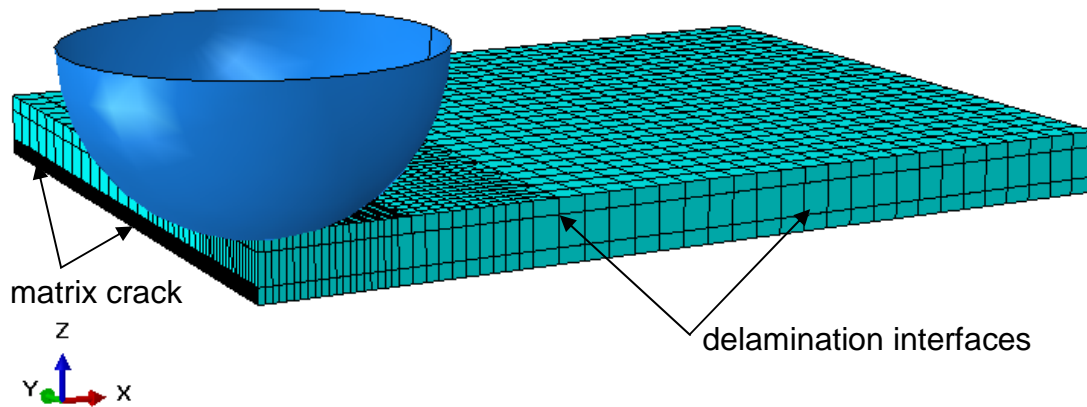


**Figure 7-1 FE model of cross-ply plate**

Unlike the research work done by Aymerich [62] where solver ABAQUS/Explicit was used, ABAQUS/Standard was employed. At the same time, QSL load was used in this paper instead of the dynamic load used in Aymerich [62]'s work.

The material properties used in this simulation are listed in table 7-1.

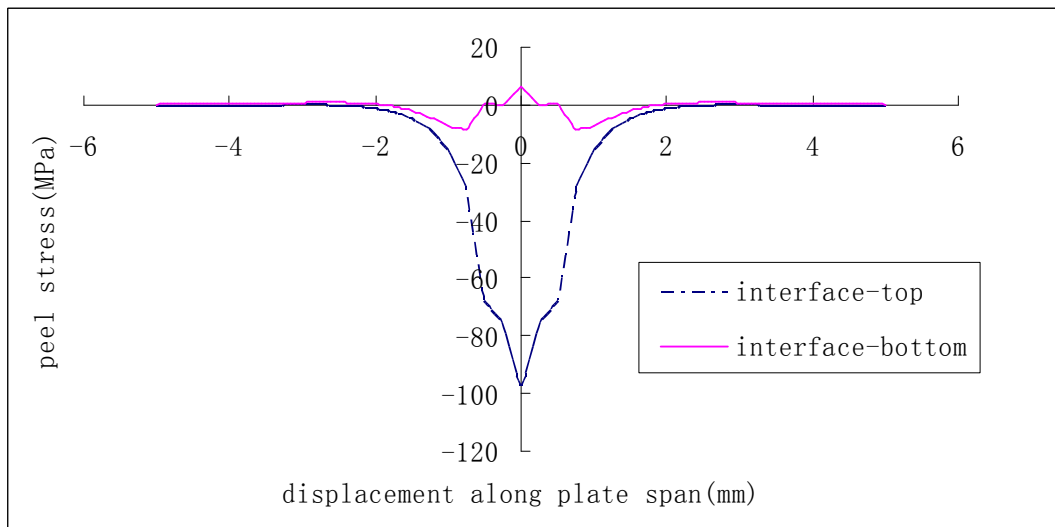
**Table 7- 1 Material properties of the laminate plate [62]**

Laminate								
$E_{11}$ (MPa)	$E_{22}$ (MPa)	$E_{33}$ (MPa)	$\nu_{12}$	$\nu_{23}$	$\nu_{13}$	$G_{12}$ (MPa)	$G_{13}$ (MPa)	$G_{23}$ (MPa)
93700	7450	7450	0.261	0.261	0.261	3970	3970	3970
Interface								
$G_{IC}$ (N/mm)	$G_{IIC}$ (N/mm)	$G_{IIIC}$ (N/mm)	$k_N$ (N/mm <sup>3</sup> )	$k_S$ (N/mm <sup>3</sup> )	$k_T$ (N/mm <sup>3</sup> )	N (MPa)	S (MPa)	T (MPa)
0.52	0.97	0.97	120000	48000	48000	30	80	80

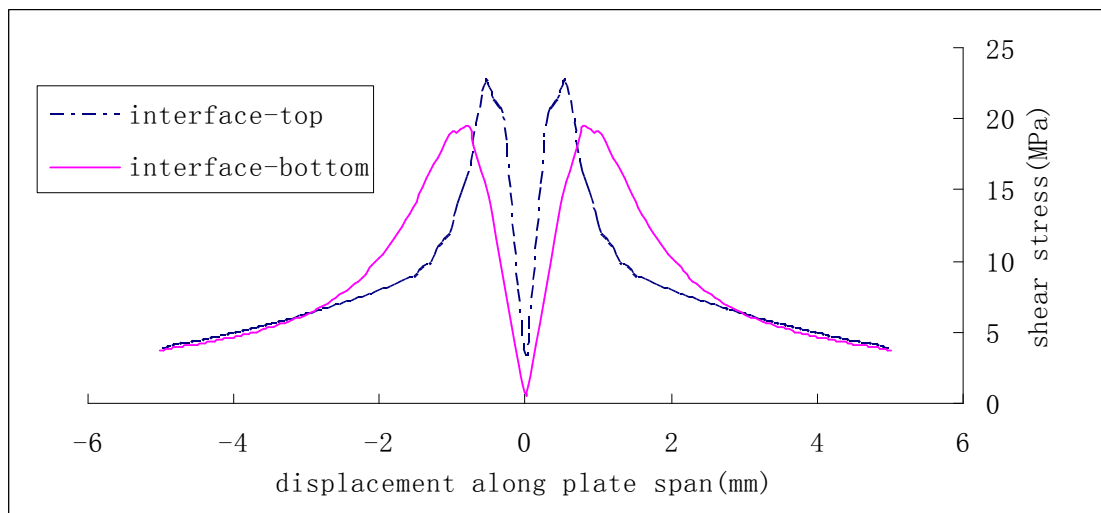
The value of  $G_{IIIC}$  was adopted from mode II fracture toughness  $G_{IIC}$ .

### 7.3 Simulation Results

The stress distribution at the top and bottom interface before delamination initiation was studied first. The results are illustrated in figure 7-2 and figure 7-3. The displacement of the impactor is about 0.3 mm and the reaction force is about 230 N.



**Figure 7- 2 Peel stress distribution along the plate span**

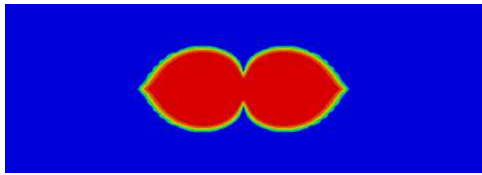
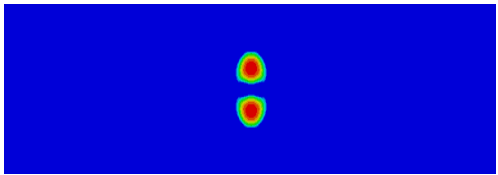
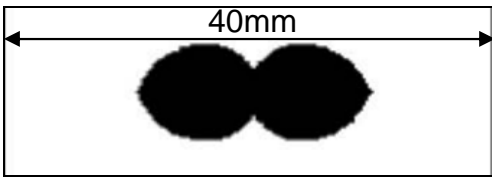


**Figure 7- 3 Transverse shear stress distribution along the plate span**

As can be seen in figure 7-2 and figure 7-3, the stress distribution for this laminate has the same overall shape as the results in chapter 3.4. Very high compressive stress exists at the top interface which will delay delamination. This agreed well with the experimental results that little delamination was observed.

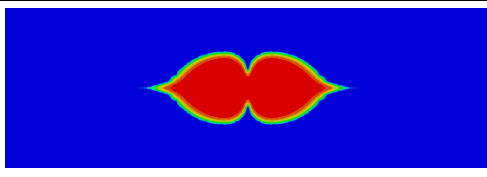
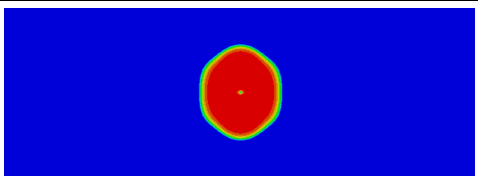
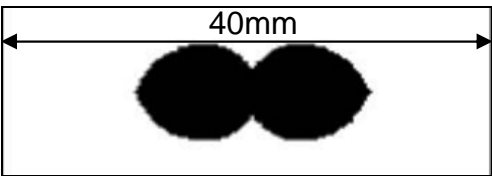
After that, delamination simulation was carried out taking into account the friction action at the top interface where there was higher compressive load. A value of 0.9 for the coefficient was used in this simulation. The delamination

area comparison between finite element model results and experimental results is shown in figure 7-4. Very good agreement between the FE results and experimental data was achieved as can be seen in the figure below. The delamination area at the top interface was not available for this particular layup, but for the laminate plate with stacking sequence of  $[0_3/90_3]_s$ , a minor delamination area which developed on the top interface was observed.

	bottom interface	top interface
FE		
X-ray		Not given in the paper

**Figure 7-4 Comparison between FE models and experiment with friction**

The comparison between the FE model and experiment in terms of delamination area without taking friction into account is shown in figure 7-5.

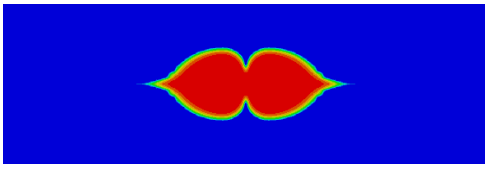
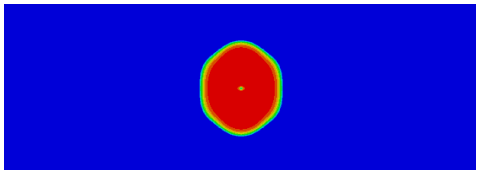
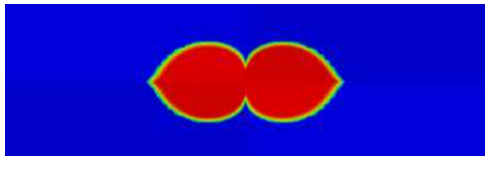
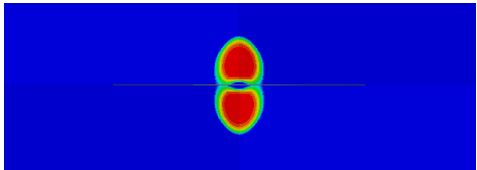
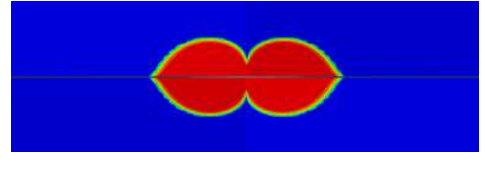
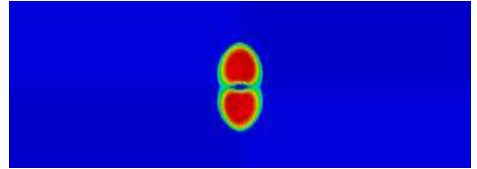
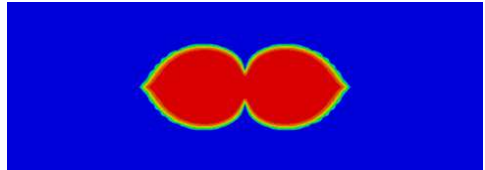
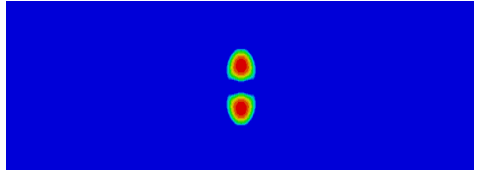
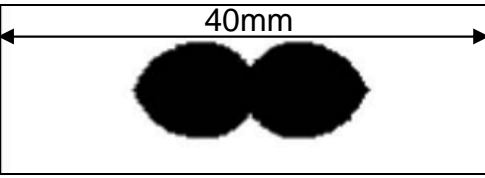
	bottom interface	top interface
FEM		
X-ray		Not given in the paper

**Figure 7-5 Comparison between FE models and experiment without friction**

As can be seen in figure 7-5, a larger delamination area was mistakenly predicted without taking account the action of friction at the top interface. In other words, the compressive load at the interface actually delays the initiation of delamination. Because the impact energy for both interfaces is the same, when the larger delamination area was observed at the top interface, a smaller

delamination area was predicted without taking account the friction action at the bottom interface.

A sensitivity analysis of coefficient of friction was also conducted to investigate the friction effect between the lamina. The delamination areas at both bottom and top interfaces were studied using different value from the coefficient of friction of 0.5, 0.75 and 0.9 respectively. The results are illustrated in figure 7-6.

CF	bottom interface	top interface
No friction		
0.5		
0.75		
0.9		
X-ray		Not given in the paper

**Figure 7-6 Comparison between different CF in terms of delamination areas**

As can be seen in figure 7-6, the delamination areas at the top interfaces are sensitive to the coefficient of friction where high compressive load exists. However, the delamination areas at the bottom interfaces show no sensitivity to the coefficient of friction because of the lower compressive load.

The plot showing impactor displacement versus reaction force is illustrated in figure 7-7. The FE results and experimental data showed very good agreement

at the beginning of the impact. At a displacement of about 1mm, a slight discrepancy was observed. This discrepancy mainly arises from the fact that some types of impact damage, like the indentation at the top surface and matrix cracking in other positions, were not considered.

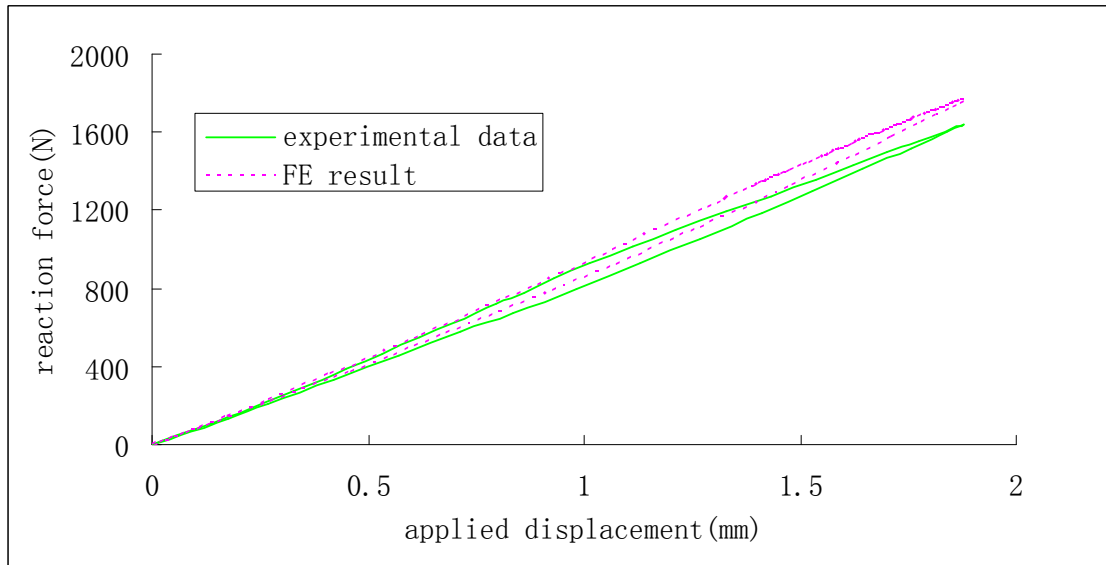


**Figure 7-7 Applied displacement versus reaction force for cross-ply laminate**

The delamination area had a peanut shape with its main axis along the fibre orientation of the lower ply as can be seen in figure 7-4. This phenomenon is mainly attributed to matrix cracking happening at an early stage of the impact events. In order to understand the relationship between matrix crack and interface delamination, the peel and transverse shear stress distribution was compared between models with or without consideration of matrix crack. Firstly, stress distribution at the top interface is shown in figure 7-8 and figure 7-9.

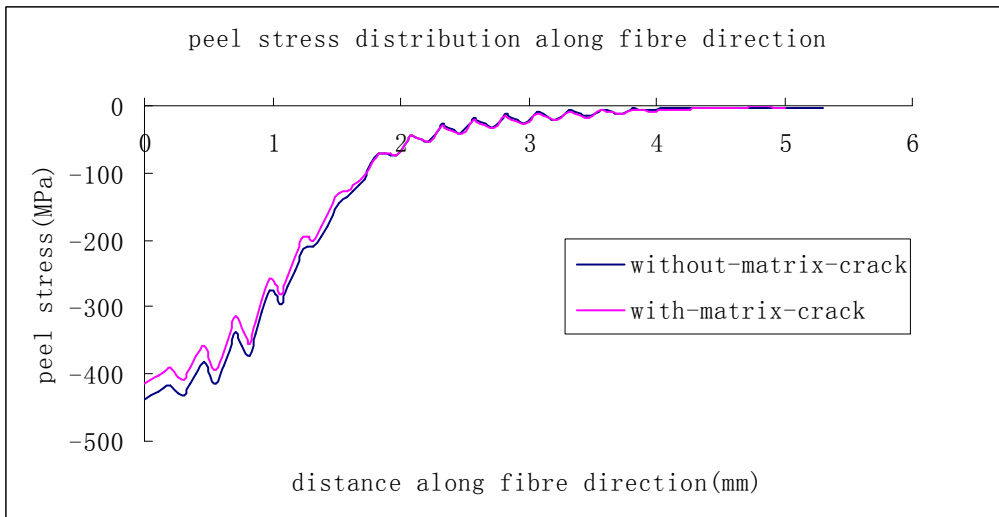


**Figure 7-8 Peel stress distribution along fibre direction of the lower ply**

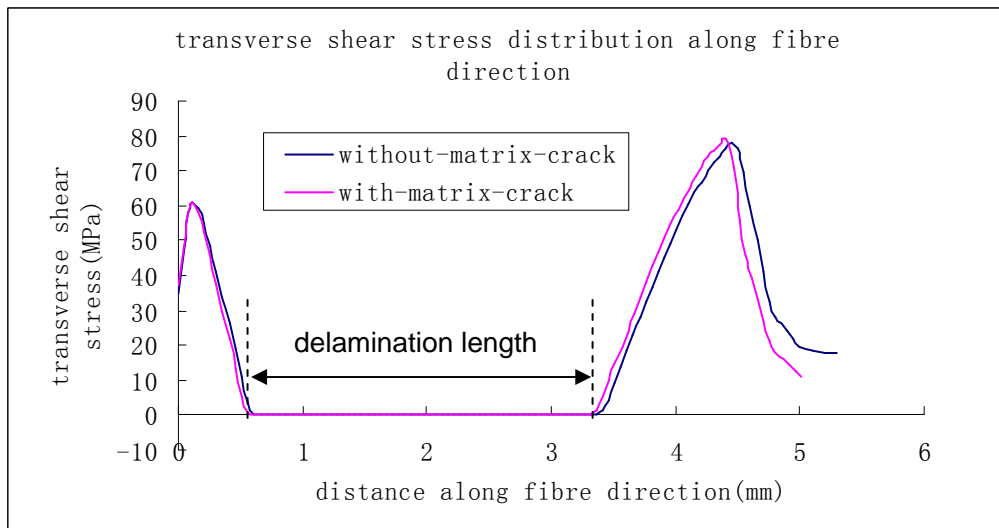


**Figure 7-9 Transverse shear stress distribution along fibre direction of the lower ply**

As can be seen above, bending matrix crack which was only simulated at the bottom interface had little influence on the stress distribution at the top interface. The stress component which leads to interface delamination is the transverse shear stress while compressive peel stress will delay the damage initiation at the top interface.

The peel stress distribution at the bottom interface was analysed taking matrix crack into account. Before the matrix crack happens, very small positive peel

stress exists in the bottom interface along the matrix crack direction. After the matrix crack happens, high positive peel stress is observed in the bottom interface along the matrix crack direction and this initiates mode I delamination in this interface. Comparison of peel stress before and after matrix crack is shown in figure 7-10. This phenomenon was also studied by Chang [29].

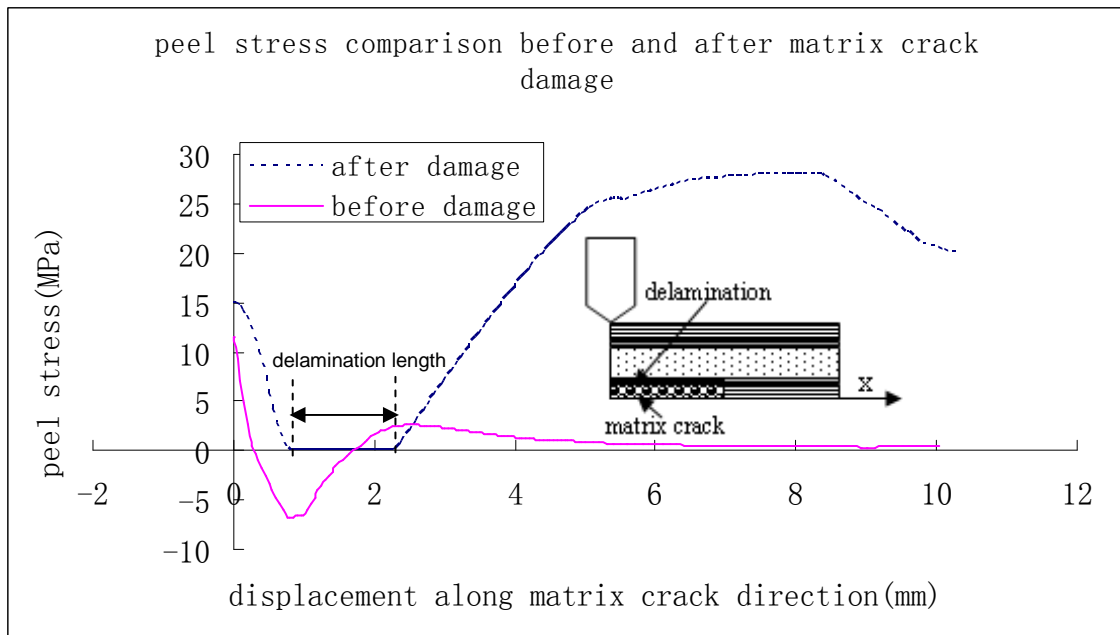


**Figure 7-10 Peel stress comparison before and after matrix crack damage**

After the predominantly model I delamination happened in the bottom interface along the matrix crack direction, delamination propagated in the transverse matrix crack direction. The peel stress distribution in these delamination area along the matrix crack direction is shown in figure 7-11. As can be seen in figure 7-11, the peel stress at the crack tip is very small and so cannot be the main factor inducing delamination.

In order to understand which stress components induce delamination in the transverse matrix crack direction, the transverse shear stress in these areas along the matrix crack direction is also illustrated in figure 7-11. As can be seen in figure 7-11, the transverse shear stress at the delamination areas away from the matrix crack is about 80 MPa which is capable of inducing delamination in these areas.



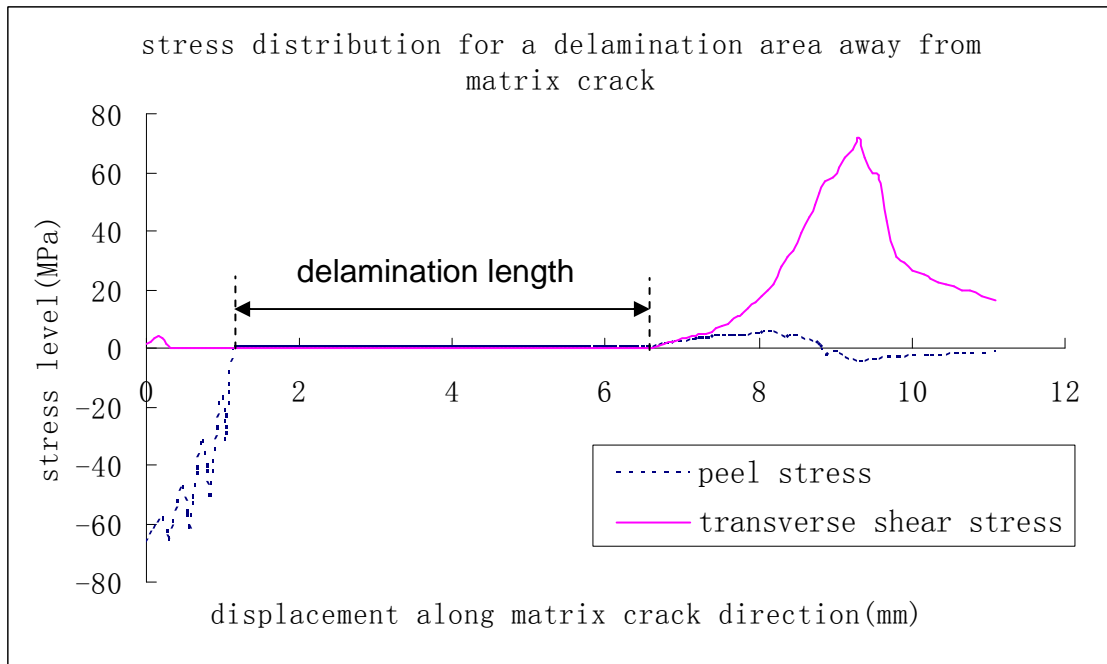


**Figure 7-11 Stress distribution for a delamination area away from matrix crack**

In conclusion, high peel stress existing in the interface along the matrix crack direction induces mode I delamination along the matrix crack. This peel stress driven delamination also explains why the area of delamination is usually observed as a peanut shape with its main axis along the fibre direction of the lower ply. After the peel stress driven delamination along the matrix crack direction occurs, delamination starts to propagate in the transverse matrix crack direction. This is mainly induced by high transverse shear stress existing in these delamination areas as can be seen in figure 7-11.

When matrix crack is taken into account, a more extensive delamination area is observed in the simulation results. Furthermore, a peanut shape delamination area is not observed in the bottom interface when matrix crack in the lowest group of plies is not taken into account. Comparison of the delamination area with and without consideration of matrix cracks together with the experimental results is shown in figure 7-12.

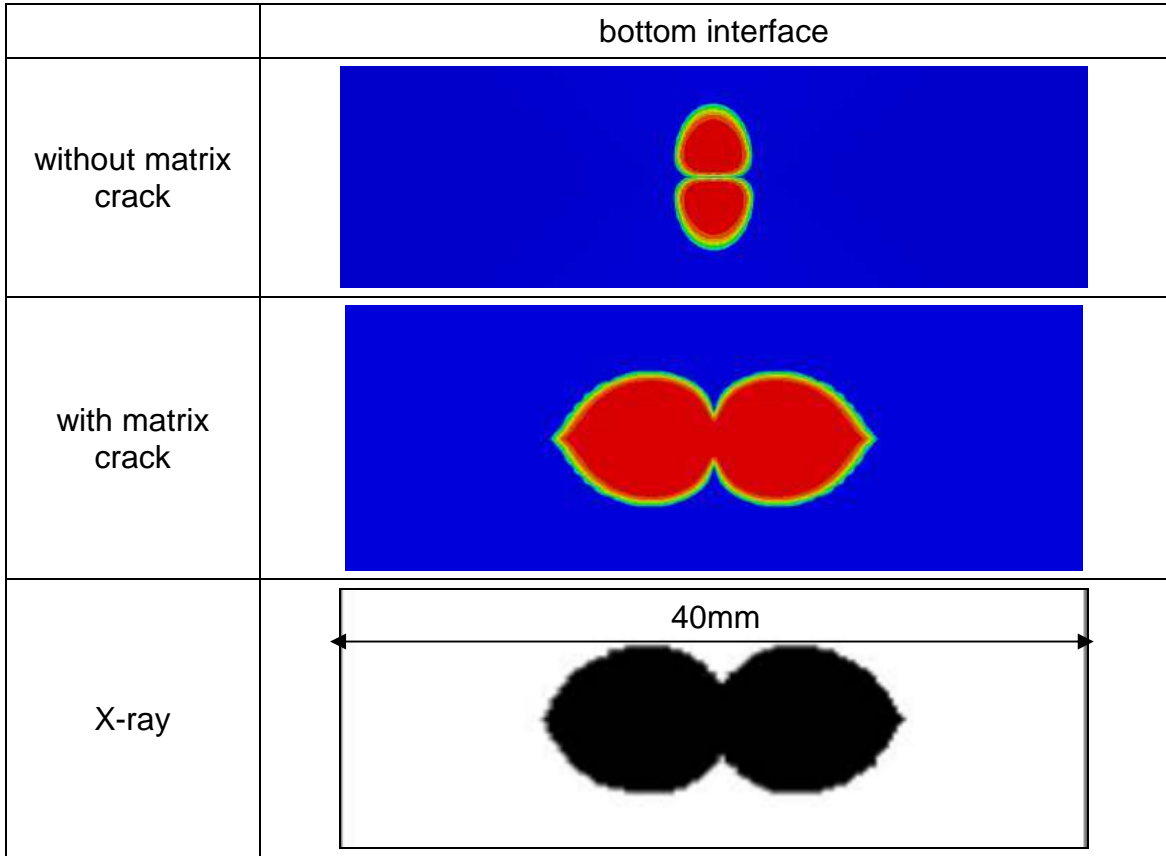


**Figure 7-12 Comparison of delamination area with and without matrix crack together with the experimental results**

## 8 DAMAGE SIMULATION OF CLUSTERED LAMINATE

### 8.1 Specimen Description

González [8] carried out tests to investigate the ply clustering effect in composite plate subjected to low-velocity impact. In order to study the clustering effect, two different quasi-isotropic stacking sequences of the plates proposed are  $[(45_2/0_2/-45_2/90_2)_2]_s$  and  $[45_4/0_4/-45_4/90_4]_s$ . In the following, these plates are named as L2 and L4 respectively. All laminates have 32 different plies with the same thickness which is about 5.8 mm. The composite plates were 150 mm × 100 mm in size and the orientation of the  $0^\circ$  fibre is along the longer in-plane dimension of the plates. The plates were simply supported by a steel plate with a 45 mm × 67.5 mm rectangular cutout just underneath the plates. The diameter of the hemisphere impactor is not specified in González [8]'s paper, so an impactor diameter of 16 mm was selected in this thesis.

### 8.2 FE Model Description

In order to simulate the matrix crack orientated along  $45^\circ$  at the bottom of the laminate, the whole plate was built in FE model because the plate is not symmetric when  $45^\circ$  and negative  $45^\circ$  plies are taken into account. The plies of the plate were simulated using continuum shell element SC8R while the interfaces between plies with different fibre orientation were modelled with 3D cohesive elements COH3D8.

For the L4 configuration, as can be seen at the bottom in figure 8-1, most of the delamination happened at the bottom half of the laminate and clearly was orientated in the fibre direction of the lower plies. Accordingly, vertical cohesive elements were set up in each of the plies at the bottom half to simulate the matrix crack and only delaminations at the bottom half were considered for L4. For the L2 configuration, only delamination at the lowest interface observed clear orientation as shown in figure 8-1, but matrix cracks act as initial points for delamination. So matrix cracks in each of the plies at the bottom half were simulated and also only delaminations at the bottom half were taken into account.

Impact energy=19.3J

Impact energy=28.6J

Impact energy=38.6J

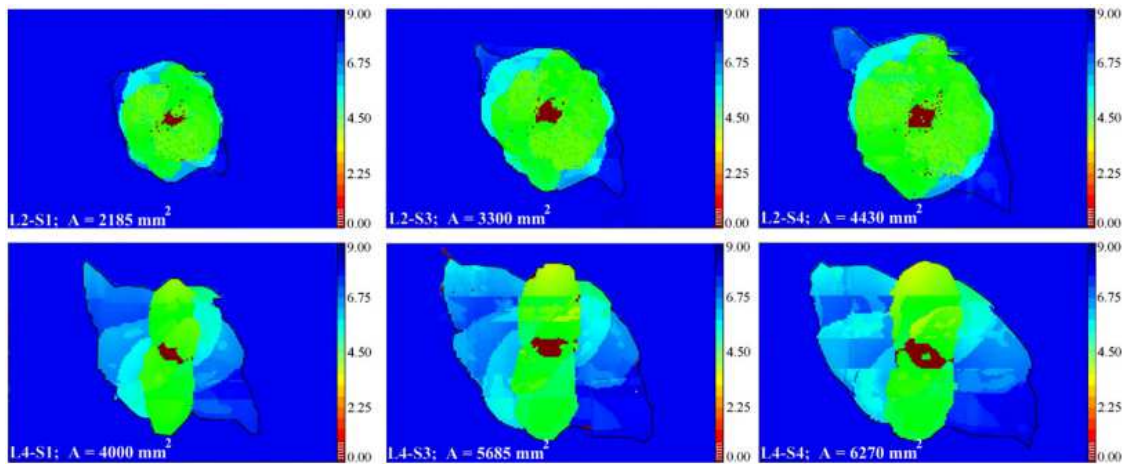


**Figure 8-1 C-scan delamination results of L2 and L4 [8]**

In order to simulate matrix crack, vertical cohesive elements were placed parallel to the fibre direction at the symmetric plane. Because there is no interface delamination between layers with the same fibre orientation, for clustering laminate L2 and L4, fewer delamination interfaces exist which simplifies the simulation. At the centre of the area of impact, the element size of the laminate is 0.5 mm while the cohesive elements size is 0.2 mm. The cohesive elements size for this model is bigger than the recommended value which is one fifth of the laminate elements size because of the limitations of calculation. The impactor was modelled using an analytical rigid body which means there is no deformation of the impactor. This is feasible considering the relatively small deformation of the impactor compared with that of the laminate. FE models L2 and L4 are shown in figure 8-2. Seven different delaminated interfaces are taken into account for the L2 model, while only 3 different delaminated interfaces are considered for L4 model. The bottom of figure 8-2 shows the 45° ply with matrix crack inserted in the symmetric plane.

The size of the FE plate model is 150 mm × 100 mm which is exactly the same size as the laminate plate, four rubber-tipped clamp points are also considered in this FE model. The simply supported boundary condition was used in this analysis. The set up of the test is illustrated in figure 8-3.

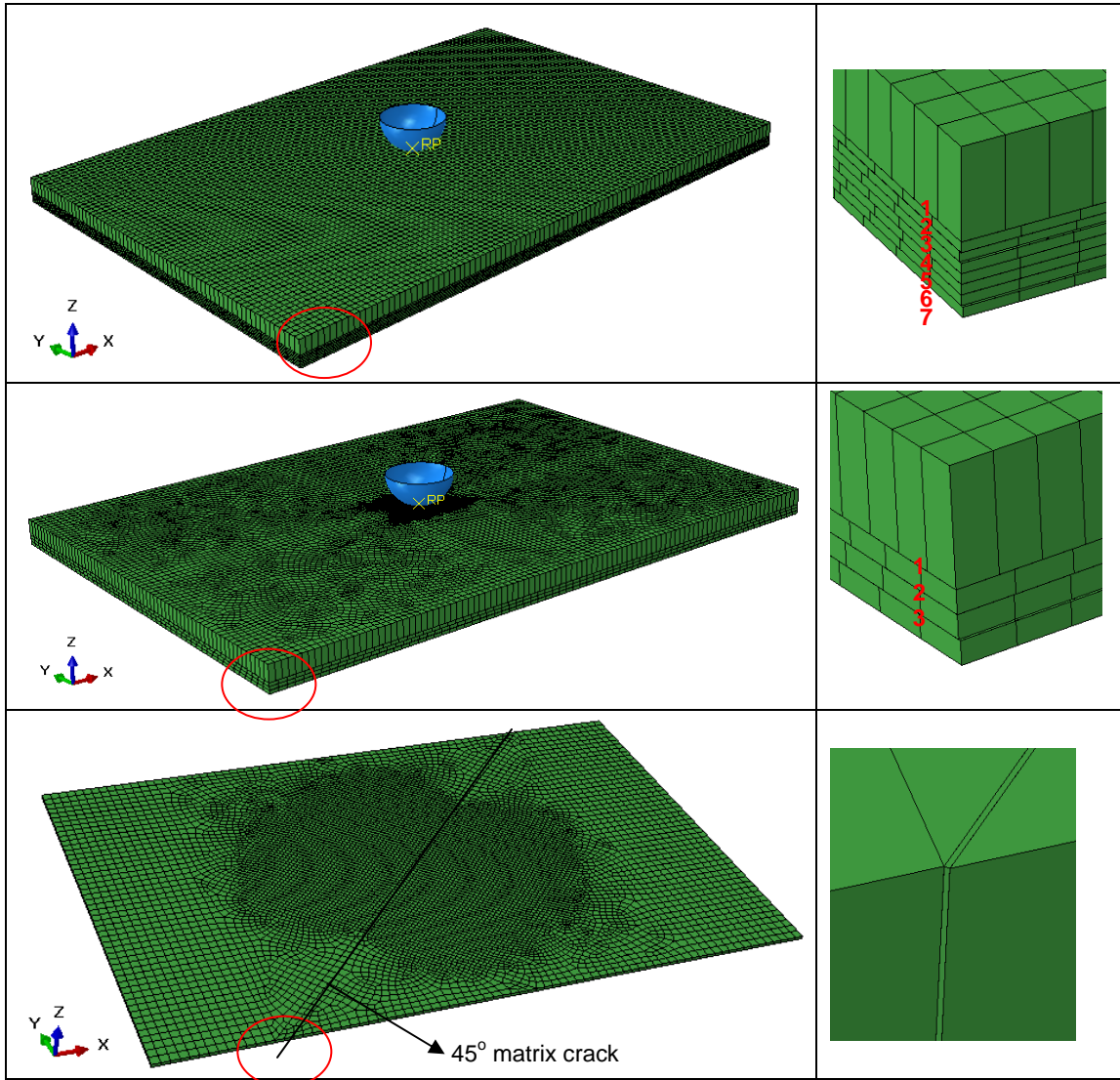


Figure 8-2 FE models of Quasi-Isotropic composite plates

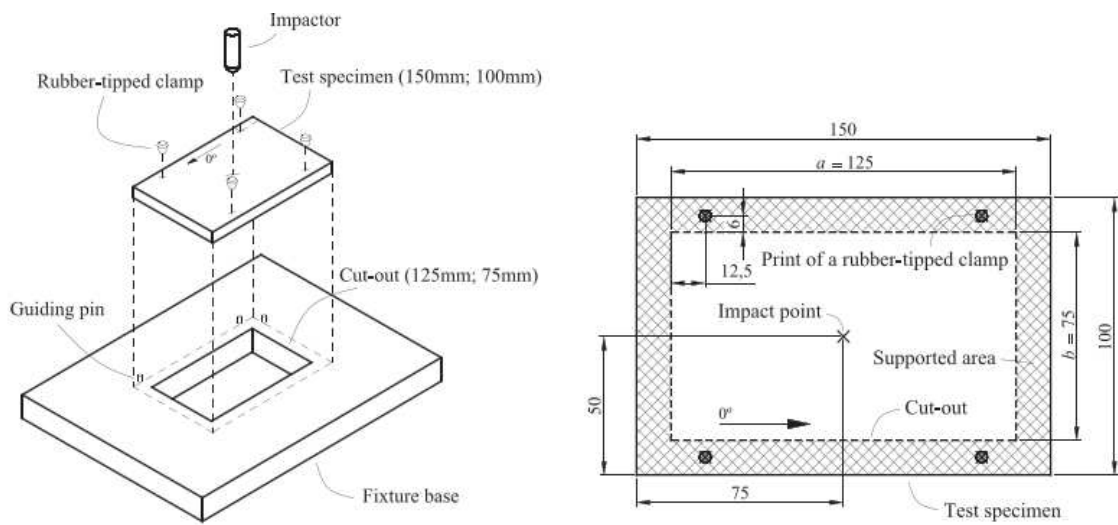


Figure 8-3 Set up of the impact test of clustering laminates [8]

ABAQUS/Standard was employed in this work. At the same time, QSL load was used in this paper instead of dynamic load. Displacement load was used in the FE analysis.

The material properties used in this simulation were listed in table 8-1.

**Table 8-1 Material properties of the laminate plate [8]**

lamina								
$E_{11}$ (MPa)	$E_{22}$ (MPa)	$E_{33}$ (MPa)	$\nu_{12}$	$\nu_{23}$	$\nu_{13}$	$G_{12}$ (MPa)	$G_{13}$ (MPa)	$G_{23}$ (MPa)
93700	7450	7450	0.261	0.261	0.261	3970	3970	3970
interface								
$G_{IC}$ (N/mm)	$G_{IIC}$ (N/mm)	$G_{IIIC}$ (N/mm)	$k_N$ (N/mm <sup>3</sup> )	$k_S$ (N/mm <sup>3</sup> )	$k_T$ (N/mm <sup>3</sup> )	N (MPa)	S (MPa)	T (MPa)
0.52	0.97	0.97	120000	48000	48000	30	80	80

The value of  $G_{IIIC}$  was adopted from mode II fracture toughness  $G_{IIC}$ .

### 8.3 Simulation Results

The reaction load versus applied displacement for the L4 configuration is illustrated in figure 8-4.

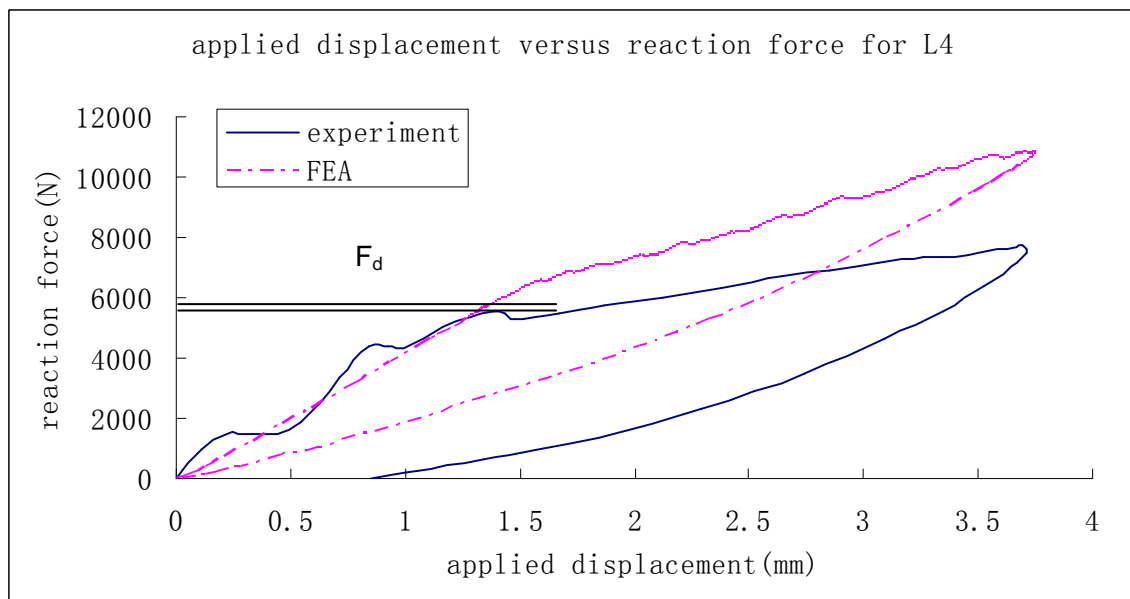


**Figure 8-4 Applied displacement versus reaction load comparison for L4**

For the L4 configuration, according to the experimental results the prescribed displacement is about 3.75 mm under 19.3 J impact energy.

As can be seen in figure 8-4, good agreement was achieved between experimental results and the FE simulation results in terms of reaction load versus applied displacement. The sudden load drop happened when the reaction load was about 5335 N in the FE analysis while the experimental threshold load was about 5600 N.

For the FEA simulation, the applied displacement of the impactor came to zero at the end of the impact. But, for the test, the applied displacement of the impactor which is also called impactor indentation is about 0.8mm when the impact stops. The difference is mainly attributed to the elastic reaction of the laminate in the FEA simulation which means the plastic indentation of the laminate is not taken into account in the model.

The delamination areas for interface 1, 2 and 3 (see figure 8-2) are shown in figure 8-5.

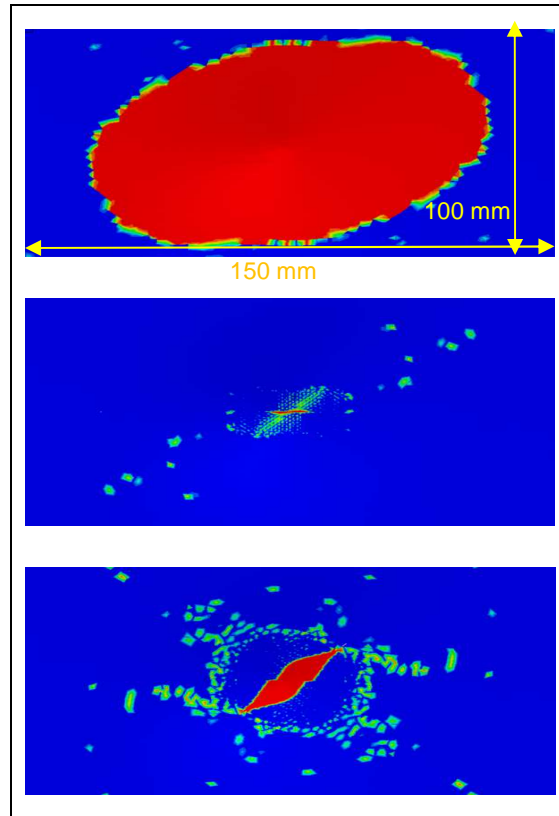


**Figure 8-5 Delamination area for interface 1, 2 and 3 of L4**

As can be seen in figure 8-5, the delamination areas were different from the experimental results. However, for interface 3, the delamination area was found to be a peanut shape with the main axis lying along the fibre direction in the lower ply. A larger delamination area was observed at interface 1 in the FE simulation, this result is mainly attributed to the high compressive load which was not taken into account in this FE model.

For the L2 configuration, the prescribed displacement is about 3.40 mm under 19.3 J impact energy according to the experimental results. Because of the excessive time required for the calculation, only 65% of the job submitted was completed for L2

The reaction load versus applied displacement for L2 configuration is illustrated in figure 8-6.

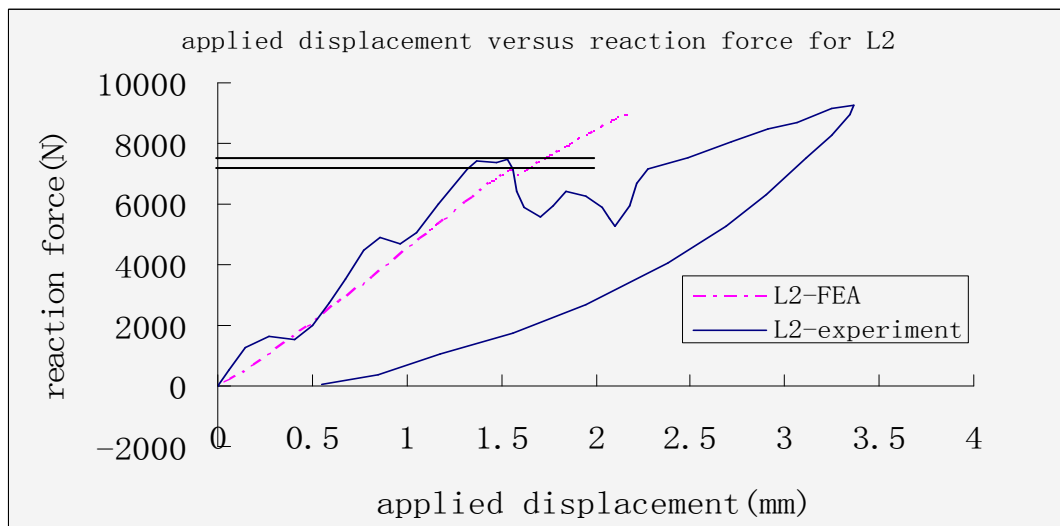


**Figure 8-6 Applied displacement versus reaction load comparison for L2**

As can be seen in figure 8-6, good agreement was achieved between experimental results and the FE simulation results in terms of reaction load versus applied displacement. The sudden load drop happened when the reaction load was about 7200 N in the FE analysis while the experimental threshold load was about 7400 N.

The delamination areas for interface 1(top), 2, 3, 4, 5, 6 and 7 (see figure 8-2) are shown in figure 8-7.



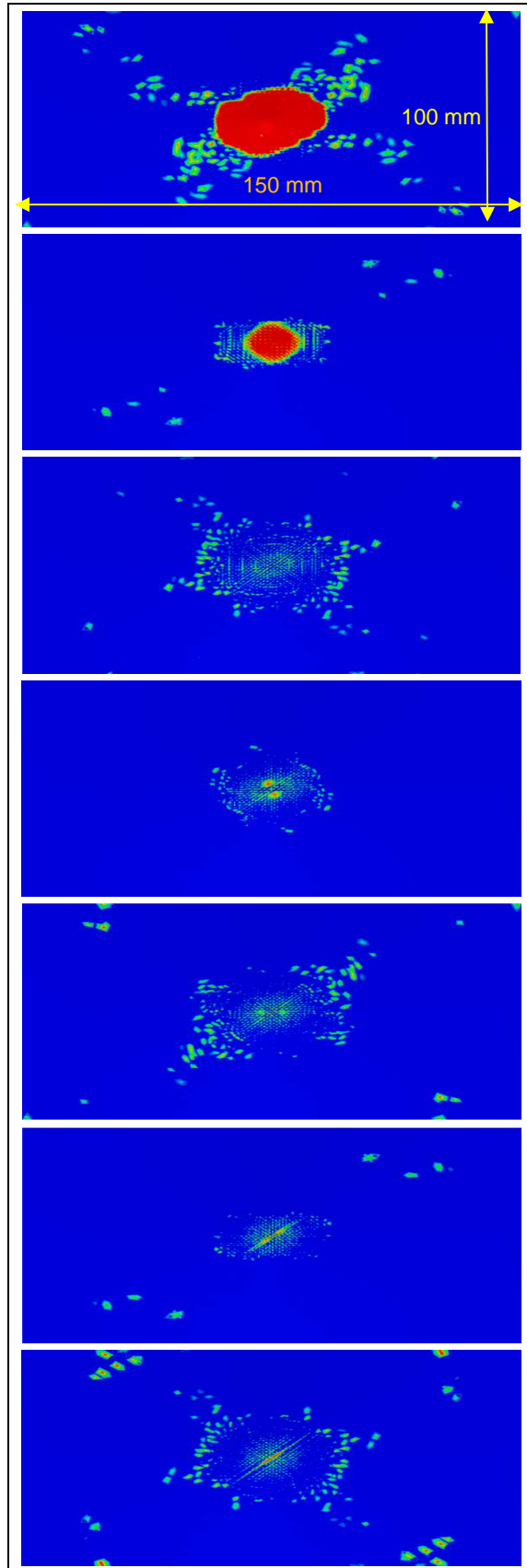


Figure 8-7 Delamination area for interface 1, 2 and 3 of L2

As can be seen in figure 8-7, the delamination areas were different from the experimental results (see figure 8-1). A larger delamination area was observed at interface 1 in the FE simulation, this result is mainly attributed to the high compressive load which was not taken into account in this FE model. The other factor which may affect the simulation results is the position and numbers of the matrix cracking. To simplify the simulation, only one single layer of matrix cracking was inserted at the middle of each lamina which is not true according to the research work of Chang [29].

#### **8.4 Conclusion**

In conclusion, for Quasi-Isotropic (QI) composite laminates, especially for L2 configuration, because there are more interfaces which can delaminate, more interface elements are needed and this caused the calculation to take longer.

Because compressive load in the interfaces can delay the delamination, future FE models need to take compressive load into account either by simulating friction between plies or using a new damage initiation criterion.

In order to simplify the simulation, only one single layer of matrix crack was inserted at the symmetric plane of the plies at the bottom half. However, several matrix cracks which located several millimetres away from the impactor were observed in the plies according to the experimental results.

## 9 CONCLUSION

A stress distribution study around the impact area found that impact damage is caused by the higher stress near the impactor. The stress level at the areas away from the impactor is lower which cannot induce damage. The higher stress near the impactor will cause matrix cracks which act as initial points for delamination. Furthermore more delamination was observed at the bottom half of the plate where positive in-plane tension stress induces more matrix crack in the transverse fibre direction. Another important factor which will delay delamination at the top half of the plate is the higher compressive load in the thickness direction.

The use of cohesive elements to simulate interlaminar delamination were validated and calibrated by the DCB and ENF FE model. The bilinear traction-separation law employed by the cohesive element was also verified.

Continuum shell elements were found to be suitable to simulate composite laminate under impact. Good agreement in terms of reaction force versus impactor displacement was achieved between experimental results and FE simulation.

Good agreement in terms of delamination area and reaction force between experimental results and FE simulation have shown that the FE model using cohesive elements was capable of predicting the impact damage in cross-ply laminates. Matrix crack simulation is very important in producing peanut shape delamination with its main axis along the fibre direction at the lower ply. Friction action was found to be capable of simulating the delayed effect of delamination in the top half of the laminate where high compressive load exists in the thickness direction.

The results showed that cohesive elements obeying the bilinear traction-separation law were capable of predicting the reaction force in quasi-isotropic laminates. However, discrepancies with the test results in terms of delamination area were observed for quasi-isotropic laminates. These discrepancies are mainly attributed to the simplification of matrix cracks simulation and

compressive load at the interface in the thickness direction which is not taken into account.

In order to simplify the FE model, only one line of the vertical cohesive elements, used to simulate matrix cracks, was inserted in the symmetric plane of the plate. However, matrix cracks usually happen at a certain distance away from the impactor and several matrix cracks may happen in a single ply. Because the interaction between matrix crack and delamination is very important, simulating matrix crack using a more accurate method is the next stage in this work.

Apart from matrix crack simulation, compressive load at the bottom half of the quasi-isotropic laminate is also needed to take into account in the future work. The compressive load in the interface can delay delamination which can be simulated either by simulating friction between plies or using a new damage initiation criterion.

## REFERENCES

1. Soutis C, Fibre reinforced composites in aircraft construction. *Progress in Aerospace Sciences* 2005; 41(2): 143-151.
2. Boeing Company. Advanced technology employed in 787 dreamliner. Available: <http://www.boeing.com/commercial/787family/background.html>.
3. Johnson W.S, Mangalgiri P.D. Investigation of fibre bridging in double cantilever beam specimens. NASA Technical Memorandum 87716, 1986.
4. FAA AC20-107B, 2009. Composite aircraft structures. U.S Department of Transportation Federal Aviation Administration.
5. Sjoblom P.O, Hartness J.T, Cordell T.M. On low-velocity impact testing of composite materials. *Compos Mater* 1988; 22(1): 30–52.
6. Papanicolaou, G.C, Stavropoulos C.D. New approach for residual compressive strength prediction of impacted CFRP laminates. *Composites* 1995; 26(7): 517-523.
7. Lopes C.S, Seresta O, Coquet Y, Gurdal Z, Camanho P.P, Thuis B. Low-velocity impact damage on dispersed stacking sequence laminates. Part I: experiments. *Composites Science Technology* 2009; 69(7–8): 926–36.
8. González E.V, Maimí P, Camanho P.P, Lopes C.S, Blanco N. Effects of ply clustering in laminated composite plates under low-velocity impact loading. *Composites Science and Technology* 2011; 71(2011): 805–817.
9. Tay T.E. Characterization and analysis of delamination fracture in composites: an overview of developments from 1990 to 2001. *Appl Mech Rev* 2003; 56(1): 1–32.
10. Krueger R. Virtual crack closure technique: history, approach, and applications. *Appl Mech Rev* 2004; 57(2): 109–43.
11. Mi Y, Crisfield M.A, Davies G.A.O, Hellweg H.B. Progressive delamination using interface elements. *Compos Mater* 1998; 32(14): 1246–73.
12. Borg R, Nilsson L, Simonsson K. Modelling of delamination using a discretized cohesive zone and damage formulation. *Compos Sci Technol* 2002; 62: 1299–314.
13. Zou Z, Reid S.R, Li S. A continuum damage model for delaminations in laminated composites. *Mech Phys Solids* 2003; 51: 333–56.

14. Brindle A.R, Zhang X. Predicting the damage tolerance of carbon-fibre coupons based on impact response. MSc Thesis 2007; Cranfield University.
15. Lee J, Soutis C. Prediction of Impact-Induced Fibre Damage in Circular Composite Plates. *Applied Composite Material* 2005; 12: 109–131.
16. Abrate S. *Impact on composite structures*. Cambridge: Cambridge University Press 1998.
17. Richardson M.O.W, Wisheart M.J. Review of low-velocity impact properties of composite materials. *Composites Part A: Applied Science and Manufacturing* 1996; 27(12): 1123-1131.
18. Davies, G.A.O, Zhang X. Impact damage prediction in carbon composite structures, *International Journal of Impact Engineering* 1995; 16(1): 149-170.
19. Schoeppner G.A, Abrate S. Delamination threshold loads for low velocity impact on composite laminates, *Composites Part-A: Applied Science and Manufacturing* 2000; 31(9): 903-915.
20. Olsson R. Mass criterion for wave controlled impact response of composite plates. *Composites Part A: Applied Science and Manufacturing (UK)* 2000; 31A (8): 879-887.
21. Beks F.A. Examination of impact response and damage of composite laminates. FFA TN1996-29, Bromma, Sweden: The Aeron.Res.Inst. of Sweden, 1996.
22. Cantwell W.J, Wotton J. Comparison of the low and high velocity impact response of CFRP. *Composites* 1989; 20(6): 545–51.
23. Morita H, Adachi T, Tateishi Y, Matsumoto H. Characterization of impact damage resistance of CF/PEEK and CF/toughened epoxy laminates under low and high velocity impact tests. *Reinf Plast Compos* 1997; 16(2): 131–43.
24. Zhang X. Impact damage in composite aircraft structures-experimental testing and numerical simulation. *Proc Instn Mech Engrs* 1998; 212(4): 245-259.
25. Aoki Y, Suemasu H, Ishikawa T. Damage propagation in CFRP laminates subjected to low velocity impact and static indentation. *Adv Compos Mater* 2007; 16(1): 45–61.
26. Ogihara S, Takeda N. Interaction between transverse cracks and

- delamination during damage progress in CFRP cross-ply laminates. *Compos Sci Technol* 1995; 54(4): 395–404.
27. Davies G.A.O, Zhang X, Edlund, A. Predicting damage in composite aircraft structures due to low velocity impact. In *Aerotech' 94*, Birmingham, January 1994 (Mechanical Engineering Publications, London).
  28. Nettles A, Douglas M, CENTER G.C.M.S.F. A comparison of quasi-static indentation to low-velocity impact, NASATP–2000–210481, 2000, National Aeronautics and Space Administration, Marshall Space Flight Centre.
  29. Chang F.K, Choi H.Y, Jeng S.T. Study on impact damage in laminated composites. *Mechanics of Materials* 1990; 10: 83-95.
  30. Bouvet C, Castanié B, Bizeul M, Barrau J.J. Low velocity impact modelling in laminate composite panels with discrete interface elements. *International Journal of Solid and Structure* 2009; 46: 2809–2821.
  31. Borg R, Nilsson L, Simonsson K. Simulation of low velocity impact on fiber laminates using a cohesive zone based delamination model. *Compos Sci Technol* 2004; 64: 279–88.
  32. Joshi S.P, Sun C.T. Impact induced fracture in a laminated composite. *Compos Master* 1985; 19: 51-66.
  33. Aymerich, et al. Simulation of multiple delaminations in impacted cross-ply laminates. *Composites Science and Technology* 2009; 69(2009): 1699–1709.
  34. De Moura M.F.S.F, Goncalves J.P.M. Modelling the interaction between matrix cracking and delamination in carbon-epoxy laminates under low velocity impact. *Compos Sci Technol* 2004; 62: 1021–7.
  35. Cantwell W.J, Morton J. The significance of damage and defects and their detection in composite materials: a review. *Strain Anal Eng* 1992; 27(1): 29–42.
  36. Gao S.L, Lim J.K. Three-dimensional characterization of impact damage in CFRPs. *Key Eng Mater* 1998; 141–143: 35–54.
  37. Cartie D.D.R, Irving P.E. Effect of resin and fibre properties on impact and compression after impact performance of CFRP. *Compos Part A-Appl S* 2002; 33(4): 483–93.

38. Diamanti K, Hodgkinson J.M, Soutis C. Detection of low-velocity impact damage in composite plates using lamb waves. *Struct Health Monit* 2004; 3(1): 33–41.
39. Choi H.Y, Chang F.K. A model for predicting damage in graphite/epoxy laminated composites resulting from low-velocity point impact. *Compos Mater* 1992; 26(14): 2134–2169.
40. Reifsnider K.L, Case S.W. *Damage Tolerance and Durability of Material Systems*, Wiley Interscience 2002.
41. Davies G.A.O, Robinson P. Predicting failure by debonding delaminations, In: *Debonding/delamination of composites*, AGARD-CP-530, Advisory Group for Aerospace Research and Development, Neuilly Sur Seine;1992.
42. Irving P.E. *Damage Tolerance in Polymer Composite Aircraft Structures*, (unpublished), Cranfield University UK 2007.
43. Mitrevski T, Marshall I.H, Thomson R. The influence of impactor shape on the damage to composite laminates. *Composite Structures* 2006; 76(1-2): 116–122.
44. Mitrevski T, Marshall I.H, Thomson R, Jones R, Whittingham B. The effect of impactor shape on the impact response of composite laminates. *Composite Structures* 2005; 67(2): 139–148.
45. Feraboli P. Some Recommendations for Characterization of Composite Panels by Means of Drop Tower Impact Testing. *Journal of Aircraft* 2006; 43(6).
46. Feraboli P, Kedward K.T. Enhanced evaluation of the low-velocity impact response of composite plates. *AIAA Journal* 2004; 42(10): 2143-2152.
47. Olsson R, Donadon M.V, Falzon B.G. Delamination threshold load for dynamic impact on plates. *Solids Struct* 2006; 43(10): 3124–41.
48. Suemasu H, Majima O. Multiple delaminations and their severity in circular axisymmetric plates subjected to transverse loading. *Compos Mater* 1996; 30(4): 441–445.
49. Olsson R. Analytical prediction of large mass impact damage in composite laminates. *Compos Part A: Appl Sci Manuf* 2001; 32(9): 1207–15.
50. Abrate S. Modeling of impacts on composite structures. *Compos Struct* 2001;



- 51(2): 129–38.
51. Rybicki E.F, Kanninen M.F. A finite element calculation of stress intensity factors by a modified crack closure integral. *Eng Fract Mech* 1977; 9: 931–938.
  52. Elder D.J, Thomson R.S, Nguyen M.Q, Scott M.L. Review of delamination predictive methods for low speed impact of composite laminates. *Compos Struct* 2004; 66(1–4): 677–83.
  53. Xie D, Biggers Jr S.B. Strain energy release rate calculation for a moving delamination front of arbitrary shape based on the virtual crack closure technique. Part I: formulation and validation. *Eng Fract Mech* 2006; 73: 771–785.
  54. David J Elder, et al. Review of delamination predictive methods for low speed impact of composite laminates. *Composite Structures* 2004; 66(2004): 677–683.
  55. Mi Y, Crisfield M.A, Davies G.A.O, Hellweg H.B. Progressive delamination using interface elements. *Compos Mater* 1998; 32(14): 1246–72.
  56. Wisheart M, Richardson M.O.W. The finite element analysis of impact induced delamination in composite materials using a novel interface element. *Compos Part-A. Appl S* 1998; 29: 301–13.
  57. Geubelle P.H, Baylor J.S. Impact-induced delamination of composites: a 2D simulation. *Compos Part-B. Eng* 1998; 29: 589–602.
  58. Camanho P.P, Davila C.G, DeMoura MF. Numerical simulation of mixed-mode progressive delamination in composite materials. *Compos Mater* 2003; 37(16): 1415–1438.
  59. De Moura M.F.S.F, Gonçalves J.P.M. Modelling the interaction between matrix cracking and delamination in carbon-epoxy laminates under low velocity impact. *Compos Sci Technol* 2004; 62: 1021–1027.
  60. Nishikawa M, Okabe T, Takeda N. Numerical simulation of interlaminar damage propagation in CFRP cross-ply laminates under transverse loading. *Solids Struct* 2007; 44: 3101–3113.
  61. Aymerich F, Dore F, Priolo P. Prediction of impact-induced delamination in cross-ply composite laminates using cohesive interface elements. *Compos*

- Sci Technol 2008; 68: 2383–2390.
62. Aymerich F, Dore F, Priolo P. Simulation of multiple delamination in impacted cross-ply laminates using a finite element model based on cohesive interface elements. *Compos Sci Technol* 2009; 69: 1699-1709
  63. Choi H.Y, Downs R.J, Chang F.K. A new approach toward understanding damage mechanisms and mechanics of laminated composites due to low-velocity impact: Part I-Experiments. *Compos Mater* 1991; 25: 992-1011.
  64. Garg A.C. Delamination-a damage mode in composite structures. *Eng. Fract. Mech* 1988; 29(5): 557-584.
  65. Fuoss E, Straznicky P.V, Poon C. Effects of stacking sequence on the impact resistance in composite laminates. Part 1: parametric study. *Compos Struct* 1998; 41(1): 67–77.
  66. Lopes C.S, Camanho P.P, Gürdal Z, Maimí P, González E.V. Low-velocity impact damage on dispersed stacking sequence laminates. Part II: numerical simulations. *Compos Sci Technol* 2009; 69(7–8): 937–47.
  67. Lopes C.S, Seresta O, Coquet Y, Gürdal Z, Camanho P.P, Thuis B. Low-velocity impact damage on dispersed stacking sequence laminates. Part I: experiments. *Compos Sci Technol* 2009; 69(7–8): 926–36.
  68. Schoeppner G.A, Abrate S. Delamination threshold loads for low velocity impact on composite laminates. *Compos Part A: Appl Sci Manuf* 2000; 31(9): 903–15.
  69. Morita H, Adachi T, Tateishi Y, Matsumoto H. Characterization of impact damage resistance of CF/PEEK and CF/toughened epoxy laminates under low and high velocity impact tests. *Reinf Plast Compos* 1997; 16(2): 131–43.
  70. Joshi S.P, Sun C.T. Impact induced fracture in laminated composite. *Composite Material* 1985; 19: 51-66.
  71. Dato M.H. *Mechanics of fibrous composites*. London: Elsevier Applied Science 1991.
  72. Simulia “Abaqus user’s guide (version 6.10)”.
  73. Shet C, Chandra N. Analysis of energy balance when using cohesive zone models to simulate fracture processes. *Eng Mater Technol* 2002; 124: 440–50.

74. Williams J.G, Hadavinia H. Analytical solutions for cohesive zone models. *Mech Phys Solids* 2002; 50(4): 809–25.
75. Alfano G. On the influence of the shape of the interface law on the application of cohesive-zone models. *Compos Sci Technol* 2006; 66: 723–30.
76. Hinton M.J, Kaddour S.K, Soden P.D. A comparison of the predictive capabilities of current failure theories for composite laminates, judged against experimental evidence. *Compos Sci Technol* 2002; 62: 1725–1797.
77. Orifici A.C, Herszberg I, Thomson R.S. Review of methodologies for composite material modelling in incorporating failure. *Compos Struct* 2008; 86: 194–210.
78. Hou J.P, Petrinic N, Ruiz C. A delamination criterion for laminated composites under low-velocity impact. *Compos Sci Technol* 2001; 61: 2069–2074.
79. ISO 15024: 2001. Standard test method for Mode I Interlaminar fracture toughness  $G_{IC}$  of unidirectional fibre reinforced polymer matrix composites.
80. Bianchi F, Zhang X. Modelling of Hybrid Metallic Composite Joints. PHD Interim Review 2009. Cranfield University.
81. Asp L.E. The effects of moisture and temperature on the interlaminar delamination toughness of a carbon/epoxy composite. *Composites Science and Technology* 1998; 58(6): 967–977.
82. Ning Y, Zhang X. Prediction of Low Velocity Impact Load of Composite Plates Using the Quasi-Static Load Method. MSc Thesis 2009. Cranfield University.



# **APPENDICES**

## **Appendix A Concept Design of Flying Wing Aircraft**

### **A.1 Introduction**

The Group Design Project (GDP) which is a concept design of a commercial flying wing aircraft started in March 2011 and finished in August the same year. According to the requirements of Aviation Industry Corporation of China (AVIC), the concept design of flying wing aircraft was conducted during this time.

The concept design of flying wing was divided into two main different phases. In phase one, the concept design of a conventional aircraft was finished with the aim of helping us become familiar with the concept design process. In the second phase, the concept design of flying wing was completed successfully.

The general requirements of the aircraft are listed below:

1. Twin-aisle, 250 seats international aircraft
2. 7500 nm range
3. M 0.80-0.85 cruise speed
4. Taking-off and Landing at 4E airports

The GDP work was divided into five different stages.

In the first stage, the geometric design characteristics of 150-250 passengers' aircraft were studied and information relating to design requirements was also collected.

During the second stage, the design drivers and general requirements of the desired aircraft were investigated.

In the third stage, the cabin layout and family issues for conventional aircraft were studied and several cabin layouts were presented according to market survey results.

In the final stage, the preliminary structural layout of the cabin of flying wing was studied.

## A.2 Geometric Design Characteristics

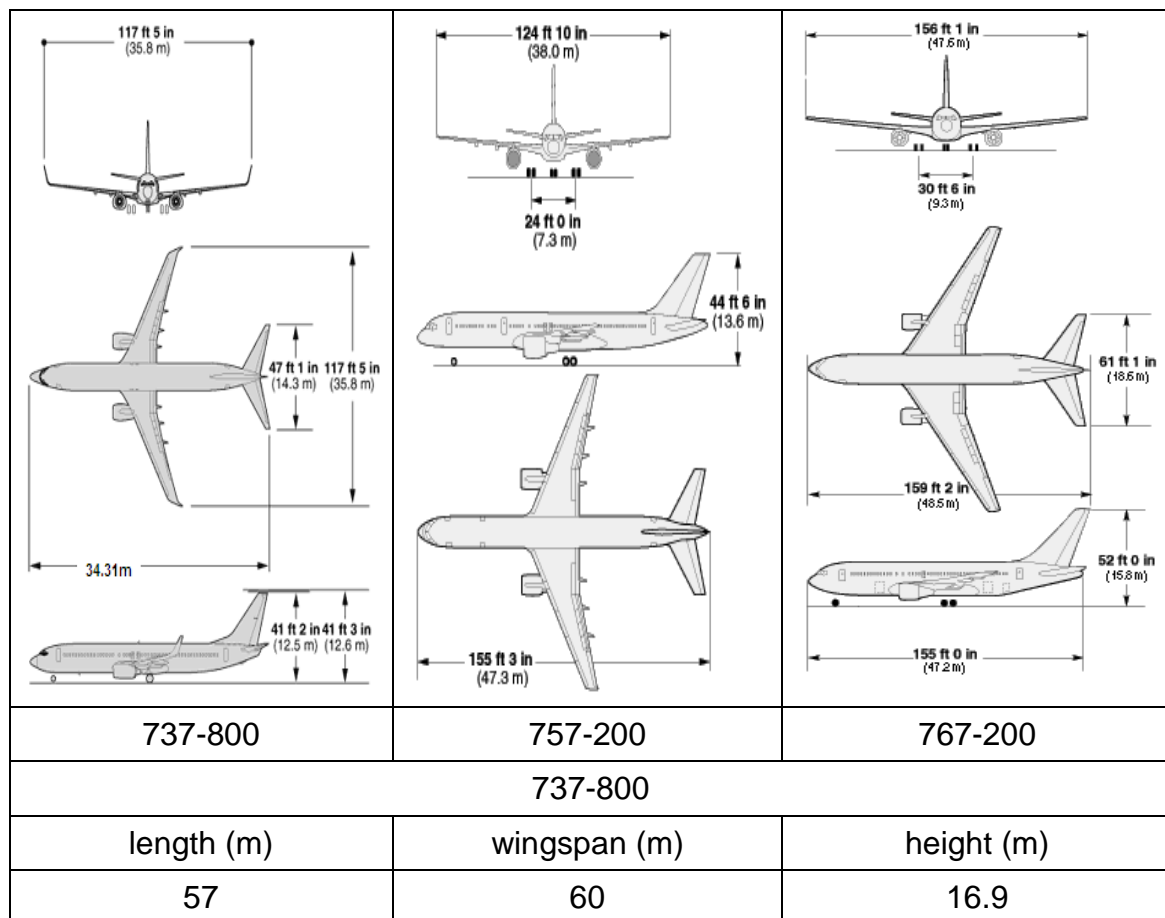
Information collection and analysis were the main objects of this phase's work. The work was divided into four different aspects according to the pattern of world aircraft design and manufacture, Airbus aircraft, Boeing aircraft, flying wing and other aircraft.

Geometric information includes wing area, wing span, sweepback, fin and tail area, fuselage geometry, landing gear, engine characteristics, material usage and so on. Boeing series aircraft were studied in this period of time. The types of aircraft fitting its design requirements are listed below.

**Table\_Apx A-1 Boeing aircraft types satisfying design requirement**

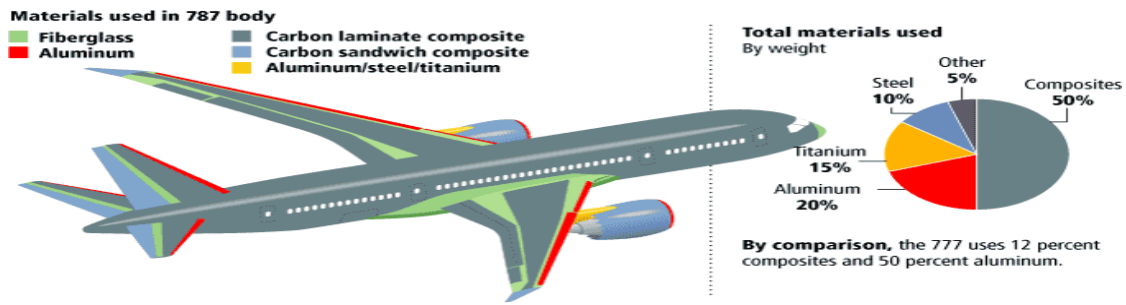
Type	737-800	757-200	767-200	787-8
Seats	160-189	200-234	181-290	210-250

The three-view drawings of the above types are illustrated in figure A-1.



**Figure\_Apx A-1 Three-view drawing of three Boeing aircraft**

The materials used in the Boeing 787 body are shown in figure A-2.

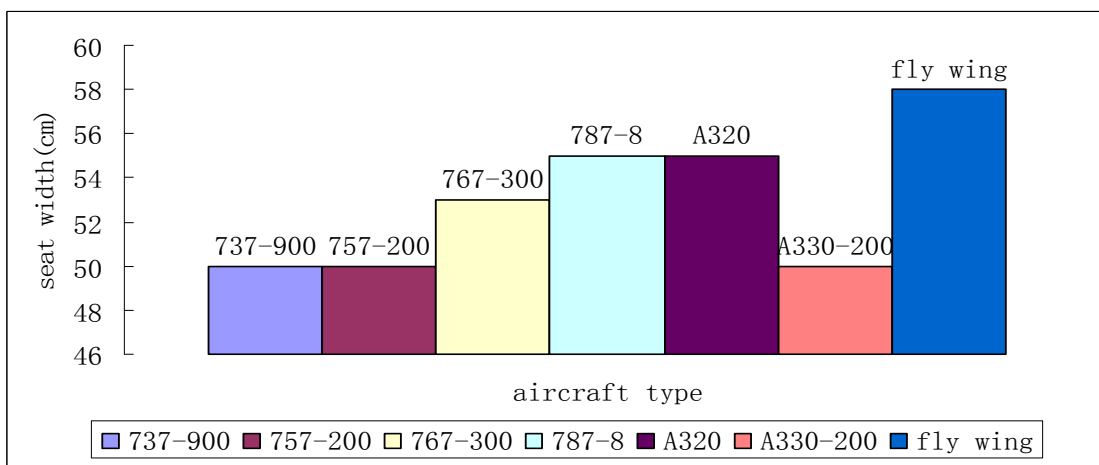


Figure\_Apx A-2 Materials used in Boeing 787 body [1]

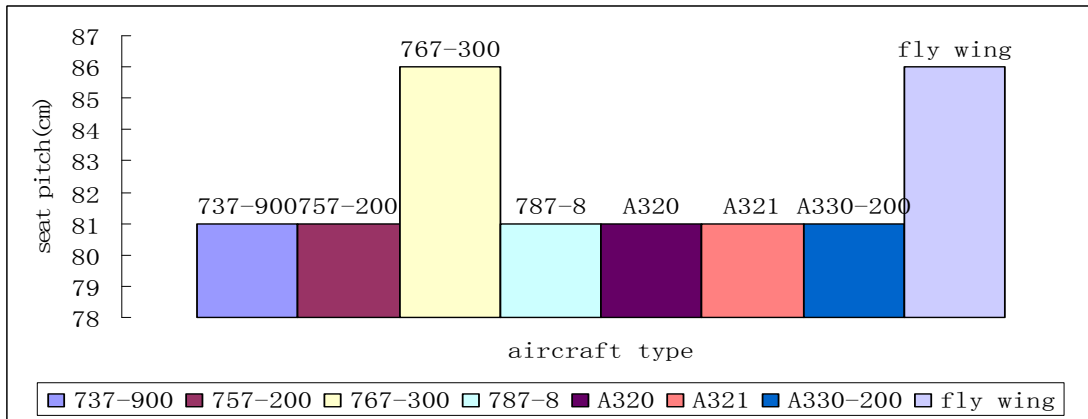
### A.3 Design Drivers and General Requirement

In order to design a new aircraft to compete with already existing aircraft, several design drivers were considered which were green, comfort, cost, and airworthiness.

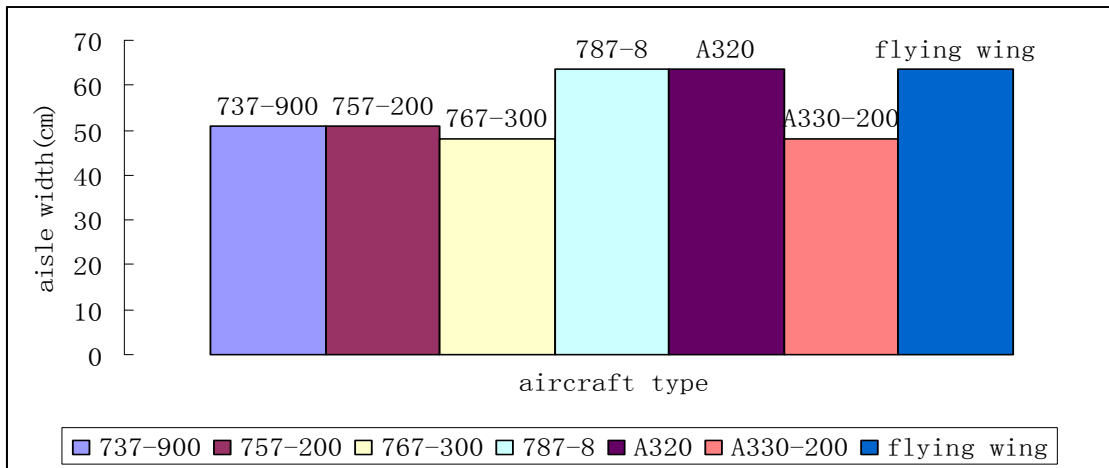
The design driver comfort for passengers was studied during this period of time. The factors which will affect the comfort of passengers include width and pitch of seats, width of aisle, cabin pressure and cabin humidity. The comparison between flying wing and conventional aircraft in terms of seat width, seat pitch, width of aisle and pressure altitude are illustrated in figure A-3 to figure A-6.



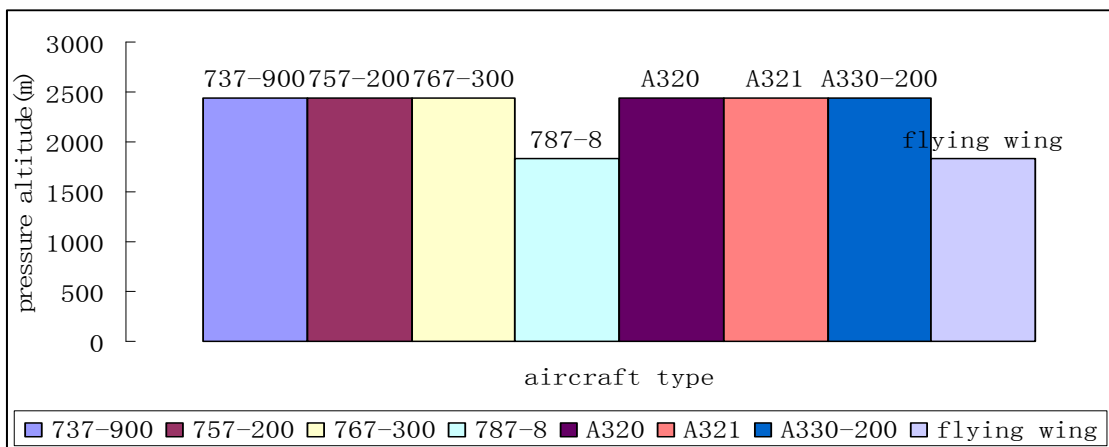
Figure\_Apx A-3 Seat width comparison between flying wing and other aircrafts



Figure\_Apx A-4 Seat pitch comparison between flying wing and other aircrafts



Figure\_Apx A-5 Aisle width comparison between flying wing and other aircrafts



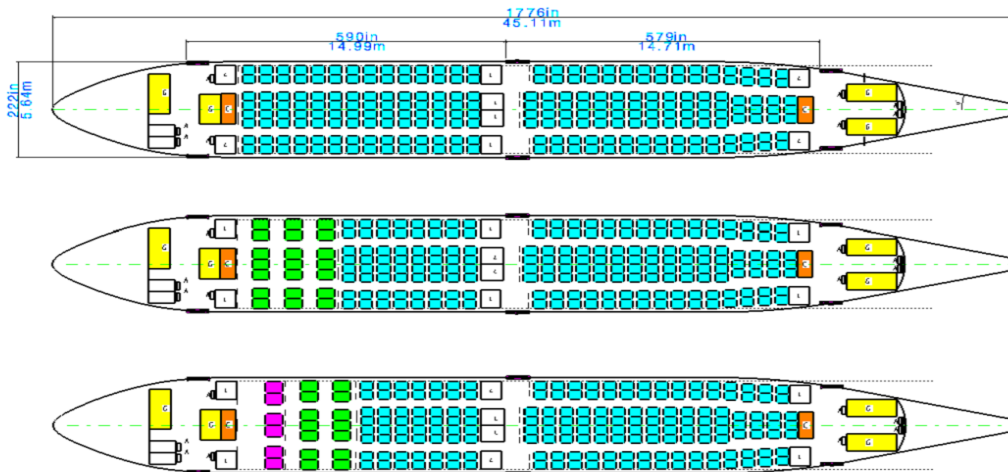
Figure\_Apx A-6 Pressure altitude comparison between flying wing and other aircrafts



Because of the wide usage of composite material in the cabin, greater cabin humidity can be achieved as another design driver.

### A.4 Cabin Layout and Family Issues

At this stage, cabin layouts for conventional aircraft of both long and short range were studied. The cabin layout for long rang types is illustrated below.

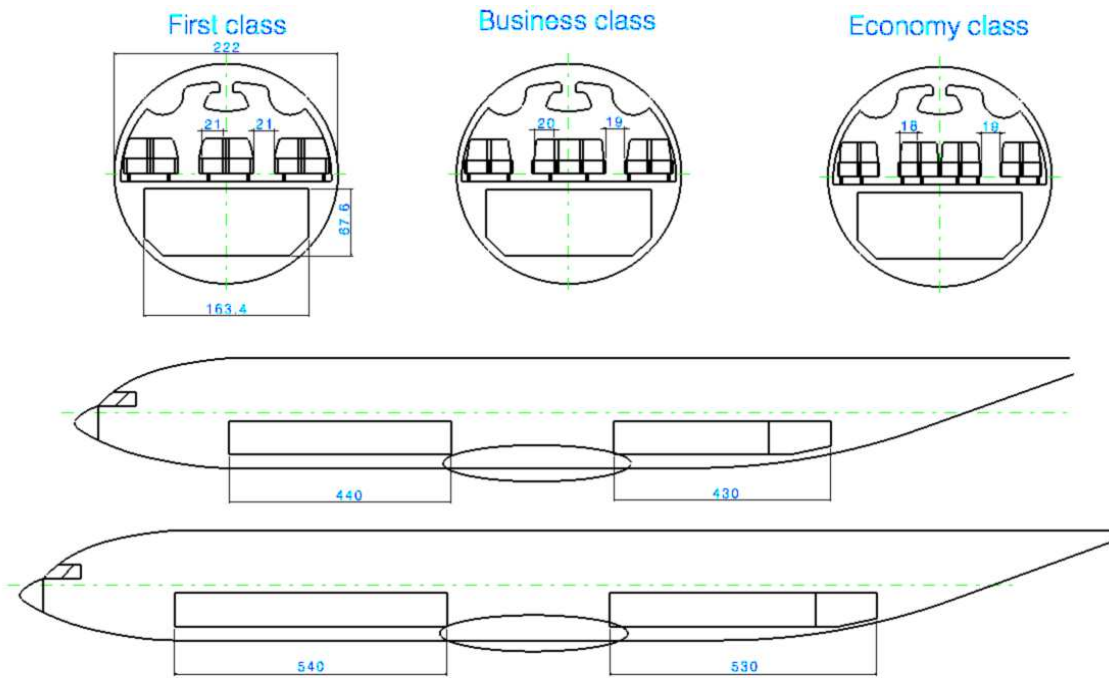


Figure\_Apx A-7 Cabin layout of long rang type aircraft

The cabin layout of short range aircraft is shown in figure A-8. The cross section and side view of the fuselage is shown in figure A-9.



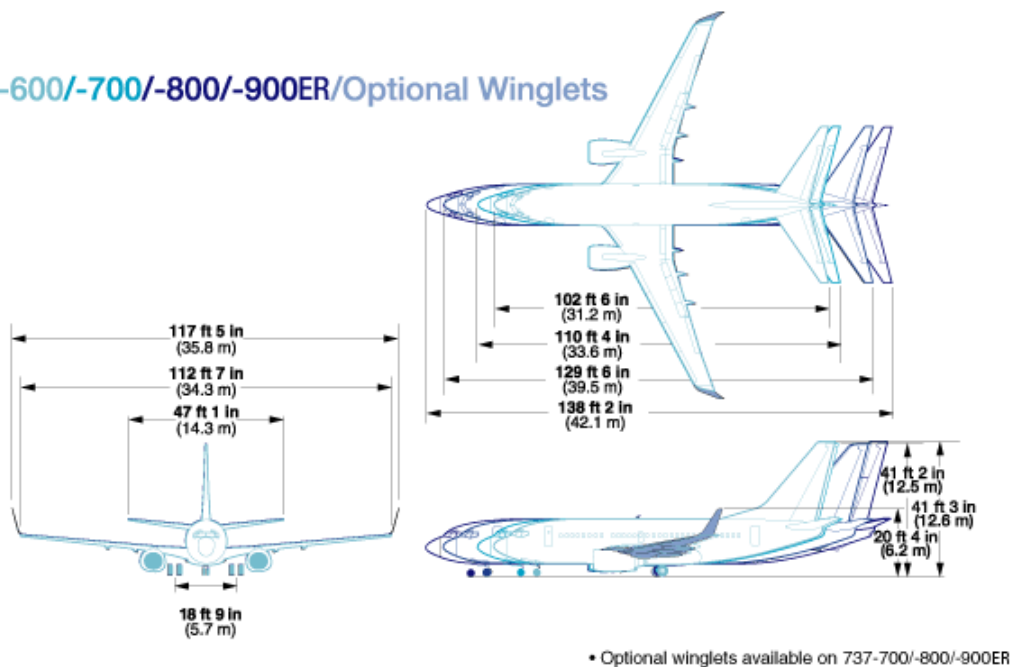
Figure\_Apx A-8 Cabin layout of short rang type aircraft



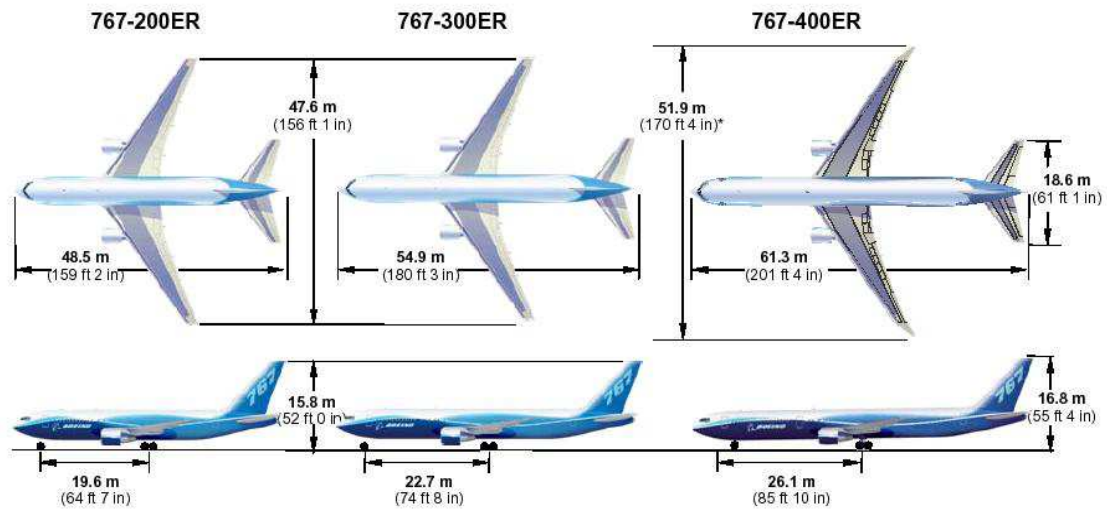
Figure\_Apx A-9 Cross section and side view of the fuselage

Family issues were also investigated using Boeing series aircrafts. Boeing 737 and 767 family aircrafts are shown in figure A-10 and A-11.

### 737-600/-700/-800/-900ER/Optional Winglets



Figure\_Apx A-10 Boeing 737 family aircrafts [1]

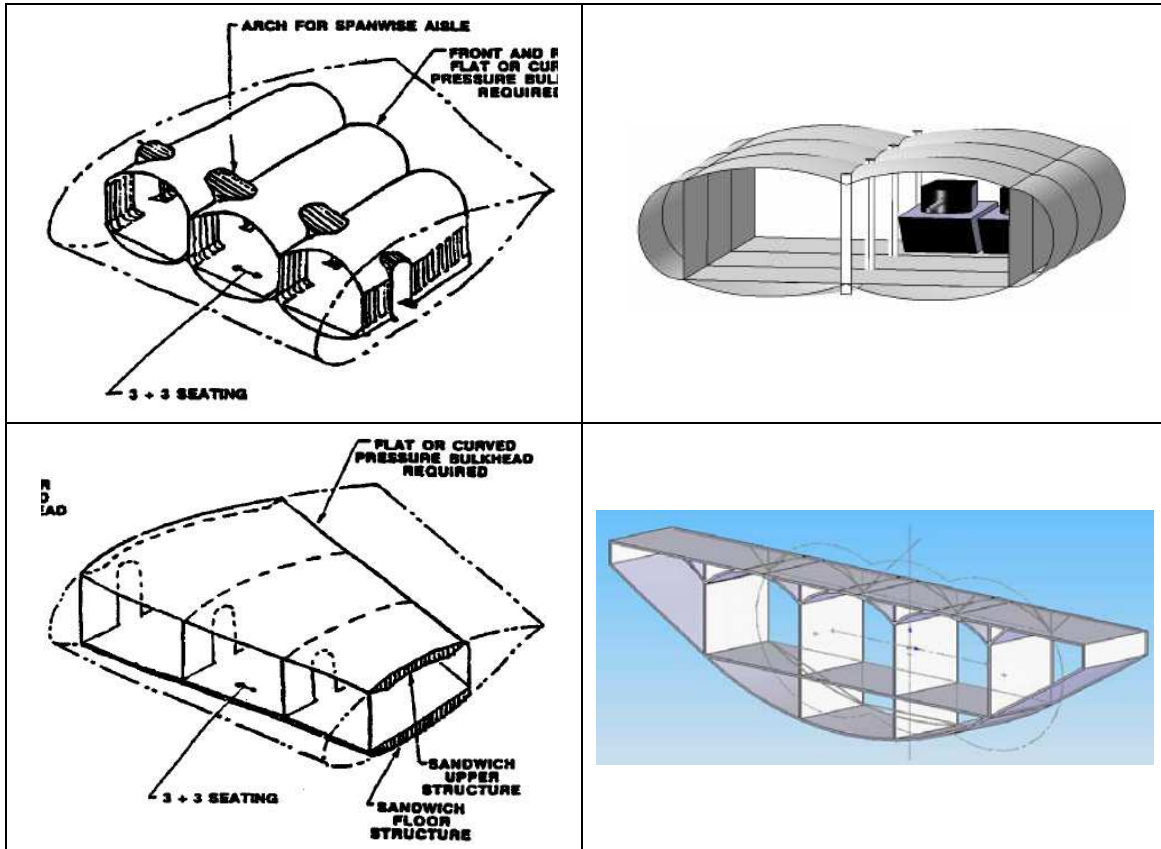


**Figure\_Apx A-11 Boeing 767 family aircrafts [1]**

As can be seen above, almost the same wing structure and extended fuselage were used in both Boeing 737 and 767 family aircrafts.

### **A.5 Preliminary Structure Layout**

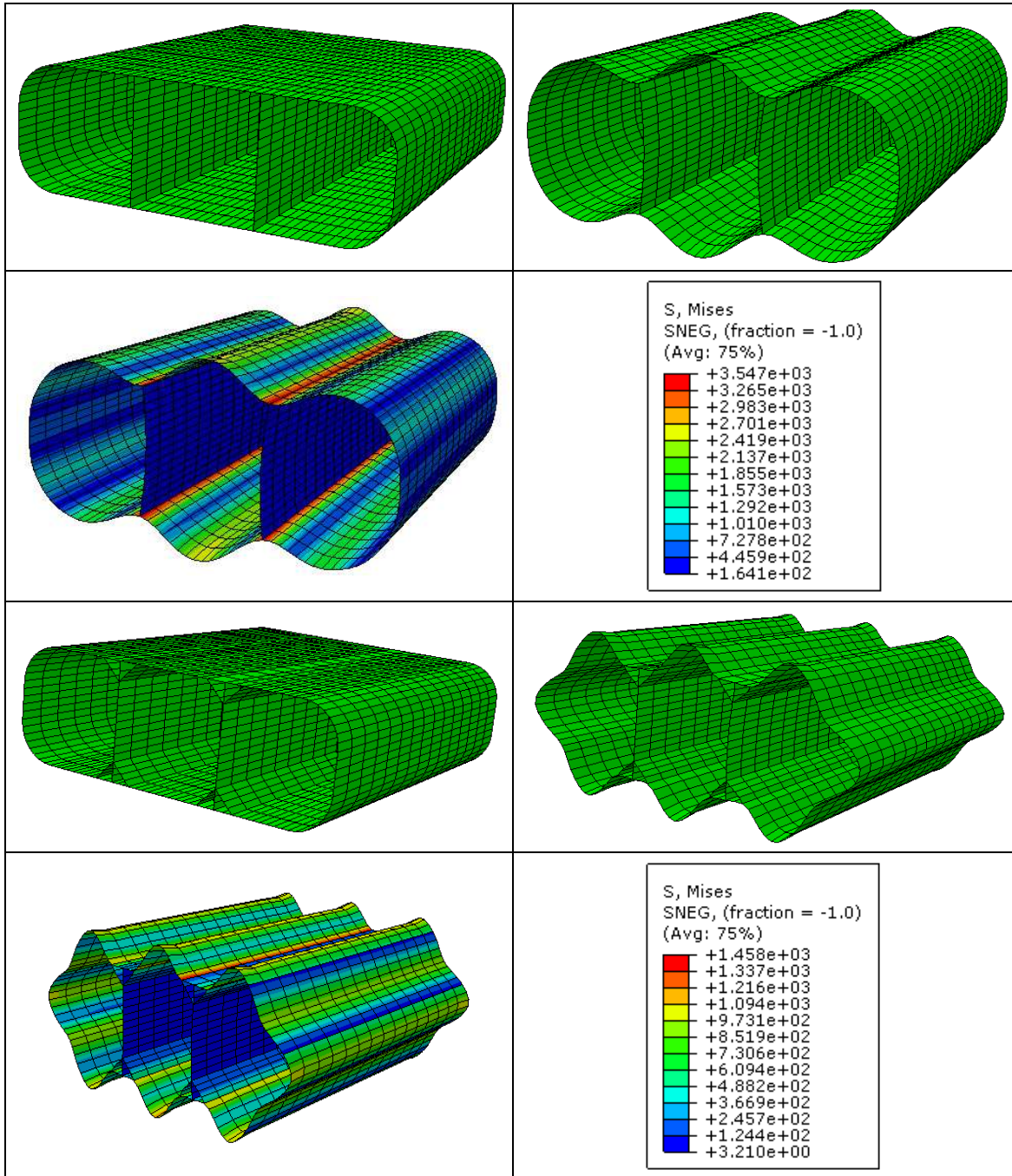
In order to carry pressure load in the cabin while maintaining good aerodynamic outer surface, four different structure concepts for the cabin were investigated as illustrated in figure A-12.



Figure\_Apx A-12 Structure layout for cabin of flying wing

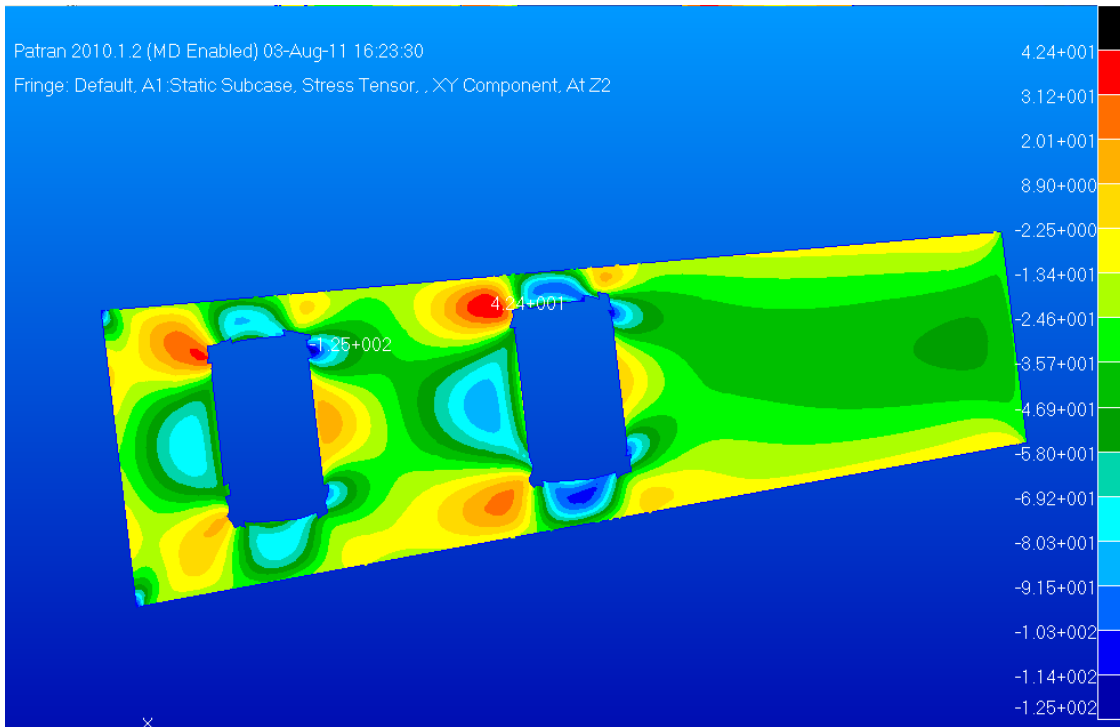
The two concepts at the top of figure A-12 use separate pressure vessels and outer skins at the same time. The two concepts at the bottom of figure A-12 use integrated skins which carry the pressurized load and aerodynamic load together.

Though separate pressure vessels can carry pressure efficiently, two layers of skins bring weight penalty to this concept. The stress analysis was carried out for the structure layout at the lower right which was finally used. The deformation and stress distribution can be seen in figure A-13.



**Figure\_Apx A-13 stress analysis of the cabin structure**

Apart from the calculation of the pressurized cabin, front and rear spars were also analysed. In order to satisfy the evacuation requirement, cabin doors were located at the leading edge which resulted in two big cutouts at the spar web. FE analysis was carried out to study the shear stress level around the cutout. The shear stress distribution of the spar web is illustrated in figure A-14.



**Figure\_Apx A-14 Stress distribution of the spar web**

As can be seen in figure A-14, the shear stress around the cutout is about 125 MPa which is almost twice the stress level at the area away from the cutout. According to the analysis above, the cutout of spar web is feasible but structure enhancements are needed to carry the extra shear stress arising from the cutout.

## REFERENCES

1. Boeing Company's website: <http://www.boeing.com/>.
2. Airbus Company's website: <http://www.airbus.com/>.
3. Lloyd R. Jenkinson, Paul Simpkin and Darren Rhodes, "Civil Jet Aircraft Design", Arnold, a member of the Hodder headline Group, London, 1999.
4. Daniel P. Raymer, "Aircraft Design: A Conceptual Approach", American Institute of Aeronautics and Astronautics, Inc. Washington, D.C. 1989.
5. Remy Reynaud, "BWB, the future airliner: Comparison between flying wing and conventional aircraft", Master Thesis, Cranfield University, 2005.
6. Airbus S.A.S, "A330 Airplane Characteristics for Airport Planning", Airbus France, January 1993.